NOVEL FABRICATION OF SIC BASED CERAMICS FOR NUCLEAR APPLICATIONS

By

ABHISHEK KUMAR SINGH

Bachelor of Technology in Mechanical Engineering
Indian Institute of Technology
Kanpur, UP, India
2001

Master of Science in Mechanical Engineering
State University of New York at Stony Brook
Stony Brook, NY, USA
2006

Submitted to the Faculty of the
Graduate College of
Oklahoma State University
in partial fulfillment of
the requirements for
the Degree of
DOCTOR OF PHILOSOPHY
May, 2009

COPYRIGHT ©

By

ABHISHEK KUMAR SINGH

May, 2009

NOVEL FABRICATION OF SIC BASED CERAMICS FOR NUCLEAR APPLICATIONS

Dissertation Approved:

Dr. Raman P. Singh

Dissertation Advisor

Dr. Allen Apblett

Dr. Hongbing Lu

Dr. Kaan Kalkan

Dr. A. Gordon Emslie

Dean of the Graduate College

ACKNOWLEDGMENTS

I would like to express my gratitude and appreciation to the members of my dissertation committee, Dr. Hongbing Lu, Dr. Kaan Kalkan, and Dr. Allen Apblett, for their feedback and co-operation while scheduling the date for the dissertation defense.

It has been a pleasure working with my lab-mates in the Mechanics of Advanced Materials Laboratory. My colleagues Dr. Gajendra Pandey and Dr. Suraj C. Zunjarrao hold a special place in my heart. I would also like to thank Dr. Ranji Vaidyanathan for allowing me to be a part of a few extremely critical projects. In a relatively short interaction period, I have had a few memorable moments.

I am especially grateful to my mentor Dr. Raman P. Singh, who has been a guardian for me during all these years. His supportive method empowers students to perform at their best. I always admire his clear and focussed thinking. Dr. Singh taught me subtle ways of thinking and importance of being open to other research areas. His insights are embedded all along this work. During the last few months, Dr. Singh took time to give me frank and very sound advice about my career plans and future directions. I've much enjoyed and learnt from our discussions and look forward to continue working with him in the years to come.

I thank my parents and my sister, Parul, for their endless support and encouragement during the years. I promised my wife, Kavita, that I would not give her the stereotypical public thanks for her support, and I am not doing so! *But, I dedicate this work to her.* Anushka, my cute little daughter, will definitely complain on not finding a single line for her. Or maybe not.

TABLE OF CONTENTS

LIST OF TABLES

LIST OF FIGURES

LIST OF ABBREVIATIONS

a-SiC	Amorphous silicon carbide
β-SiC	β-Silicon carbide
λ	Thermal conductivity
AHPCS	Allylhydridopolycarbosilane
BeO	Beryllium oxide
Bo3B	Ball-on-three-balls
CVD	Chemical vapor deposition
CVI	Chemical vapor infiltration
DU	Depleted uranium
ECO	Enhanced thermal conductivity oxide
FE	Finite element
Gen IV	Generation IV
GFR	Gas-cooled fast reactor
MOX	Mixed-oxide
PIP	Polymer infiltration and pyrolysis
Q	Heat flow
RoR	Ring-on-ring biaxial flexure method
SiC	Silicon carbide
TRISO	Tristructural-isotropic
UHP	Ultra high purity
XRD	X-ray diffraction

CHAPTER 1

DEFINITION OF THESIS PROBLEM

1.1 Objective

The objective of this work is to investigate the feasibility of a novel processing approach for the fabrication of silicon carbide (SiC) based composite fuels and in-core materials for ultra high temperature applications such as the Generation IV (Gen IV) Gas-Cooled Fast Reactor (GFR).

Current nuclear power generation technology is based on Gen II and Gen III reactors. Advances in reactor technology and the use of gas-cooled fast reactors require the development of new materials that can operate at the higher temperatures expected in these systems. Such materials include refractory alloys based on Nb, Zr, Ta, Mo, W, and Re; ceramics and ceramic-matrix composites such as SiC–SiC_f; carbon–carbon composites; and advanced coatings. Besides the ability to handle higher expected temperatures, effective heat transfer between reactor components is necessary for improved efficiency. Improving thermal conductivity of the fuel can lower the center-line temperature and thereby enhance durability and reduce the risk of fuel pellet failure due to cracking and premature degradation. This also leads to increased power production and lower waste generation because of reduced temperature buildup and long fuel service life. Finally, the materials must be suitable for applications in a nuclear radiation environment.

For this investigation, the focus is on crystalline silicon carbide, which has superior characteristics as a structural material from the viewpoint of its thermal and mechanical properties, thermal shock resistance, chemical stability, and low radioac-

tivation [1,2]. There has been much effort to develop SiC based composites in various forms for use in advanced energy systems [3, 4].

1.2 Motivation

The world's primary energy need has increased by more than 50 times the pre-industrial level. However, the biggest energy challenge of today is not running out of resources but the increase in greenhouse gas emissions, such as CO_2 levels in the atmosphere. Global warming remains a controversial issue, but according to the Intergovernmental Panel on Climatic Change (IPCC), the observed increase in overall global temperature is most likely due to high greenhouse gas concentration [5]. This report predicts a temperature increase of 1.8–4.0 °C in the next century, and it is theorized that such changes can cause irreversible damage to life on earth [6].

In recent years there has been renewed interest in nuclear energy as a viable, long term, and economic power source, that is free of geo-political supply disruption risks, and also free of carbon emission problems. While, proliferation of nuclear weapons, reactor safety, and nuclear waste management continue to be issues, it has been recognized that nuclear power continues to have significant potential as a non-green house gas producing source of energy. At the current usage rate, the existing nuclear resources are sufficient for over 85 years of operation [7]. Furthermore, wider use of breeder reactors and fuel reprocessing would significantly improve the fuel availability. In that case, it is estimated that the total conventional resources of uranium could suffice for 16000–19000 years [8].

The current nuclear reactors are considered second generation (Gen II). The Department of Energy's Generation IV Initiative is focussed to develop reactors that will offer significant advances in sustainability, economics, safety and reliability, and proliferation resistance [9]. The new reactor technologies have stringent requirements to achieve higher efficiencies. Therefore, specifically tailored materials are now required

to handle high temperature functionality.

The innovative concepts that are being considered for next generation reactors employ relatively high coolant outlet temperatures. These increased temperatures would increase energy conversion efficiencies as well as provide sufficient heat for high temperature processes, such as hydrogen production [10]. Gas-Cooled Fast Reactors (GFR) are one of the six identified systems under focus for the Gen IV reactors [11]. For the GFR, the in-core temperatures in the gas-cooled reactors can be as high as 1200 °C during normal reactor operation and may exceed 1700 °C in case of an accident [12]. In general, fuel elements should have high mechanical strength to endure various external mechanical loads, irradiation, and thermal stresses, while maintaining their integrity [13]. This is even more so for the GFR and other high temperature reactors, resulting in ceramic materials being investigated as candidates for both advanced nuclear fuels and in-core materials.

Refractory-based ceramics (carbides: SiC, ZrC, TiC, NbC; nitrides ZrN, TiN; and oxides: MgO, $Zr(Y)O_2$) display a number of unique properties, including extremely high melting points and hardness, as well as high thermal and electrical conductivity, and solid-state phase stability [11,14,15]. This combination of properties makes these "refractory carbides" potential candidates for high-temperature nuclear reactor components, including shielding, fuel, control elements, and structural components. Refractory carbides are also excellent candidates for a variety of other high-temperature structural applications, including zero-erosion rocket nozzle throats, hypersonic leading edge materials, combustion liners, engines, plasma arc electrodes, cutting tools, furnace elements, and high temperature shielding [16,17].

In recent years, with the development of high yield preceramic precursors, the polymer infiltration and pyrolysis (PIP) method has aroused interest for net-shape fabrication of ceramic based materials, for various applications ranging from disc brakes to nuclear reactor fuels [18]. The pyrolysis of preceramic polymers allows a

wide variety of ceramic materials to be processed at relatively low temperatures. The raw materials are element-organic polymers whose composition and architecture can be tailored and varied. At first, during the pyrolysis of these precursors, amorphous materials are formed which have an atomically homogenous element distribution and, in this state, represent a new class of materials with very interesting properties. Additionally, these amorphous states can be crystallized to stable or metastable phases by a second annealing, where, under certain conditions, and with surprising ease, nanocrystalline materials are formed, whose microstructures are stable at very high temperatures. These technological characteristics of precursor pyrolysis processing, and the fact that the preceramic stage can be processed relatively easily using standard techniques of polymer processing technology to various material forms (fibers, films, infiltrates, etc.) and components, means that this method has a high application relevance.

The pyrolysis-based process also provides numerous advantages in comparison with other techniques used to manufacture advanced ceramic materials and composites, including chemical vapor deposition (CVD), and chemical vapor infiltration (CVI), and high-temperature sintering. The pyrolysis process requires only a controlled atmosphere oven for material fabrication. The liquid polymer precursor is easy to handle and can be stored for long periods of time under appropriate conditions. The PIP process is environmentally friendly, does not require hazardous acid scrubs, as for CVD/CVI, and produces only simple gaseous byproducts. The liquid and dust-free nature of the process makes it especially attractive for remote processing of highly radioactive species, such as plutonium (^{239}Pu, ^{244}Pu) and americium (^{241}Am, ^{243}Am).

Finally, the preceramic stage can be processed relatively easily using standard techniques of polymer processing technology to generate various material forms and components (fiber reinforced and graded structures, thin films, complex shaped bulk

materials, etc.), with no inherent limitations with regard to component size. Appropriately designed gradations and microstructures can be used to minimize residual, thermal, and irradiation induced swelling stresses, provide multifunctional characteristics, and optimize the nuclear characteristics.

The primary focus of this effort is to use a pyrolysis based process to fabricate a host of novel silicon carbide-metal carbide/oxide composites, and to synthesize new materials based on mixed-metal (metal/silicon) carbides that cannot be processed using conventional techniques. It is expected that these mixed-carbide material systems will offer improved material properties for high-temperature applications. In addition to material processing, mechanical property characterization of precusor-derived ceramic matrix composites, in terms of biaxial strength, is carried out using equibiaxial 'ring-on-ring' test. Room temperature thermal conductivity of these composites are measured and there is an ongoing effort to characterize the effect of various constituents in the composite on mechanical strength. This has led to a better understanding of such manufacturing process. Solid state reactions that take place during the pyrolysis are determined from X–ray diffraction. Finally, factors affecting the fabrication of precursor-derived SiC matrix composites are characterized and the feasibility of the current process is established.

CHAPTER 2

BACKGROUND AND LITERATURE SURVEY

Nuclear materials can be broadly classified into in-core and out-of-core components. The in-core component materials include fuel assemblies and the neighboring coolant channels for water reactors, cladding (cylindrical tubes that house the fuel pellets) for the fuel and the wrapper (a container that houses fuel elements, in between which the coolant flows) for subassemblies of fast reactors. The out-of-core materials form the rest of the nuclear reactor system. Typical issues of concern for all nuclear materials are radiation resistance, high-temperature mechanical performance, compatibility with the fuel and the coolant, and manufacturability [8]. Figure 2.1 [11] shows a schematic representation of the proposed GFR, showing the core components, out-of-core components, and balance-of-plant components.

In a nuclear reactor core, generally all materials are subjected to demanding temperature, stress, and neutron irradiation conditions. Depending on the design of the reactor, the service exposure conditions including temperature, temperature gradient, irradiation dose, and stresses vary from component to component within the same reactor. Ceramic materials offer the advantage of a much higher temperature and environmental stability in comparison to conventional polymers or metals without large change in the physical properties. These properties associated with ceramic materials make them highly attractive for their use as nuclear materials. Table 2.1 represents the screening requirements for GFR material selection based on Generation IV goals [19].

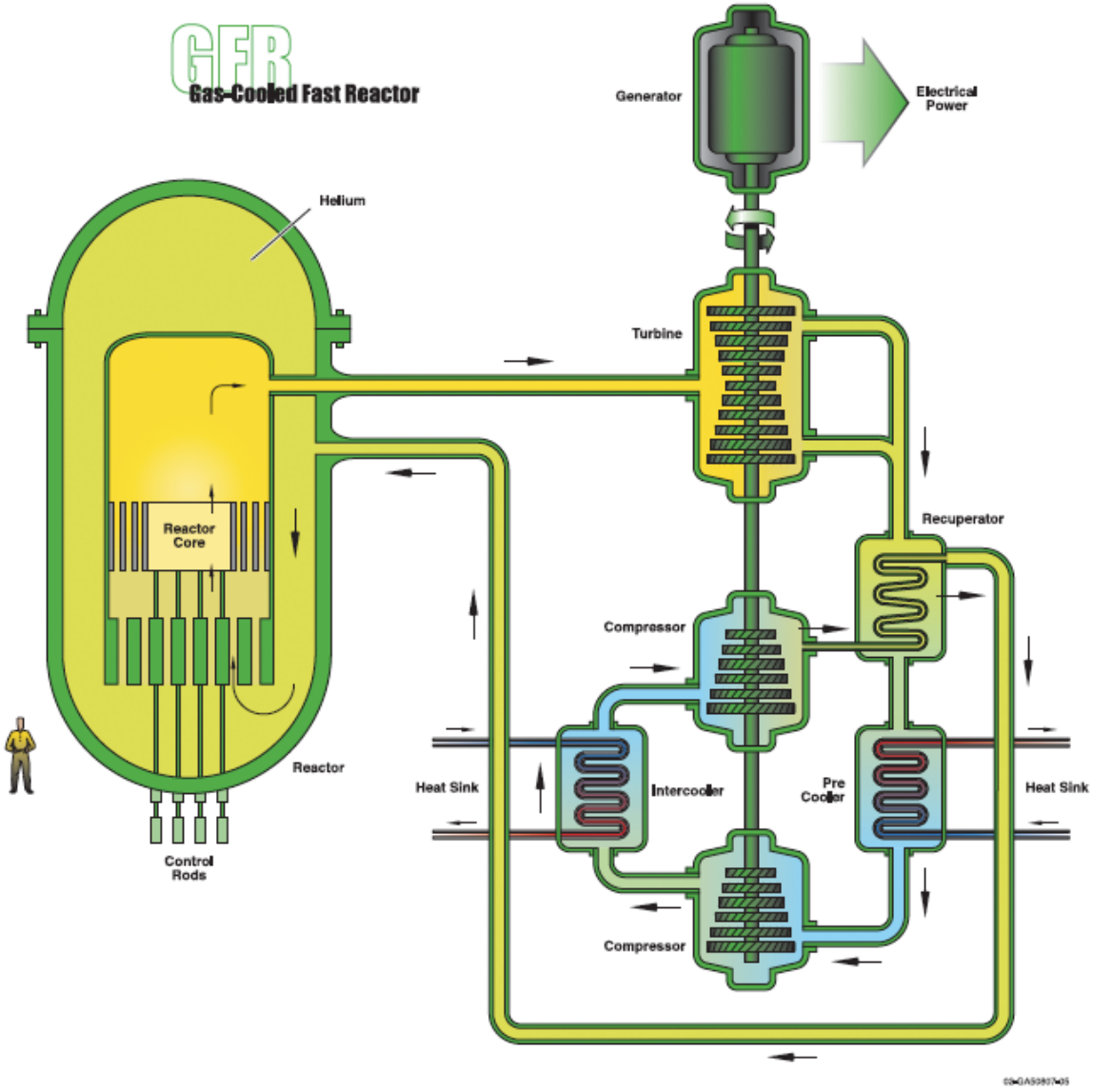

Figure 2.1: Schematic of different components in a reactor: core components, out-of-core components, and balance-of-plant components [11].

Requirement	**Reference Value**
Melting/decomposition temperature	$> 2000\,^{\circ}\mathrm{C}$
Radiation induced swelling	$< 2\%$ over service life
Fracture toughness	> 12 MPa-m$^{1/2}$
Thermal conductivity	> 10 W/m-K

Table 2.1: GFR fuel matrix and structural material reference requirements [19].

2.1 Conventional Oxide-based Nuclear Fuels

Only one fissile nuclide, ^{235}U, is found in nature, where it occurs with an isotopic abundance of 0.72%. The remainder of natural uranium is ^{238}U and ^{234}U with 99.2745% and 0.0055% natural abundance, respectively. Despite this low concentration of fissile isotope, it is possible to fuel certain types of critical reactors with natural uranium, and all the early reactors were of this type. It is also possible to manufacture certain fissile isotopes from a nonfissile material. This process is commonly known as conversion, and the two most important fissile nuclides manufactured using conversion are ^{233}U and ^{239}Pu.

Natural uranium obtained from the ore exists in the form of a number of complex oxides. These are first converted to U_3O_8, which is then converted to uranium hexafluoride, UF_6, for enrichment. The enrichment process increases the concentration of ^{235}U, following which UF_6 is converted to UO_2 [20]. Finally, UO_2 is fabricated into fuel assemblies and loaded into the reactor. The fuel pellets are formed using compaction followed by sintering to remove voids. The presence of voids can lead to decreased thermal conductivity. Most present-day nuclear power reactors employ uranium dioxide based fuel.

The wide-spread use of uranium dioxide fuel is primarily due to the many desirable characteristics of the uranium dioxide material, such as a high density of uranium atoms necessary for initiating and sustaining a nuclear reaction, inertness and insolubility of the uranium dioxide in high temperature water, and the ease of fabricating fuel pellets by sintering. Additionally, UO_2 has a high melting point and does not contain neutron poisons which could affect reactor performance. In fact, UO_2 is the only stable 'oxide' of uranium at higher temperatures above 1500 °C [21] till its melting point of 2800 °C [22]. However, UC and UN were chosen as the reference fuel for GFRs, instead of UO_2, due to their higher thermal conductivity, higher heavy metal density, and minimal impact on neutron spectrum [19].

2.1.1 Fabrication of oxide based fuels

Powder metallurgical routes have been used successfully in the industry for the production of both UO_2 and mixed oxide (MOX – made up of about 5% plutonium and 95% uranium[1]) fuel pellets. The powder based processes involve a large number of mechanical steps [23] and the fabricated pellets have to meet stringent dimensional quality control requirements. The typical fast reactor fuel pellets are about 5 mm in diameter and 8–10 mm in height. The tolerance on the diameter of these pellets is less than 50 μm [24]. Each fuel pin holds around 100 such pellets and there are several thousands of fuel pins in a typical fast reactor core. The precise dimensional requirements along with surface defects are very difficult to be met in a shielded cell fabrication facility. This results in a high percent of rejects and lower throughput.

Amongst other efforts to fabricate fuel, sol–gel processes provide solutions for the fabrication of ceramic nuclear fuels [24]. With the sol–gel process, handling of radioactive toxic powder is eliminated. However, this process has not been studied to improve the existing thermal behavior of the fuels. Sol–gel processing generally has lower yields, and porosity issues due to greater shrinkage, and produces in–situ particles that must be sintered. Another non–powder based method for preparing ceramics, and that has promising potential, is pyrolysis based processing of polymer–derived ceramics.

2.1.2 Thermal conductivity enhancement in oxide based fuels

The low thermal conductivity of the oxide based uranium fuel, which further decreases with increasing temperature [22, 25], is its biggest shortcoming. This can limit the operating temperature of a reactor, thereby the efficiency and gas outlet temperature. Furthermore, low thermal conductivity also results in high center-line

[1] using MOX helps to manage the plutonium stocks that would otherwise increase by using *only* conventional uranium based reactors

temperatures leading to faster fuel degradation and thermo-mechanical cracking. A few critical properties of UO_2 and other alternative uranium based fuels are given in Table 2.2 [26–29]. Increasing the thermal conductivity by as little as 5% or 10% would provide significant benefits in terms of lowered volume-averaged fuel temperature, fission gas release, and fuel rod internal pressure [30]. The nuclear industry has made attempts to increase the thermal conductivity of uranium dioxide fuel, but none of the attempts have been successful so far. Apart from this, uranium dioxide based fuels are supported by a well-established technology and currently remain the dominant fuel for nuclear power reactors [31].

Property	**UO_2**	**UC**	**UN**	**U metal**
Theoretical density (g/cm^3 at 25 °C)	10.96	13.63	14.32	18.95
Heavy metal atom density (g/cm^3)	9.67	12.97	13.52	18.95
Melting point (°C)	∼2800	∼2400	∼2700	1132
Thermal conductivity (W/m-K)				
200 °C	7.19	22.49	4	30
1000 °C	3.35	7.58	20	50.2
Static modulus of elasticity (GPa at 25 °C)	190	87.3	–	

Table 2.2: Properties of various uranium based fuels [26–29].

Polymer infiltration and pyrolysis was used recently by Sarma *et al.* [32] to fabricate enhanced thermal conductivity oxide (ECO) fuels. They used SiC and BeO as a non-fissile, high-conductivity phase in the uranium dioxide based fuels. The choice of these materials was based on their sufficient chemical compatibility with UO_2, stability in aqueous environments, compatibility with zircaloy, neutronic properties, and irradiation performance. In general, SiC is known to react with UO_2 at relatively low temperatures in open systems at 1370 °C [33], and at 1800 °C in closed isothermal systems [34]. Due to these restrictions, sintering could not be used; as SiC is very difficult to sinter below 2000 °C without using large volume fractions of sintering aids [35]. Therefore, they used the polymer infiltration technique to process UO_2 pellets to get SiC in the secondary phase. Their approach was to infiltrate pre-sintered

plugs of UO_2 using precursor derived SiC. However, unacceptable thermal conductivities were observed, possibly due to limited infiltration of the polymer precursor. On the other hand, BeO is stable with UO_2 up to its eutectic points of 2160 °C [36]. It can be sintered at typical fuel fabrication sintering temperatures as well.

For ECO fuels, Solomon *et. al.* [37] found that 10 vol.% of continuous phase BeO in UO_2 increases the thermal conductivity of the composite, 50% over standard UO_2 fuel. Furthermore, a 25% increase in thermal conductivity of UO_2 can be obtained at 1100 °K with an almost continuous 4.2 vol.% of BeO phase at the grain boundaries [38]. But to achieve this, it has to be processed above 2433 °K, the eutectic temperature. However, dispersed BeO in UO_2, processed at lower temperatures did not result in the same improvements [30].

The presence of BeO in the ECO fuel necessarily displaces some uranium and therefore decreases the uranium loading of a fuel assembly. Although it might be expected that a significant increase in ^{235}U enrichment would be required to offset the loss of uranium, neutronic calculations showed that the required increase in enrichment is only about 0.007%. Because of this insignificant change, Mccoy *et. al.* [30] claim a possibility of significant reductions in uranium costs. However, the hexagonal structure of BeO raises the concern for anisotropic radiation growth at high damage doses. This still remains to be addressed for its acceptance in nuclear applications.

2.2 Carbide-based Nuclear Fuels

Carbide based fuels are the primary candidates for gas-cooled fast reactors (GFR) [11]. The high thermal conductivity and density of the carbide based fuels allows for a superior specific power operation compared to conventional oxide based fuels [39]. The carbide based fuels have higher melting point and higher thermal conductivity compared to a similar oxide- or nitride-based fuel [40]. For example, the thermal conductivity of uranium monocarbide (UC) is about five times higher than UO_2 (as given

in Table 2.2). This is of extreme importance for high temperature applications. For this reason, uranium carbide based fuels in a silicon carbide clad are being considered for the GFR systems where, under nominal full power operation, the peak fuel, and clad temperature limits are 1500 °C, and 1100 °C, respectively [19].

The reactivity of uranium carbide with metals poses a restriction on materials for cladding and coolant. However, niobium and its alloys are compatible with UC up to very high temperatures. Moreover, the solubility of zirconium, niobium, tantalum and vanadium in uranium monocarbide can be used to develop cermets with enhanced mechanical properties and corrosion resistance. For example, UC alloyed with 50 mole% of ZrC shows significant improvement in resistance against water corrosion. Furthermore stoichiometric monocarbide is stable to sodium up to at least 900 °C, thus sodium is an attractive coolant for systems with (U, Pu)C fuels [22]. Krishnaiah *et al.* [41] claimed that due to its higher thermal conductivity, UC had higher conductivity integral compared few other selected fuel materials (including UO_2, (U,Pu)O_2, (U, Pu)C, and UO_2-Ni). Moreover, the data indicated that the total energy per pin of carbide fuel was three times higher than the oxide based fuel.

The U.S. and the former Soviet Union developed solid solutions of uranium carbide and carbides of refractory metals in support of high temperature nuclear fuel development for space nuclear propulsion systems. Owing to this growing interest, several fuel forms and microstructures were tested earlier in the U.S.'s NERVA/Rover program including dispersed fuels with UO_2 or UC_2 particles in graphite and a composite solid-solution (U, Zr)C and graphite [42, 43]. Tosdale [44] predicted similar improved performances in a study of UC–ZrC–NbC systems. While UC-ZrC and ZrC-NbC-UC based composite fuels have exhibited melting temperatures in excess of 2927 °C, the rather involved material processing procedures have restricted their widespread adoption. However, there are inconsistencies in the data reported for the carbide based fuels, most probably due to the varying carbon contents [42]. There-

fore, a better understanding of the ternary system is still required before large scale deployment of these fuels.

Tristructural-isotropic (TRISO) is a fuel type that contains microspheres of either UCO, UC_2, ThO_2 or UO_2 depending on the type of the reactor. These microspheres are enclosed in layers of PyC and silicon carbide, as shown schematically in Fig. 2.2 [45]. The silicon carbide layer acts as the primary barrier for the nuclear fission products and the radioactive elements and also provides structural integrity to the fuel. Tristructural-isotropic fuel is designed to withstand fission gas pressures even at temperatures upto 1600 °C. Therefore, these are considered accident resistant and are extremely desirable form of fuel for two Gen IV reactor designs.

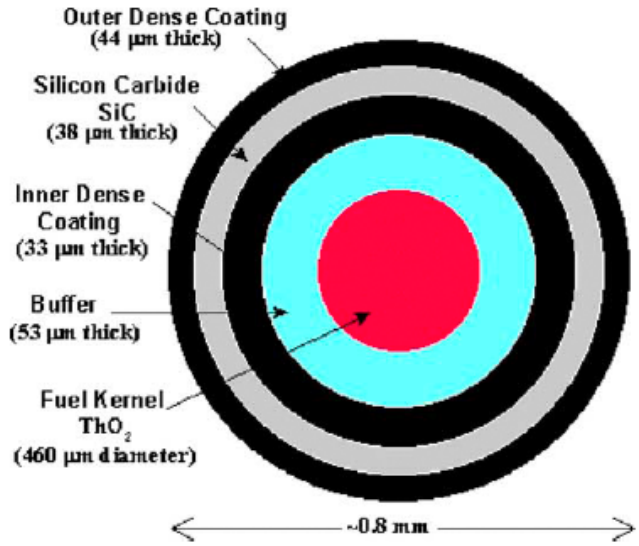

Figure 2.2: Schematic representation of the Tristructural-isotropic (TRISO) fuel [45].

2.2.1 Mixed-metal carbides

Mixed-metal carbide and metallic silicocarbide systems are even more of an exciting development in refractory carbides. Mixed-metal carbide systems rely upon the ability of refractory metals such as hafnium and zirconium to form alloys with niobium, tantalum, titanium, and other transition metals. While research in this area has been limited by processing issues, the evidence is highly promising. For example, the

alloy tantalum hafnium carbide (Ta_4HfC_5), with a melting point of 4215 °C, is one of the most refractory substances known to mankind. Also, the high-temperature hardness of $(Ta_{0.8}Hf_{0.2})C_{1+x}$ exceeds that of both pure-metal carbides TaC_{1-x} and HfC_{1+x}. The melting points of the mixed-metal carbides outperform those of the pure-metal carbides, as well. For example, 8TaC-ZrC and 4TaC-HfC exhibit melting points of 3890 °C and 3990 °C, respectively, somewhat higher than those of the pure-metal carbides (measured at 3470, 3750, and 3840 °C for ZrC, HfC and TaC, respectively) [46].

Mixed carbide fuels, (U, Zr, Nb)C, are being currently studied for their applicability in Gen IV reactors. Their high thermal conductivity make them a more desirable form of fuel over the conventional UO_2 based nuclear fuels. Moreover, their longer life expectancy and stability at higher temperatures make them a candidate fuel for nuclear thermal propulsion (NTP). This is possible because of their high melting temperature, high thermal conductivity and resistance to hot hydrogen corrosion [47].

Fuel performances such as melting temperature and corrosion resistance due to hydrogen (critical for NTP), varies with its microstructure [47]. Czechowicz *et al.* [48] observed the formation of a second phase, carbon, in equilibrium with the solid-solution (U, Zr)C_x during their stoichiometric studies of (U, Zr)C. The melting temperature of these eutectic compositions, (U, Zr)C_x+C, was also affected by the uranium content in the compound.

The evolution toward an uncoated all carbide, solid-solution (U, Zr)C fuel was motivated by unacceptable mass losses from earlier designs due to the high reactivity of free carbon with the flowing hot hydrogen propellant and the mismatch in coefficient of thermal expansion between the graphite matrix and NbC or ZrC coatings. Furthermore, Butt *et al.* [49], in a thermochemical analysis of the binary carbide systems (U, Zr)C and (U, Nb)C, suggested that an optimized composition of (U, Zr, Nb)C, might exhibit the longest operating lifetime.

Due to the stringent requirements associated with fabricating these materials using powder metallurgy techniques it is apparent that the development of novel processing techniques, that permit the formation of mixed-metal carbides and allow for direct control over the ceramic composite microstructure, is highly desirable to fully harness the ultra-high temperature potential of refractory, mixed-metal carbides.

2.3 SiC-based Materials in Nuclear Applications

Irradiation induced creep and void swelling are two major material issues in fast reactors. The tendency of a material for swelling and irradiation creep is characterized in terms of its change in dimensions with increasing irradiation dose or increasing stress measured at a constant temperature and dose, respectively [8]. Of the various advanced ceramics, silicon carbide has superior characteristics as a structural material from the viewpoint of its thermal and mechanical properties, thermal shock resistance, an excellent hermeticity with respect to gases (cooling gas fluids or gaseous species formed by nuclear reactions), and low radioactivation [1, 2, 50].

The effect of high temperature irradiation on swelling and mechanical properties of high purity SiC has been evaluated by various researchers. Raffrey *et al.* [51] found that high cycle efficiency and safety considerations make SiC/SiC materials attractive for use as high performance blankets with LiPb. While the irradiation stability of SiC has always been of concern, it has been established that suitable properties are expected when the composition of silicon carbide is close to stoichiometric and the microstructure is crystalline [2,52–57]. In a recent study, Hinoki *et al.* found excellent high temperature irradiation resistance for high purity SiC/SiC composites irradiated up to 1600 °C [2]. Moreover, Newsome *et al.* [56] reported insignificant degradation in mechanical properties for high purity silicon carbide after irradiation. They found that the magnitude of volumetric swelling depended on the irradiation temperature and material, and was nearly independent of the irradiation fluence. Such properties

make crystalline SiC a promising candidate for use in nuclear applications.

There have been many efforts to develop SiC based composites in various forms for use in advanced energy systems. Kim *et al.* [58] prepared multi-layer coatings for UO_2 based fuels using silicon carbide and pyrolytic carbon. Such multi-layered coating, having layers of dense carbon and β-SiC with fine columnar grains is considered optimum for coated nuclear fuel pellets. Alkan *et al.* [3] proposed a joining technique of SiC parts so that the fissile material could be encapsulated in SiC capsules. Lee *et al.* [4] studied the effect of cyclic thermal shock on the mechanical and thermal properties of various ceramics being considered as candidates for nuclear fuel matrices. They observed that the silicon carbide based material exhibited superior mechanical and thermal shock performance at higher temperatures, as compared to those based on zirconia or magnesia aluminate.

Several other favorable attributes of silicon carbide includes a very high disassociation temperature of 2830 °C [59], oxidation resistance up to about 1600 °C, excellent thermal conductivity, 31 W/m °C, and a very low coefficient of thermal expansion, $4.7 \times 10^{-6}/\,^{\circ}\mathrm{C}$ at 1200 °C [60]. Moreover, Munro reported extremely high stiffness, 387 GPa, even at elevated temperatures of 1200 °C [60]. The combination of high thermal conductivity and low thermal expansion provide exceptional thermal shock resistance [61]. Such properties make SiC an extremely attractive ceramic material. However, the same characteristics make SiC a very difficult material to fabricate.

There are several requirements for the successful application of these materials. First, the fabrication process must allow control over microstructure and material purity to ensure performance under high temperature and irradiation environments. Second, the processing technique should allow for facile incorporation of reinforcements and net shape manufacturing. Finally, a non-powder based method would be preferable for processing techniques that involve the handling of highly radiotoxic and pyrophoric materials.

2.4 SiC Fabrication Using Polymer Infiltration and Pyrolysis

Typical manufacturing of ceramic products is based on shaping and consolidation of fine ceramic powders. Large sintering shrinkage of 15–20% limits geometrical accuracy; therefore, machining is often needed to achieve precision and intricacy. Very high temperature or pressure required during sintering, magnify the energy requirements for these techniques. This also inhibits the incorporation of reinforcements such as silicon carbide fibers, which degrade at temperatures above 1200 °C [62].

Polymer infiltration and pyrolysis (PIP) is an alternative approach for the fabrication of ceramic materials and composites. It offers direct control of the microstructure and composition; allows for incorporation of fibrous and particulate reinforcements; and, perhaps most importantly, offers the possibility of net shape manufacturing with controlled porosity at temperatures as low as 500–1500 °C [63–66]. In this manner, the PIP process can be used for consolidation of several compatible species due to its adaptability. Therefore, fabrication of ceramic components through PIP is a flexible and a potentially cost efficient approach. Also, the ceramic yield is much higher in polymer derived processing as compared to other non–powder chemical routes. In some cases, ceramic yield as high as 85% has been reported [67]. It is advisable to use slow heating (usually $\sim 1\,^{\circ}\mathrm{C/min}$) below 650 °C for better yield. Slow heating favors the lower temperature ($\sim$400 °C) curing of the polymer that involves the competitive processes of gas evolution by decomposition of the lighter molecules releasing H_2 and polymerization. This stage is critical in filling the porosity [37]. Finally, this process offers the unique possibility of modifying the structure and composition, and thereby the properties of ceramics, by designing the chemistry of the polymer precursor [68].

Polymer infiltration and pyrolysis has been identified as a viable alternative for fabricating SiC based materials [32, 63–65, 69–72]. However, the use of PIP for fabricating materials targeted for nuclear applications is limited. Very recently, Sarma *et al.* [32] fabricated UO_2 based fuel pellets using a combination of sintering and polymer

infiltration and pyrolysis. However, unacceptably small improvements were observed, as discussed earlier. Sarma *et al.* [32] also showed that PIP can be used for consolidating other dispersed phases like Tristructural-isotropic (TRISO) fuel particles with compatible SiC outer layers. They used relatively low processing temperature for PIP based pyrolysis to avoid reactions with UO_2 which impaired the composite's thermal conductivity. However, they postulated that UC or PuC would be more preferable as the fissile phase in SiC ceramics.

The current study investigates the use of the PIP technique to fabricate silicon carbide and uranium- oxide/carbide, refractory metals, and metal carbide based nuclear materials. Materials are fabricated by directly incorporating the compound of interest to the preceramic polymer, and then converting the latter to SiC by pyrolysis. In this manner, the subject process does not involve pre-sintering and can be used with any uranium or non-uranium additive [73, 74]. These additives can be categorized as active or passive fillers based on their stability with the polymer during pyrolysis. Inclusion of these fillers may increase the high temperature stability, creep and oxidation resistances of the composite. The presence of active fillers are desirable since they help in reduction of porosity and shrinkage while developing ceramic nano- or micro-composite [75].

2.4.1 Allylhydridopolycarbosilane (AHPCS), as a precursor for SiC

Allylhydridopolycarbosilane (AHPCS) was chosen as the preceramic polymer precursor for this study. Selection of this particular preceramic polymer was favored due to the fact that it is claimed to be a high purity precursor, that yields ceramic of near stoichiometric SiC. Additional benefits include reduced cycle times, ease of use and relatively low shrinkage. It is now widely used as precursor for SiC fibers. The polymer, designated as SMP–10, is acquired from Starfire Systems Incorporation (Malta, New York, USA). This polymer is a clear, amber viscous liquid and its

relevant properties are listed in Table 2.3.

Property	**Allylhydridopolycarbosilane (AHPCS)**
Density	0.998 (g/cc)
Appearance	Clear, amber liquid
Viscosity	80 to 100 cps
Solubility	Hexane, THF, acetone, toluene, insoluble in water
Flash Point	89 °C (192 °F)
Moisture Absorbtion	$< 0.1\%$ in 24 hrs at room temperature
Nominal Cure Temperature	250 to 400 °C
Surface Tension	30 dynes/sq.cm

Table 2.3: Properties of allylhydridopolycarbosilane (AHPCS) [76].

Initially AHPCS is an olefin-modified polymer that undergoes pyrolysis when heated under an inert atmosphere to yield near-stoichiometric SiC. Upon heating, the polymer precursor yields a dry and partially cross-linked solid at about 300 °C. Further heating results in more cross-linking accompanied by the loss of low molecular weight oligomers and hydrogen gas until a-SiC is obtained at about 900 °C [77]. However, according to manufacturer's specifications [76], a fully-ceramic, amorphous SiC forms at 850–1200 °C with minimal shrinkage, 80–82% ceramic yield and nanocrystalline β-SiC forms at 1250–1700 °C with a 75–80% yield.

CHAPTER 3

EXPERIMENTAL PROCEDURE

3.1 UO_2–SiC based Nuclear Fuels

The feasibility study of our novel technique was initiated by fabricating uranium oxide based fuel composites. A complete description of the fabrication for our first sample case, U_3O_8–UO_2 based ceramic composite, is presented here. For the fabrications described later, the procedure essentially remains the same and minor deviations are stated as necessary.

Depleted uranium (DU) was used as the material for fabricating fuel composites. A byproduct of the gaseous diffusion enrichment cycle, DU is artificially depleted in the lighter isotopes and contains 0.2% ^{235}U by weight. This depletion process effectively eliminates nuclear criticality concerns. Four type of depleted uranium materials were acquired from International Bio-Analytical Industries (Boca Raton, Florida, USA) including a block of solid depleted uranium metal, powders of uranium oxide (U_3O_8) and uranium dioxide (UO_2), and 4–20 mm sized irregular pieces of uranium carbide (UC).

Inherent radioactivity, pyrophoricity in powdered form, and perhaps most importantly, heavy metal toxicity associated with these materials poses additional handling requirements. Therefore, all the process involving these powders were performed in Unilab-2000 (MBraun Inc., Statham, NH, USA) glove box where an inert environment was maintained using argon flow. The glove box is equipped with an oxygen sensor module and all materials were handled at oxygen concentrations below 50 ppm. However, some of the preliminary work for this study was conducted in another smaller

glove box, which lacked the capability of an oxygen sensor or an active purge system. Figure 3.1 shows Unilab-2000 glove box used for all current material handling.

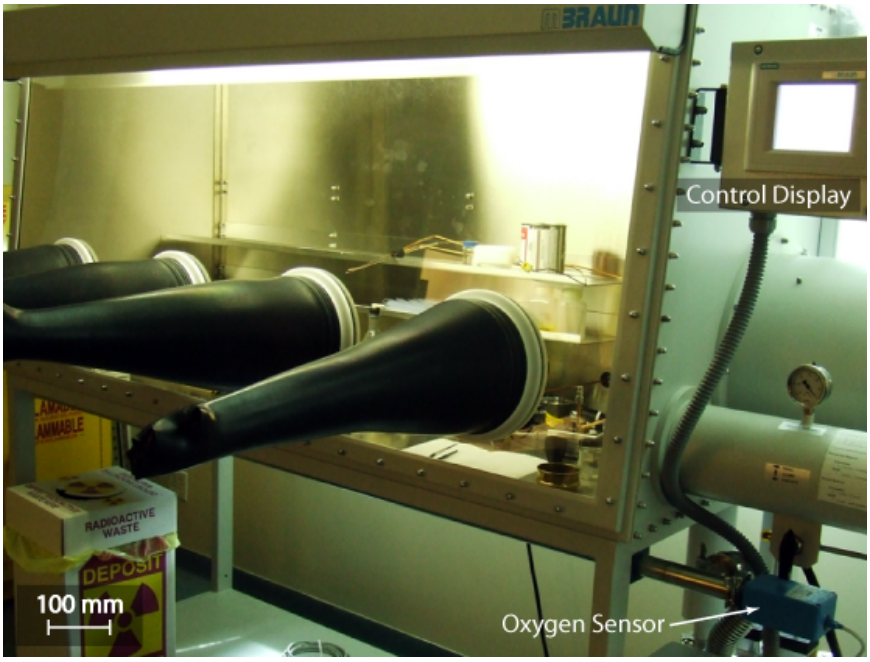

Figure 3.1: Unilab-2000 glove box equipped with oxygen sensor for handling pyrophoric powders.

3.1.1 Pellet fabrication

Pellet fabrication using the proposed technique involves mixing of the desired powder with a small amount of polymer precursor, net shape compaction in a mold to make a green body pellet that can be handled, and finally pyrolysis of the fabricated pellet. Due to large shrinkage during pyrolysis of the polymer, high porosity remains in the fabricated samples. Several infiltration and pyrolysis steps (typically 8 or more) are therefore required to fill these pores and aid densification. The complete fabrication process is schematically shown in Fig. 3.2.

To fabricate U_3O_8 based pellets, first a slurry was prepared by mixing 92 wt.% of U_3O_8 particles (International Bio-Analytical Industries, Boca Raton, Florida, USA) and 8 wt.% of the liquid AHPCS polymer precursor in a planetary ball mill (PM-100, Retsch GmbH, Haan, Germany). The composition of the initial slurry was selected so

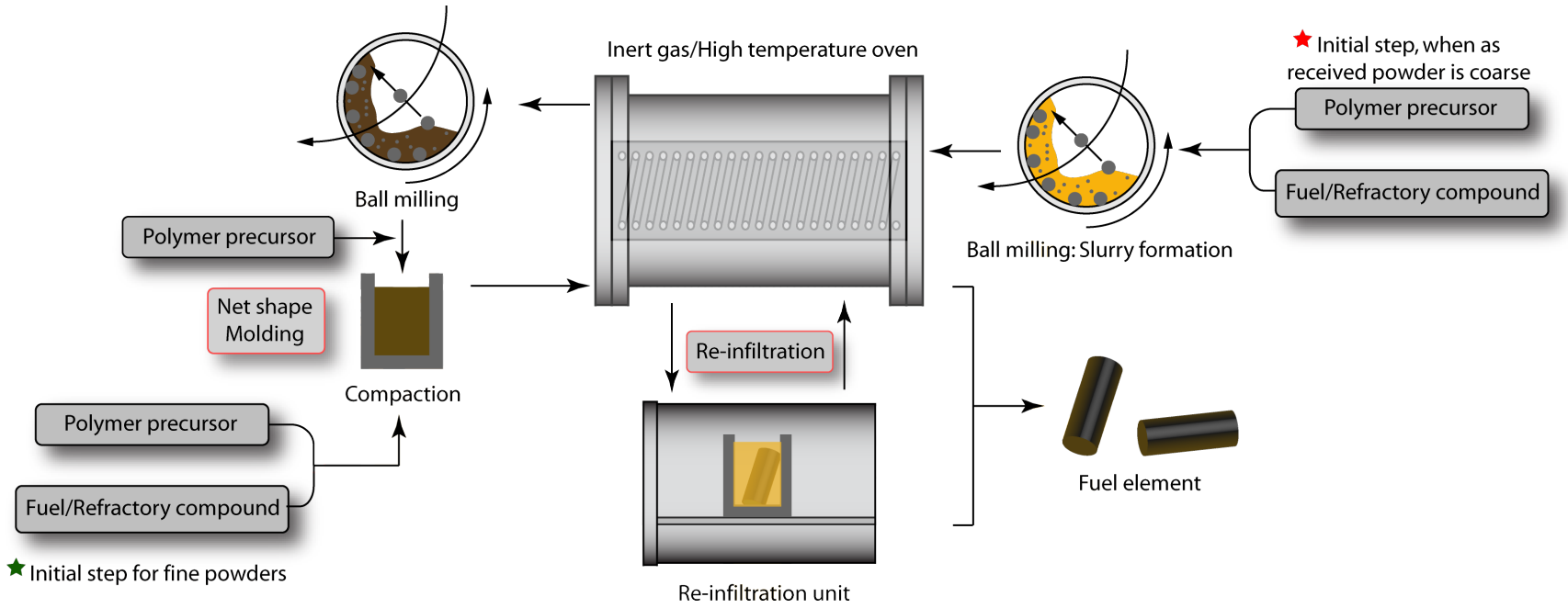

Figure 3.2: Schematic representation of the PIP based fabrication process.

that the final material would contain ∼4.99 g/cm^3 solid density of elemental uranium at the end of processing. This requirement was established by criticality calculations, carried out at Brookhaven National Laboratory, and was based on fissile loading used in the GCFBR design for the pin fuel concept [78]. An intermittent, on–off cycle of 3 min. each, at 300 rpm, for 6 hours was used to prepare the slurry. Such a cycle was chosen to provide adequate grinding and mixing while avoiding excessive heating. As-received U_3O_8 particles were irregular in shape (5–10 μm chunks), as shown in Fig. 3.3(a). The ball milling process reduced the size of the U_3O_8 particles and facilitated the coating of the polymer precursor.

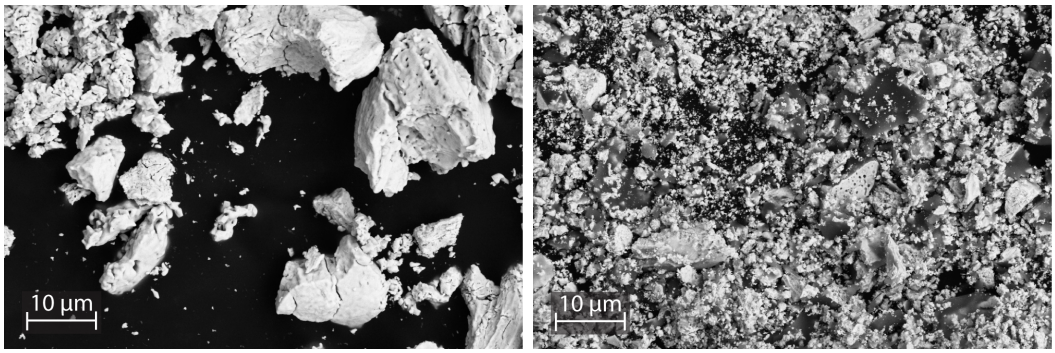

(a) As-received U_3O_8

(b) After first pyrolysis of slurry containing U_3O_8 and AHPCS

Figure 3.3: Uranium particles after initial processing.

The liquid slurry, obtained after ball milling, was pyrolyzed in a covered alumina crucible in a box furnace. This furnace was fitted with a retort that allowed for a continuous flow of an inert gas such as nitrogen or argon. In this case, the pyrolysis was carried out under ultra high purity (UHP) argon. The slurry was heated to 900 °C at a rate of 60 °C/hour, and was held at the peak temperature for 90 minutes to ensure thermal equilibrium. The pyrolysis of this slurry resulted in a solid that contained uranium oxide particles dispersed in an *a*-SiC matrix. However, due to the amount of polymer precursor used for this initial cycle, this solid acquired the shape of the crucible and contained large voids that were generated by the release of hydrogen gas.

In order to make cylindrical samples from this material, which could be tested for mechanical properties, the solid obtained after the above pyrolysis was crushed into powder by ball milling for 12 min. at 300 rpm. The powder thus obtained was then mixed with a small amount of polymer precursor (∼3% by weight of the milled powder) and compacted into short cylinders, ϕ25.4×15 mm, using a hydraulic press. A nominal compaction pressure of about 26 MPa was sufficient for producing green-body plugs that could be handled for further processing. These pre-compacted plugs, in the form of short cylinders, were pyrolyzed up to 900 °C at a rate of 60 °C/hour under argon atmosphere. A set of compacted pellets for this work are shown in Fig. 3.4.

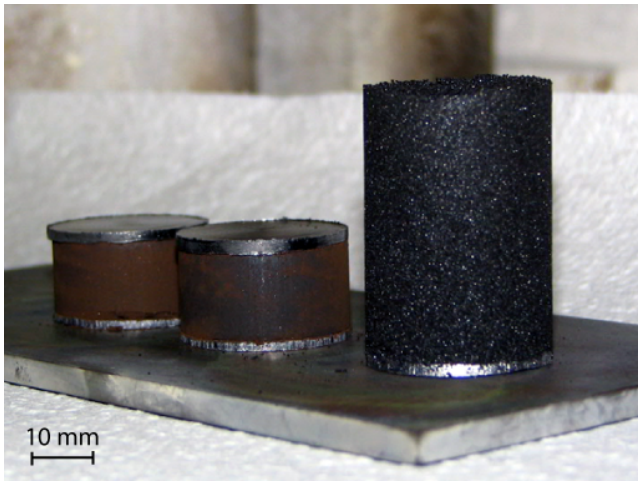

Figure 3.4: Compacted pellets, with a little use of polymer precursor with the powders.

As is customary in PIP processing, the samples were subjected to multiple polymer infiltration cycles. The reinfiltration of the cylindrical pellets was carried out under vacuum, with repeated 1 hour cycles for 3 hours with intermediate 1 min. purges. In addition, pressurized argon was used during each purge. This enhanced the re-infiltration while minimizing contamination [79]. A reinfiltration chamber acquired from Abbess Instruments (Holliston, Massachusetts, USA) was fitted with timed automated purge controller. However, before pouring the polymer onto the pellet for the

first time, the chamber was evacuated for 15 min. This aids in removing any trapped air in the pellet and reducing polymer's viscosity for better infiltration. Figure 3.5 shows the reinfiltration chamber designed to assist during impregnation cycles of PIP.

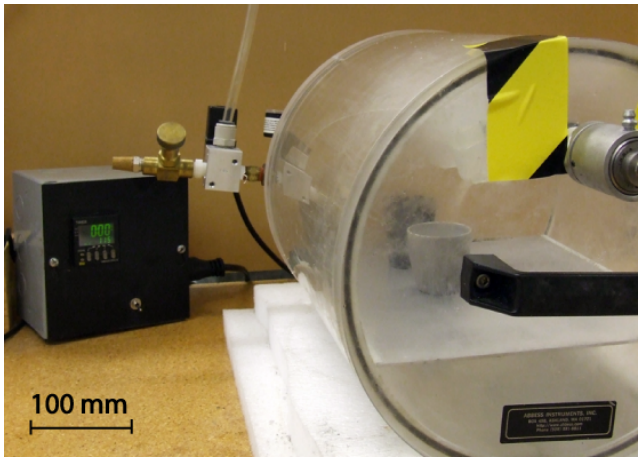

Figure 3.5: Reinfiltration chamber.

In the case of uranium oxide bearing samples, two types of composites were fabricated using different reinfiltration schemes. The first type of material, designated as a-SiC–U_3O_8–A, was prepared by using a mixture of polymer precursor and uranium powder (obtained after first pyrolysis and specifically ball milled for 9 hours to reduce its particle size) as the reinfiltrating liquid. The second type of material, designated as (a-SiC)–U_3O_8–B, was infiltrated using neat polymer precursor. In the first case, the use of uranium oxide particles in the infiltrating media to promote uranium loading, was stopped after the 5^{th} reinfiltration cycle. Beyond five reinfiltrations, the pore size becomes small and the presence of uranium oxide particles in the liquid polymer precursor could impede material densification. Subsequent reinfiltrations were continued using neat polymer precursor. In the second case, all reinfiltrations were done using neat polymer precursor.

The cylindrical specimens were sliced after the 3^{rd} reinfiltration cycle to obtain discs of 1 mm thickness using a precision sectioning saw (Isomet 1000, Buehler, Lake

Bluff, Illinois, USA). Prior work with polymer derived ceramic composites, using this polymer system, has showed that ∼6–8 reinfiltration cycles are sufficient to obtain the maximum achievable density [71]. Therefore reinfiltration of the discs was continued for a total of eight cycles.

To avoid oxidation of the components at any stage, all the handling and processing was carried out in an argon atmosphere. Also, control samples that contained only amorphous silicon carbide (*a*-SiC) were fabricated using the same procedure, but without the addition of any uranium oxide.

3.2 Metal-Carbide based Composites and Fuel

Uranium carbide and refractory metal carbides were used to fabricate SiC based composites. Fine powders, −325 mesh, of niobium carbide (NbC), and zirconium carbide (ZrC) was acquired from Alfa Aesar (Ward Hill, Massachusetts, USA) to fabricate carbide-carbide composites. Various combination of these materials were studied for investigating their reaction stability with AHPCS during pyrolysis.

No.	Material	Composition	Volume Ratio
1	SiC-PP-9010-H	SiC and PP	90:10
2	SiC-PP-9010-M	SiC and PP	90:10
3	NbC-PP-9010-H	NbC and PP	90:10
4	NbC-PP-9010-M	NbC and PP	90:10
5	ZrC-PP-9010-H	ZrC and PP	90:10
6	ZrC-PP-9010-M	ZrC and PP	90:10
7	NbC-SiC-PP-454510-H	NbC, SiC, and PP	45:45:10
8	ZrC-SiC-PP-454510-H	ZrC, SiC, and PP	45:45:10
9	ZrC-NbC-PP-454510-H	ZrC, NbC, and P	45:45:10
10	UC-PP-H	UC, and AHPCS	n/a

Table 3.1: Fabrication scheme and composition of carbide based materials.

Table 3.1 provides a list of metal carbide based materials fabricated during this investigation. Composites were fabricated using both *hand*- and *machine*-compaction technique to study carbide-carbide based systems. Both these schemes were essen-

tially identical except for the compaction pressure employed during green-body preparation. The fabrication of these materials was to provide a basis for the mechanical, physical, and thermal property variations as functions of NbC, ZrC, and UC content. Salient features of the fabrication process and the compositional variations were as follows,

- Materials were fabricated using both low and high compaction pressures, corresponding to *hand* (suffix -H) and *machine* (suffix -M) compaction, respectively. The examination of physical properties, however, did not reveal significant differences between materials fabricated using the two schemes. Furthermore, the use of lower pressure compaction leads to a nominally simpler fabrication process. Thus, later materials were fabricated using only *hand* compaction.

- SiC-PP materials were the control samples fabricated using commercial acquired β-SiC.

- The 'PP' designation refers to 'polymer precursor' and specifically to allylhydridopolycarbosilane (AHPCS), which is used to generate the amorphous/nanocrystalline silicon carbide, a-SiC or n-SiC, matrix for our materials.

- The nominal volume ratios represent the initial mixtures and not the final volume fractions. The latter can be determined only by gravimetric analysis after all the re-infiltrations have been completed.

- The uranium carbide based material, UC-PP-H, was fabricated by a procedure that involved slurry-pyrolysis followed by crushing and compaction. Therefore, the concept of a nominal volume ratio does not apply. As for all other cases, the final constituent distribution can be determined only by gravimetry.

3.2.1 Uranium carbide based fabrication

To fabricate uranium carbide based materials, the as-received uranium carbide was directly mixed into the preceramic polymer. This processes was expected to yield a UC–SiC based fuel element. The process was similar to that explained in the previous section. However, it was observed that all UC compacted samples fell apart during the first run but were intact upon re-compaction. Figures 3.6(a) and 3.6(b) show the plugs processed after first and second compaction cycles, respectively.

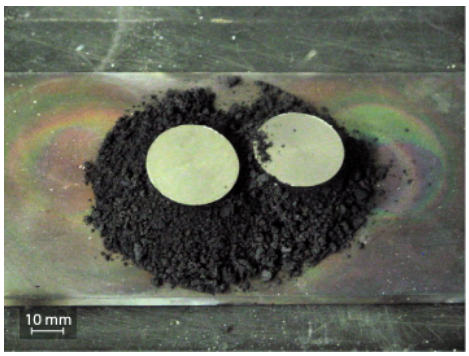

(a) Resulting plugs after first compaction using UC

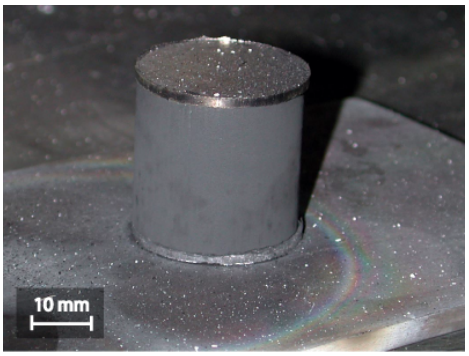

(b) Resulting plug after second compaction using UC

Figure 3.6: Fabrication attempt using UC as the base material. Pellets were pyrolyzed to 900 °C.

This required us to refine the fabrication process. Furthermore, it was found that while excessive ball milling led to very fine crushed powder, insufficient ball milling led to coarse metal particles. Both these conditions may lead to the disintegration of the pellets as shown in Fig. 3.7. Therefore, an iterative process was adopted to optimize the ball milling parameters.

In addition, it was suspected that these materials were oxidizing, which was confirmed later by XRD analysis (see Fig. 4.4(a) on page 39). During the first cycle, UC oxidized to UO_2 and was therefore unstable due to the resulting volume change. Upon re-compaction no further compositional change occurred and the material was stable.

Further investigation showed that environmental control in the box oven was lim-

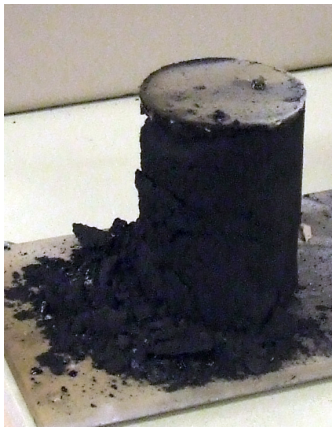

(a) Excessive milling of slurry led to instability in the pellet.

(b) Coarse metal reinforcement led to cracking of the pellet.

Figure 3.7: Disintegration of pellets due to incompatible reinforcement filler size obtained after ball milling.

ited and allowed oxidation to occur over long durations, especially when highly reactive species, such as UC, were present. This oxidation was not observed when SiC or other more stable species were processed. Furthermore, we were restricted to 900 °C for pyrolysis because of the furnace limitations. Additionally, since evidence of crystallization for AHPCS was reported near 1100 °C by Zunjarrao *et. al.* [80], it was decided to upgrade the furnace. The new tube furnace is shown in Fig. 3.8. At the inlet, an ultra high purity argon gas is passed through a combination of moisture and oxygen traps to ensure zero-oxidation due to impurities that may be present in the tanked gas. Also, steel tubing is used at the inlet to avoid contamination by air diffusion into the tubes. This tube furnace is capable of pyrolysis up to 1650 °C. Moreover, fast curing is possible with the current furnace. This capability was used to pyrolyse materials at 1 °C/min up to 650 °C, and at 3 °C/min up to 1150 °C for samples fabricated later.

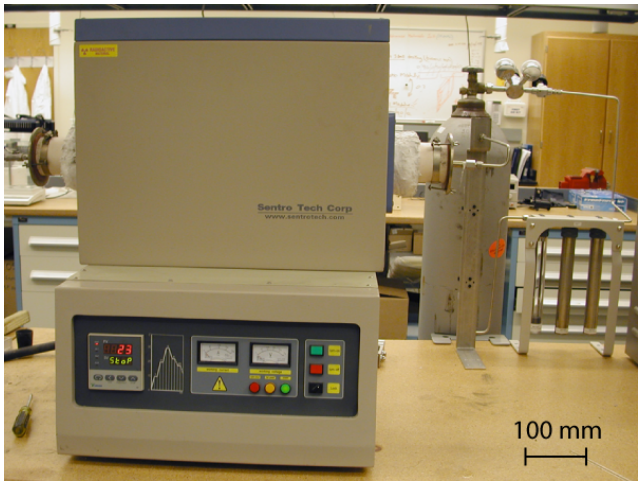

Figure 3.8: Setup used for inert gas pyrolysis up to 1150 °C. The furnace is capable of controlled heating to the maximum of 1650 °C.

3.3 Mixed-metal Carbide and Silicocarbide Composites

The final focus of this investigation is to fabricate mixed-metal carbides (U/Nb/Zr)C using the proposed technique. It is based on pyrolysis of a mixture of a metal with metal/metal-carbide and the polymer. The concept here is to form mixed-metal carbide or silicocarbide compositions contained within an SiC matrix, where the metal carbide or silicocarbide is generated by direct solid state reactions between the metal of interest (U, Nb, Zr, or combination) and the preceramic polymer.

Powders for metallic Nb, −325 mesh, and Zr, 50 mesh, were acquired from Alfa Aesar (Ward Hill, Massachusetts, USA), and Atlantic Equipment Engineers (Bergenfield, New Jersey, USA), respectively. However, since the availability of uranium powder is limited, a hydriding procedure was adopted to generate UH_3 flakes from a block of depleted uranium. Next, this UH_3 was used as the source for uranium. UH_3 is highly pyrophoric, but, it is an interesting substance, since it is the intermediate in the preparation for most uranium compounds for which uranium is the starting material. UH_3 starts dissociating at 400 °C, and later disintegrates easily with rising temperature [22]. This makes it an extremely interesting for the current fabrication process due to the possible solid state reactions with a combination of other metals

and the current precursor during pyrolysis.

We used UH_3 and the polymer precursor to prepare UC in the final composition. Typically, there are several ways of fabricating UC: (i) by direct reaction of elements during arc welding, (ii) by reaction of uranium with hydrocarbon gases (usually methane), (iii) by reaction between UO_2 and carbon [22]. The powders produced by any of the above mentioned method are highly reactive and must be stored in an inert environment. However, in our technique, uranium carbide is obtained in the final composite due to a reaction that takes place during the regular pyrolysis cycle. The innovation of this procedure is in the use of polymer infiltration and pyrolysis to achieve UC in the composite. The schematic of the proposed technique is shown in Fig. 3.9.

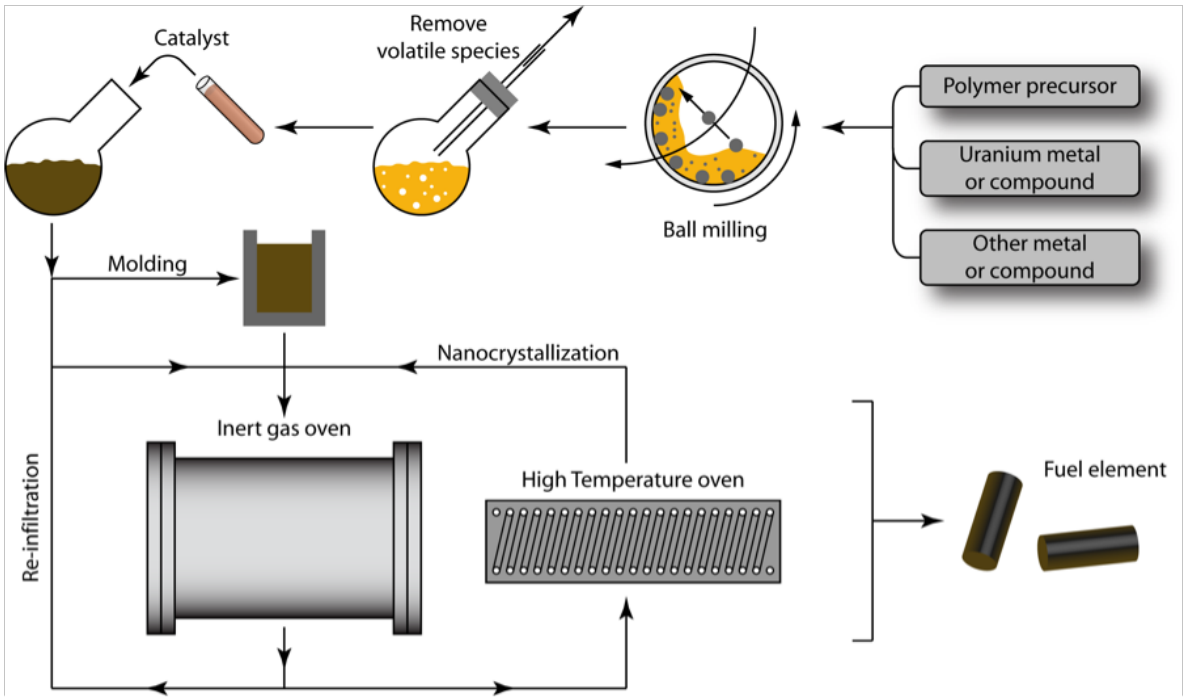

Figure 3.9: The schematic of the proposed technique to produce nuclear fuel.

Outline of the processing steps and optional variations for fabricating nuclear fuel are given as follows:

1. Start with a mixture of polymer precursor for silicon carbide (or another ce-

ramic) and a uranium containing powder (metal, hydride, oxide, etc.). Other refractory metals or compounds may be added (e.g. Zr, Nb, or Hf based). The process can be used with other fuels compositions of interests including those based on transuranics.

2. Mechanically mix initial constituents using a ball mill or another scheme.

3. (Optional) Remove volatile species from the mixture. These could be from the polymer precursor, or could be mixing aids added in previous step.

4. (Optional) Add catalyst to start precuring of the mixture.

5. For the first cycle only, pyrolyze the slurry in an inert gas oven. This will lead to a foamy solid mass. The uranium (or other metals) would convert to a carbide, silicide or silico-carbide through solid state reactions. The polymer precursor would convert to silicon carbide (or other ceramic based on selection of the precursor).

6. For the first cycle only, crush the foamy mass and bind the resulting powder with small amount of polymer precursor. Mold in a press to form a green body.

7. Conduct single or multiple polymer infiltration and pyrolysis cycles.

8. (Optional) Subject the formed shaped to a higher temperature oven to nanocrystallize the silicon carbide (or other ceramic) matrix.

A hydriding setup, shown in Fig. 3.10, was built inside the glove box under a sealed inert environment to avoid any oxidation during preparation. The use of a sealed inert environment also prevents oxidation after hydriding has taken place. Typically, hydriding involves heating the uranium block to about 200 °C under constant hydrogen flow. Uranium metal reacts rapidly with hydrogen to form uranium hydride. This results in complete disintegration of the metallic structure due to volumetric

expansion (uranium has a density of 18.9 g/cm^3, while uranium hydride's density is 11.4 g/cm^3) during the chemical conversion. A gas mix of 5% hydrogen in argon was used to obtain the hydrogen flow over the uranium block. The amount of gas flow was monitored by a bubbler in the exhaust outlet. The glass flask that contained the uranium block was heated by an analog controlled mantle heater. Metal tubing was used for both gas inlet and exhaust. A subsequent de-hydriding step, to acquire uranium, is not required as that would occur during the pyrolysis procedure. Figure 3.10 shows a photograph of the uranium block undergoing the hydriding process. Initially about 200 g of UH_3 was produced using the hydriding process for material fabrication.

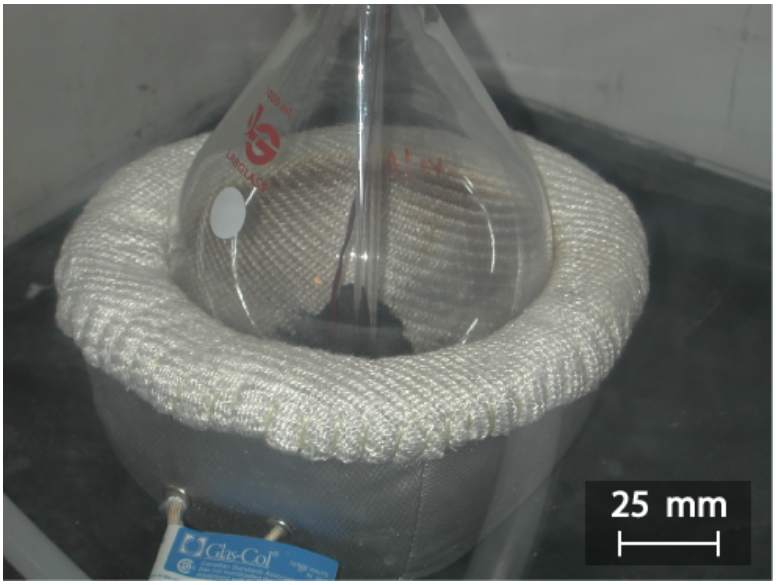

Figure 3.10: Setup for hydryding of uranium to produce UH_3.

A list of materials fabricated to study mixed-metal carbides/silicides are listed in Table 3.2.

No.	Material	Composition	Form
1	UH_3-PP	UH_3 and PP	Powder & Pellet
2	UH_3-Nb-PP	UH_3, Nb and PP	Powder
3	UH_3-Zr-PP	UH_3, Zr and PP	Powder
4	Nb-PP	Nb and PP	Powder
5	Zr-PP	Zr and PP	Powder
6	UC-Nb-PP	UC, Nb and PP	Pellet

Table 3.2: Fabrication scheme and composition of mixed-metal carbide/silicide based materials.

CHAPTER 4

ANALYTICAL AND PHYSICAL CHARACTERIZATION

4.1 Analytical Characterization

4.1.1 Oxide materials

The starting material for our oxide based composites was either U_3O_8 or UO_2. The ceramic composite fabricated using U_3O_8 showed a color change. After the first pyrolysis, the pellet came out as a brown cinnamon colored solid. Figure 4.1 shows the as-received U_3O_8 and the pyrolyzed powder obtained after the first heating cycle. This change in color indicated a chemical conversion. Therefore, in order to investigate the microstructure and formation of new chemical species, due to *in situ* reactions, the fabricated materials were studied using powder X-ray diffraction (XRD). These measurements were performed on a Phillips PW1729/APD3520 diffractometer with CuKα radiation ($\lambda = 0.154$ nm) operating at 40 kV and 30 mA. Peaks in the XRD patterns were identified using the JCPDS-ICDD database.

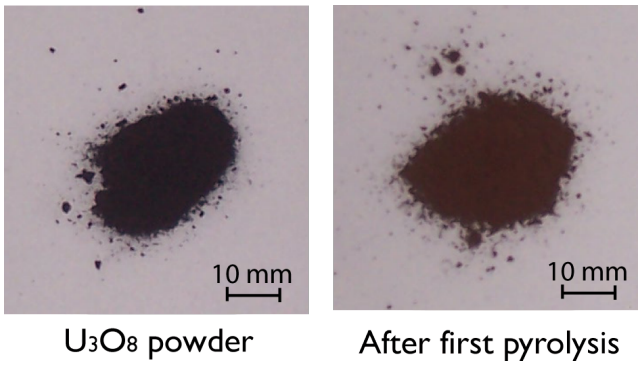

Figure 4.1: Color change of parent uranium powder after first pyrolysis.

Figure 4.2 shows the diffraction patterns obtained for as-received U_3O_8 powder

and ball milled slurry powder after one cycle of pyrolysis. The diffraction peaks in the pyrolyzed slurry pattern were mostly dominated by the presence of UO_2 providing evidence of the conversion of U_3O_8 to UO_2 during the first pyrolysis cycle. This conversion has been widely studied [81–83]. Since the pyrolysis was carried out in an inert environment, it is highly likely that the reduction took place due to the presence of hydrogen gas that evolves during the pyrolysis of the precursor. In the presence of hydrogen this reduction can take place in the temperature range of 400–600 °C [82,83]. However, this process is highly affected by the powder properties such as BET surface area and size. A more detailed understanding of these conversion is needed. Nonetheless, the conversion of U_3O_8 to UO_2 is favorable given the stability of the latter at higher temperatures.

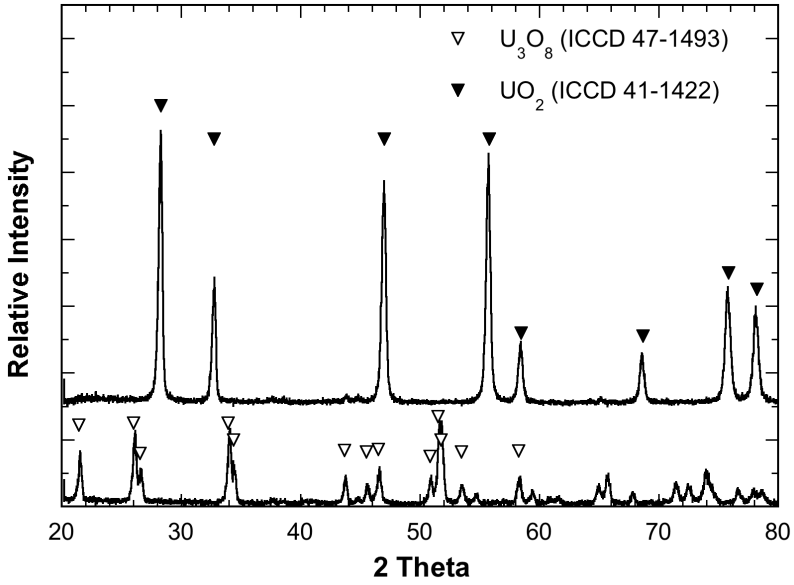

Figure 4.2: X-ray diffraction pattern for as-received U_3O_8 and after first temperature cycle to 900 °C.

Scanning electron microscopy (SEM) was performed on *a*-SiC–U_3O_8–A and *a*-SiC–U_3O_8–B after three and eight reinfiltrations. It can be observed from these microscopy images, shown in Fig. 4.3, that the distribution of U_3O_8 (actually UO_2) was highly uniform and pores were not visible even after the third reinfiltration at this scale.

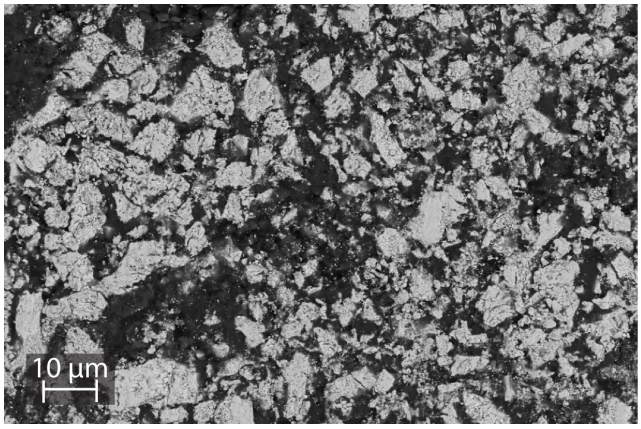

(a) (a-SiC–U_3O_8–A) After 3^{rd} reinfiltration

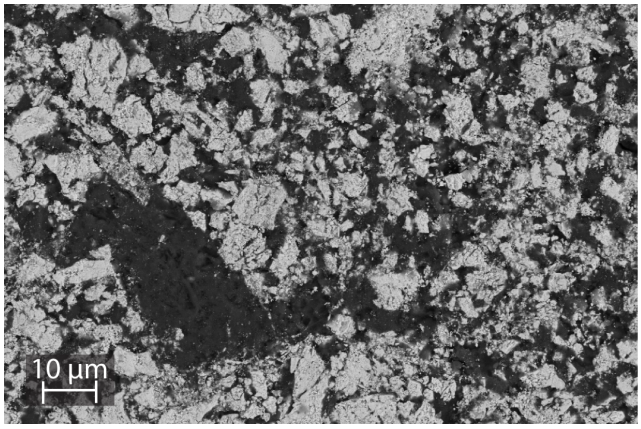

(b) (a-SiC–U_3O_8–A) After 8^{th} reinfiltration

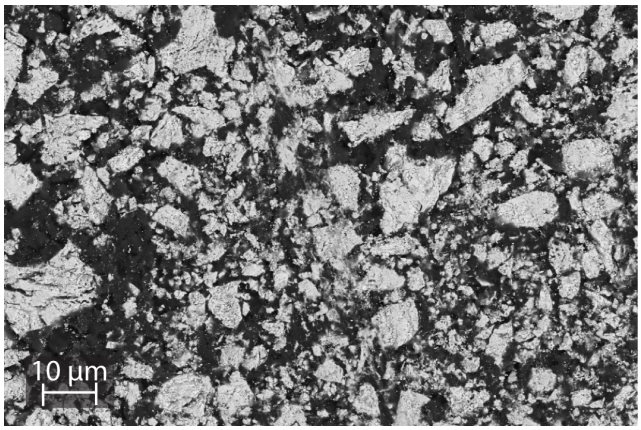

(c) (a-SiC–U_3O_8–B) After 8^{th} reinfiltration

Figure 4.3: Uranium ceramic composite after 3^{rd} and 8^{th} reinfiltrations. The bright portion of the micrograph represents UO_2 and the dark regions represent SiC matrix phase.

4.1.2 Carbide materials

In order to investigate niobium, zirconium, or uranium based metal carbides it is essential to first understand the stability of these carbides during pyrolysis in the presence of AHPCS, the precursor for SiC. This was done by adding a small amount of the metal carbide of interest to sufficient liquid polymer precursor and then extensively ball-milling this to produce a slurry. The slurry was pyrolyzed and the resulting materials were characterized using a Bruker D8 advance X-ray powder diffractometer. Table 4.1 lists the carbide based materials prepared during this study for X-ray diffraction characterization.

Constituents (Polymer precursor &)	**Pyrolysis Temperature** (°C)	**Composite Constituents** (as observed in XRD pattern)
UC	900	UO_2, *a*-SiC
UC, NbC	1150	UC_2, UO_2, NbC, *a*-SiC
NbC, ZrC	1150	ZrC, NbH_2, NbC, *a*-SiC
ZrC	1650	ZrC, SiC

Table 4.1: Compositions prepared for stability analysis of the metal carbides with AHPCS during pyrolysis.

Figure 4.4(a) shows the diffraction pattern of the crushed powder after two pyrolysis cycles to 900 °C during uranium carbide based pellet fabrication. It was observed in the diffraction pattern that the uranium carbide was completely converted to UO_2. This also explained the failing pellet fabrications observed in Fig. 3.6. There is an approximate 30% increase in volume for UC—UO_2 conversion. Once the conversion was complete, we were able to fabricate solid pellets with ease.

Separate slurries of 50% v/v mix ratio of UC and NbC with AHPCS, NbC and ZrC with AHPCS, and ZrC with AHPCS, were pyrolyzed. However, the slurry with ZrC was pyrolyzed up to 1650 °C. Figures 4.4(b) and 4.5 show diffraction patterns obtained from the pyrolysis of these compositions. It should be noted that SiC is also formed, but is not detected by XRD due to the amorphous microstructure.

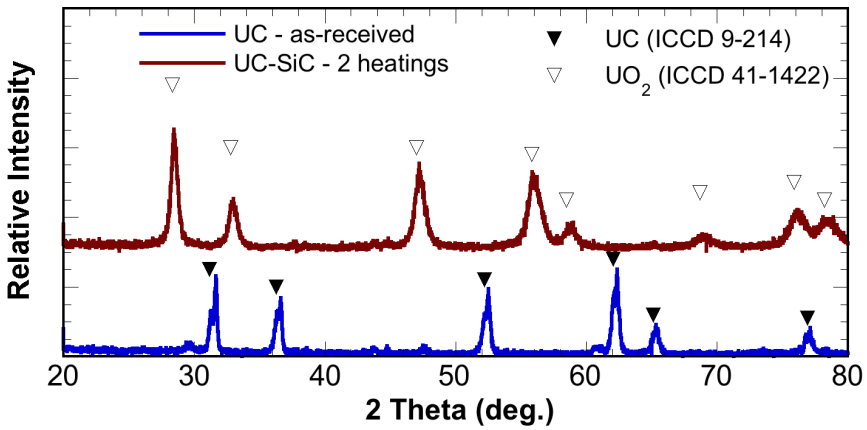

(a) X-ray diffraction pattern for as-received UC and after second temperature cycle to 900 °C, showing its complete conversion to UO_2.

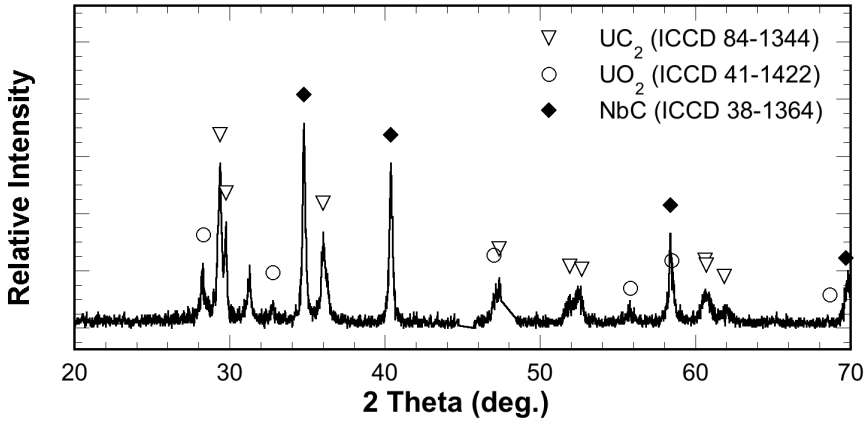

(b) X-ray diffraction pattern for UC and niobium carbide-AHPCS pyrolysis to 1150 °C, showing presence of UC_2, UO_2, and NbC.

Figure 4.4: X-ray diffraction data for pyrolyzed zirconium carbide-AHPCS slurry.

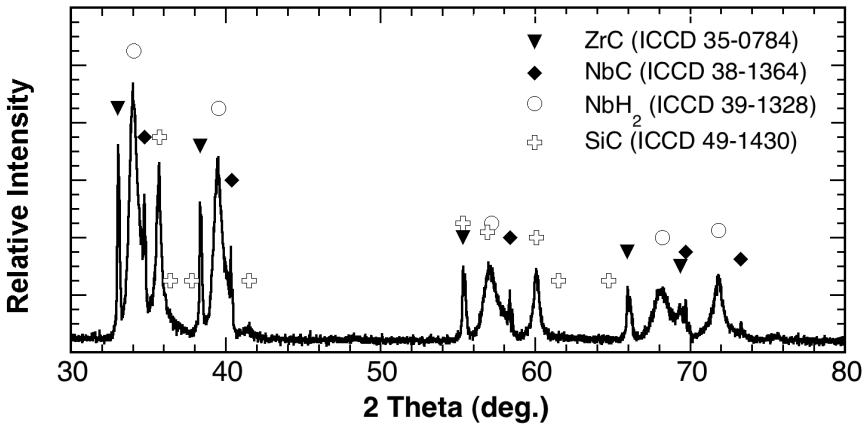

(a) XRD data for zirconium carbide and niobium carbide-AHPCS pyrolysis to 1150 °C, showing presence of ZrC, NbH_2, and NbC

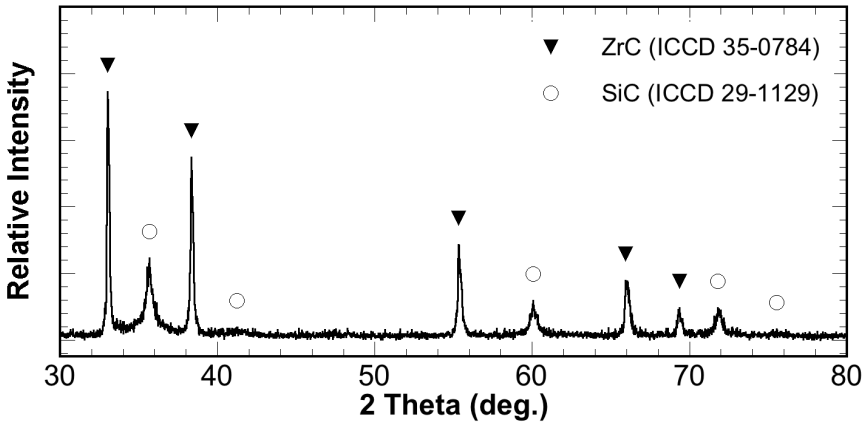

(b) XRD data for zirconium carbide-AHPCS pyrolysis to 1650 °C, showing presence of ZrC and cubic SiC

Figure 4.5: X-ray diffraction data for pyrolyzed zirconium carbide-AHPCS slurry. Zirconium carbide does not react with either niobium carbide or the polymer precursor even at higher temperatures. The slurry pyrolyzed to 1650 °C shows the presence of crystalline SiC.

Figure 4.4(b) shows XRD data from a region that has excess carbon and thus exhibits the formation of UC_2 from UC. However, the conversion to UO_2 is also prominent. An unidentified peak at $2\theta \approx 31.3°$ is also observed.

Figure 4.5(a) shows the pattern for ZrC-NbC pyrolysis with AHPCS. Zirconium carbide did not react with AHPCS or NbC, however, niobium carbide reacted with AHPCS to form NbH_2. In another X-ray diffraction pattern of zirconium carbide pyrolyzed to 1650 °C, silicon carbide is apparent now in crystalline form and zirconium carbide stays as a stable component (shown in Fig. 4.5(b)). This snapshot of the zirconium carbide's behavior could be instrumental in explaining the lowest biaxial strength (discussed in chapter 6 on page 60) observation amongst the various refractory metal carbide plug combinations fabricated in the current study.

4.1.3 Mixed-metal carbides/silicides

Separate slurries were prepared with either niobium, zirconium or uranium hydride (equivalent to using uranium metal) with AHPCS. The slurry was pyrolyzed and the resulting material was characterized using XRD. The objective was to investigate stability and possible in-situ solid-state reactions. Table 4.2 is a list of materials fabricated for this analysis. Figure 4.6 shows diffraction patterns obtained from two regions of pyrolyzed Nb-AHPCS. These regions correspond to AHPCS-rich and niobium-rich regions, respectively, and represent different local compositions of Nb:Si:C leading to potentially different solid-state reactions. Figure 4.6(a) shows XRD data from a region that has excess carbon and thus exhibits the formation of NbC with no free Nb. Again, SiC is also formed, but is not detected by XRD due to the amorphous microstructure. Figure 4.6(b) is generated from a region that has excess niobium and thus exhibits the formation of NbC along with excess free Nb. This figure also shows some peaks that could not be identified in the currently available 2004 JCPDS database. These do not correspond to any carbides or silicides of niobium. Nor do

they correspond to possible contaminants from the tungsten carbide ball mill or the alumina crucibles. It is suspected that these correspond to ternary carbides/silicides that are formed due to *in situ* solid-state reactions.

Constituents (Polymer precursor &)	**Pyrolysis Temperature** (°C)	**Composite Constituents**
UH_3	1150	UC, *a*-SiC
UH_3, Nb	1150	UC, Nb, NbC, *a*-SiC
UH_3, Zr	1150	UC, ZrC, *a*-SiC
Nb	1150	Nb, NbC, *a*-SiC
Zr	1150	ZrC, Zr_2Si, *a*-SiC

Table 4.2: Compositions prepared for stability analysis and solid-state kinetics of the mixed-metal carbides/silicides with AHPCS during pyrolysis. Few unidentified peaks were also observed in all of these measurements.

Similarly, a slurry of Zr with AHPCS was also pyrolyzed. The diffraction pattern of zirconium pyrolyzed with AHPCS results in the formation of zirconium silicide, Zr_2Si, and zirconium carbide as shown in Fig. 4.7. This figure also shows some peaks that could not be identified in the currently available 2004 JCPDS database. It was confirmed that these do not correspond to any possible contaminants from the tungsten carbide ball mill or the alumina crucibles. It is suspected that these correspond to ternary carbides/silicides that are formed due to *in situ* solid-state reactions. However, the presence of quartz, SiO_2, is suspected.

Uranium hydride was used as the source for uranium metal for our mixed-metal carbide/silicide studies. Slurries were prepared by mixing UH_3 with AHPCS, niobium powder with AHPCS or zirconium powder with AHPCS. The formation of uranium carbide in the final composite was confirmed in all of these compositions by performing X-ray diffraction studies on the crushed powder after the first pyrolysis. Figure 4.8 shows the diffraction patterns, which indicates the presence of uranium carbide in each fabrication and unidentified peaks were also observed. Such peaks could be due to the presence of an unknown silicide or silico-carbide phases and therefore is considered

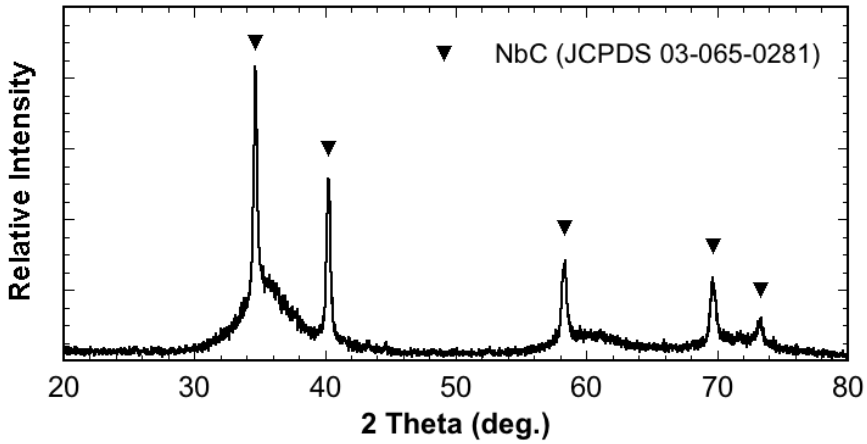

(a) XRD data for AHPCS-rich region showing presence of NbC and no free Nb

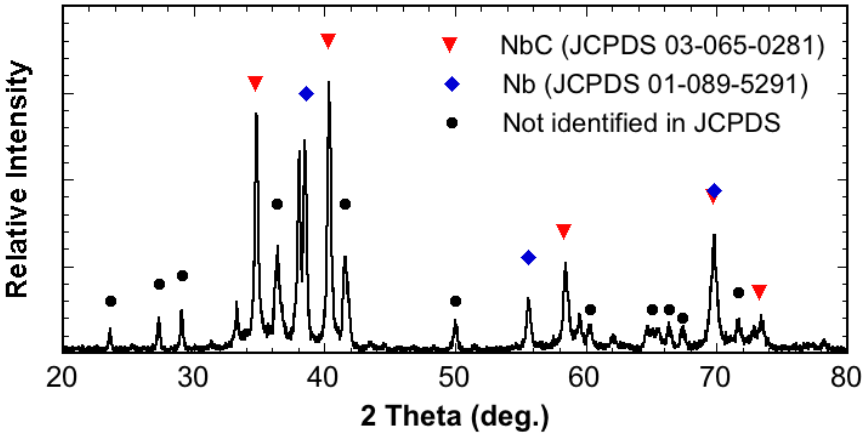

(b) XRD data for niobium-rich region showing presence of NbC, free Nb, and some unidentified material(s)

Figure 4.6: X-ray diffraction data for pyrolyzed niobium-AHPCS slurry showing evidence of *in situ* solid-state reactions.

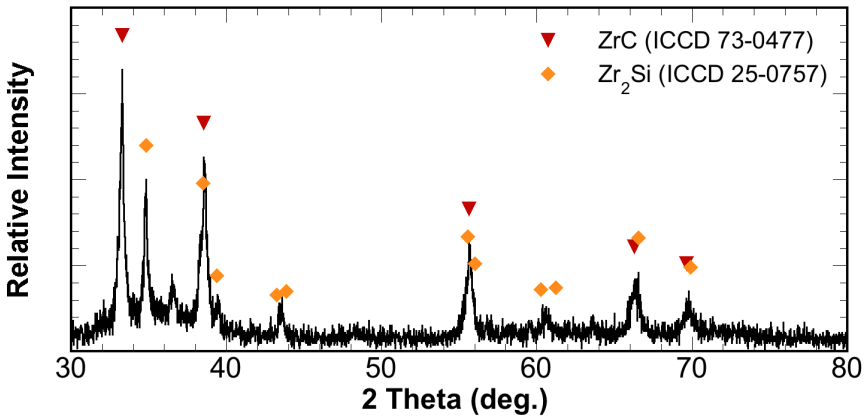

Figure 4.7: XRD data for zirconium-AHPCS pyrolysis, showing presence of ZrC and Zr_2Si.

favorable for our process. The commercial development of uranium monocarbide has been extremely difficult because below 1200 °C the homogeneity range of UC is less than 0.05 wt%, apparent in the phase diagram shown in Fig. 4.9. Our fabrication technique successfully achieves this by the pyrolysis method. Once formed, UC is stable from room temperature to its melting point of about 2560 °C [22].

4.2 Density and Porosity Measurements

The density and porosity of the fabricated materials was determined after the 8^{th} reinfiltration using the buoyancy method. First the specimen was dried at 120 °C for 12 hours, until it reached a constant mass, and then cooled to room temperature in a desiccator. The dry mass of the sample, m_1, was recorded. Subsequently, the dried sample was saturated using ultra-high purity water to fill all the open pores. A few drops of Photo-Flo® (Kodak Corporation, Rochester, New York, USA) were added to reduce the surface tension of water and aid in saturation. A four-hour evacuation cycle was employed with intermittent purges at every thirty minutes to release trapped air. The apparent mass of the saturated sample, m_2, was then determined using a density determination kit. The temperature of the saturation liquid was also recorded to correct for variations in the density of water, ρ_{fl}, as a function of temperature.

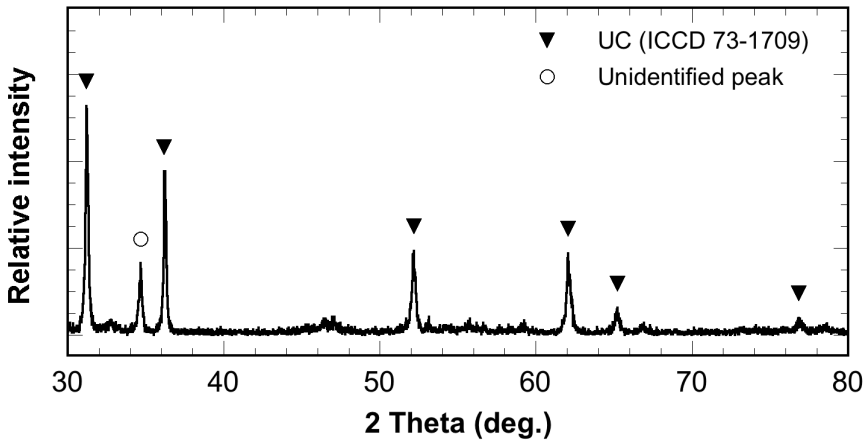

(a)

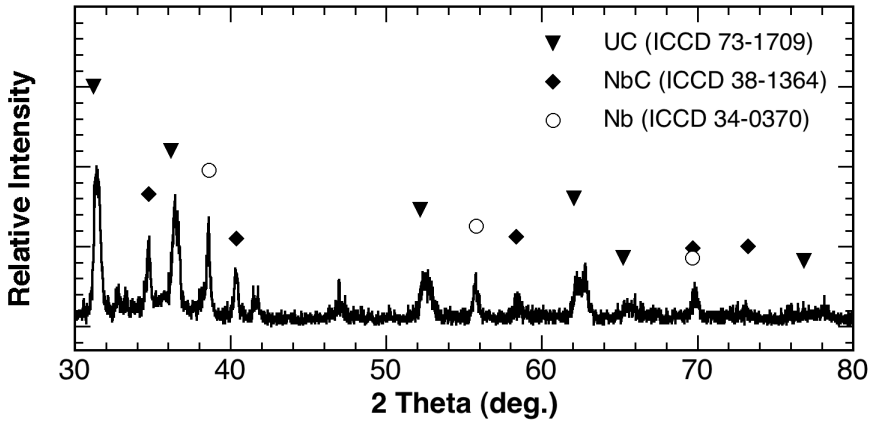

(b)

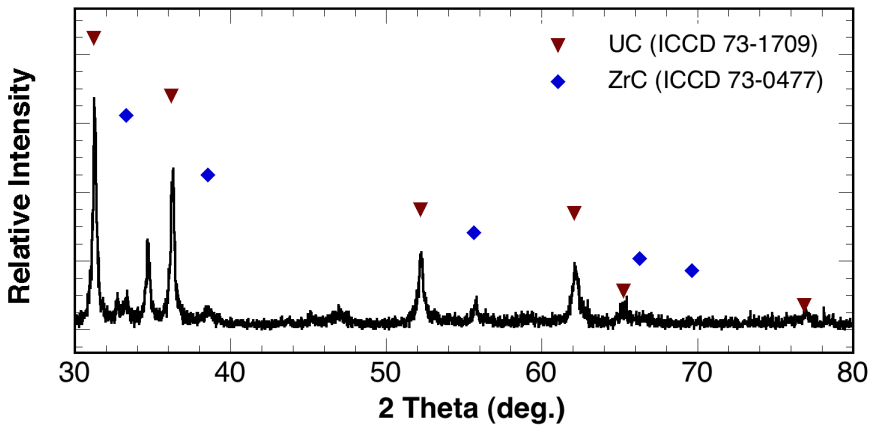

(c)

Figure 4.8: X-ray diffraction pattern observed on the powder obtained after one heating cycle of the slurry of AHPCS alongwith (a) UH_3 powder, (b) UH_3 and Nb powder, and (c) UH_3 and Zr powder.

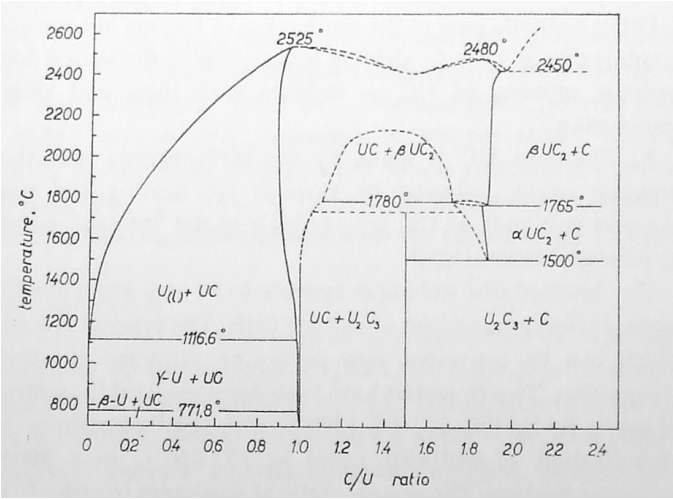

Figure 4.9: Phase diagram of the uranium-carbon system [22].

Finally, the mass of the saturated sample, m_3, was determined by weighing in air. Any liquid that remained on the surface of the sample was removed with a damp sponge and the operation was performed quickly, to avoid loss of mass due to evaporation. Subsequently, the bulk density, ρ_b, was calculated as,

$$\rho_b = \frac{m_1}{m_3 - m_2}\rho_{fl}, \tag{4.1}$$

and the open porosity, π_a, in vol. % was calculated as,

$$\pi_a = \frac{m_3 - m_1}{m_3 - m_2} \times 100. \tag{4.2}$$

Bulk densities and open porosities of the oxide based pellets after the 8^{th} reinfiltration are listed in Table 4.3. The PIP processing generated closed pores in the consolidated pellets and therefore the bulk densities of the composites obtained were lower than their true densities. The true density (particle density) of the amorphous SiC (after pyrolysis to 900 °C) prepared during this study was 2.67 g/cm^3. The true densities of polymer derived SiC have been found to vary from 2.7 g/cm^3 at 900 °C to 3.2 g/cm^3 at 1650 °C [80]. The bulk density and porosity values for both *a*-SiC–

U_3O_8–A and *a*-SiC–U_3O_8–B were found to be close. It is possible that the modified reinfiltration process, as for *a*-SiC–U_3O_8–A, impeded the densification leading to lower bulk density and higher open porosity, as indicated in Table 4.3. Given the scatter in data, however, it is not possible to make this claim unambiguously.

Material	**Bulk density** ρ_b (g/cm^3)	**Open Porosity** π_a (%)
(*a*-SiC)	2.21±0.01	3.39±1.14
(*a*-SiC)–U_3O_8–A	4.58±0.06	2.77±1.14
(*a*-SiC)–U_3O_8–B	4.70±0.06	1.94±0.56

Table 4.3: Density and porosity of the samples after 8^{th} reinfiltration.

During fuel fabrication using sintering, the fuel pellets are produced to $\sim 90\%$ of the theoretical density. The deliberate introduction of residual porosity is desired in fresh fuel to accommodate fission product swelling and redistribution [84]. Similarly, it is hypothesized that the presence of pores, in the current fabrication process, is beneficial and may decrease the effect of irradiation swelling of SiC.

For carbide materials, the bulk density after the 8^{th} reinfiltration was measured using the buoyancy method as well as using the Ultrapycnometer 1000 (Quantachrome Instruments, Pittsburgh, PA, USA). Helium was used as the purge gas for the instrument. The sample, after dry mass measurement, was placed in the measurement cell of the pycnometer. The pycnometer was purged with helium for 5 minutes, and then it was programmed to average 3, out of a maximum of 6, readings with standard deviation less than 0.01%. The pycnometer measures the volume of the material placed in the cell and using the dry mass, m_1, the bulk density can be calculated. Bulk density values, as determined using helium pycnometry, are listed in Table 4.4, and are in good agreement with those determined using the buoyancy procedure.

No.	Material	Buoyancy Method		Pycnometry
		Bulk Density (g/cc)	Open Porosity (%)	Bulk Density (g/cc)
1	SiC-PP-9010-H	2.69	7.54	2.57
2	SiC-PP-9010-M	2.68	7.47	2.64
3	NbC-PP-9010-H	4.77	10.48	4.47
4	NbC-PP-9010-M	5.07	7.52	4.88
5	ZrC-PP-9010-H	4.16	7.20	3.93
6	ZrC-PP-9010-M	4.39	10.47	4.27
7	NbC-SiC-PP-454510-H	3.75	7.79	3.71
8	ZrC-SiC-PP-454510-H	4.53	13.33	4.44
9	ZrC-NbC-PP-454510-H	3.57	2.84	3.45
10	UC-PP-H	4.20	8.49	4.07

Table 4.4: Physical characteristics of carbide based materials.

CHAPTER 5

THERMAL CHARACTERIZATION

Thermal conductivity (λ) is an intrinsic property of a material and an extremely important parameter in advanced designs and modern material fabrications. A high thermal conductivity is a desirable property during nuclear fuel selection [85]. Fundamentally, thermal conductivity is a measure of the heat flux that flows through the material for a certain temperature gradient. Thermal conductivity of a material depends on various factors including its structure (crystal plane), temperature (surrounding), phase, and form. For example, pure crystalline substances may exhibit different thermal conductivities along different crystal axes due to differences in phonon coupling along a given crystal axis, and the thermal transport in nanomaterials is different from that in bulk materials due to the strong boundary scattering of energy carriers (phonons or free electrons). In silicon carbide, the matrix material phonons are the primary thermal transport mechanism. Therefore, the conductivity is higher for crystalline materials and is dependent on ambient temperature conditions.

5.1 Measurement Techniques

Measurement of thermal conductivity involves two processes: *heating* and *sensing*. In general, there are several techniques to achieve these. Each of them suitable for only a limited range of materials, depending on the thermal properties, geometry and the surrounding temperature. These can be broadly classified into steady-state and non-steady-state techniques [86].

In general, steady-state techniques are performed when the material that is an-

alyzed, is in equilibrium. This provides more precise measurement (theoretically) but usually takes a long time to reach the required equilibrium. For such measurements, the ends of the sample are maintained at different temperatures, and after steady state is achieved, the temperature variation across the sample length is measured. However, since these measurements transfer heat through conduction, they suffer from high contact resistance, surface finish and flatness of the specimen (the resistance between the source or sink, with that of the sample) and it restricts this technique to provide precise data. Heat loss models [87] are incorporated, in addition to such measurements, to account for external losses.

Moreover, using traditional techniques, it is difficult if not impossible to directly measure the thermal conductivity of microscopic structures and features such as fibers, fiber coatings, whiskers, grain boundaries, grains, powder particles, functionally gradient coatings and intergranular phases, because the majority of supplied energy is used up for heating up the heating/sensing element [88]. Therefore, it has been a topic of considerable research to obtain a method that can project the thermal conductivity of a material with precision. Also, because of the geometrical and phase variations, non-contact methods are highly desirable.

Amongst non-steady-state techniques, hot-wire, laser-flash, and 3-omega method are widely used. The hot-wire method is based on radial heat flow through a specimen where the heater and sensor wires are embedded within the specimen. Since, it is radial flow technique, isotropic specimens are required. It is commonly used with large specimens of refractory material. The technique has been conventionally used to measure properties of liquids and plastics materials of relatively low thermal conductivity. Recent modification of this technique is the "probe" method. This configuration is particularly practical where the specimen conductivity is determined from the response of a "hypodermic needle" probe inserted in the test specimen. Thus the method is conveniently applied to low-conductivity materials in powder or other

semi-rigid form [89].

Three-omega is a very popular modern contact technique [90]. It is used for direct measurement of thermal conductivity. This technique was originally reported by David Cahill in 1989. It utilizes an AC heating current and a lock-in amplifier to directly measure thermal conductivity of dielectric materials. A small line heater is put on the sample surface by sputtering through a mask or photolithography. The combined heater/sensor element is a single wire intimately attached to the surface of the specimen. An electrical current at angular frequency ω is driven through the wire, causing Joule heating at a frequency 2ω. The temperature oscillations of the wire are measured by the third harmonic of the voltage across the wire with a lock-in amplifier, hence the name 3-ω method. Samples with complex geometry can be tested as long as a heater/thermometer can be placed on the surface. This method uses a radial heat-flow geometry. Thermal conductivity is determined by measuring the amplitude and phase of third-harmonic temperature oscillations in the wire at two different AC driving frequencies. Since the thermal wave measurement depth is controlled by the heating frequency, thermal conductivity of coatings and thin films can be studied. Therefore, this technique has been used with both bulk and thin-film amorphous dielectric solids. The three-omega method is fast and accurate compared to other thermal conductivity measuring techniques. However, sometimes thermo-reflectance method is preferable over three-omega for nano-thick films [91]. This is a similar method as three-omega with the only difference being a small temperature excursion (ΔT) about average temperature T, that is related linearly to a fractional change (ΔR) in reflectance R.

High temperature thermal conductivity can be obtained by laser flash technique using the formula, $\lambda = \alpha C_p \rho$, where α is the thermal diffusivity, C_p the specific heat and ρ is the bulk density of the sample. For a two phase system rule of mixtures is used to calculate the specific heat capacity based on the volume fraction of individual

contents. Laser-flash method are non-contact techniques and are generally used to measure thermal conductivity of dense ceramic materials. Most non-contact measurements are based on photothermal techniques utilizing modulated or pulsed laser beams for the determination of thermal conductivities.

Flash methods are generally employed for single layer specimens. In these methods, a flat specimen is heated on one surface with a laser pulse. This causes temperature rise on the rear side of the sample due to diffusivity. A sensor or array of sensors then detects the change in temperature over time on the opposite surface. This technique has been successfully used to measure thermal conductivity of liquids and pastes as well [92, 93]. This method is also a non-contact method and is widely used because of the small specimen size required and the ease and rapidity with which measurements can be taken. The disadvantage of this method is that density and heat capacity also need to be known or measured to calculate thermal conductivity. Therefore, these tests usually involve diffusivity measurement by calculating $t^{\frac{1}{2}}$ measurement from the sample [85, 88, 94]. However, the use of indirect transient methods may yield questionable results in complex composites or layered ceramics where there are unusual patterns of heat flow within the body of the material [86].

5.1.1 Axial flow method

In the current study, the room temperature thermal conductivity, λ, was measured using a steady state axial flow setup [95], shown in Fig. 5.1, using cylindrical samples of ϕ 25 $\times$ 5 mm. The heat flow was measured using eight T-type, high precision copper-constantan thermocouples, located in the hot and cold side of the sample on pure copper rods. Heat loss from the setup through conduction in the radial direction is prevented by thick teflon cylinder insulation. The hot side temperature was controlled using Omega CN132 temperature/process controller and the cold side using an analog controlled Cole Palmer chiller, model:12750-00. Source and sink of heat

are located far apart so that the masured temperature represents the temperature of the whole cross-section at that location. A thin layer of high thermal conductivity paste, Omegatherm 201, was used to minimize the thermal resistance between the copper rods and the sample. Data was recorded using a Fluke 53 series II digital storage thermometer, after steady state conditions had been achieved in ≈20 hours. Figure 5.2 shows a typical data set that was recorded. The hot and cold side linear curves were extrapolated to determine the temperatures, T_{hot} and T_{cold}, at the specimen interfaces. Equation 5.1 is used to calculate the heat flow, Q, on both sides of the specimen, which is represented as Q_{hot} and Q_{cold}. Subsequently, the thermal conductivity, of the sample is determined using the Fourier law of heat conduction, as given in Eqn. 5.2.

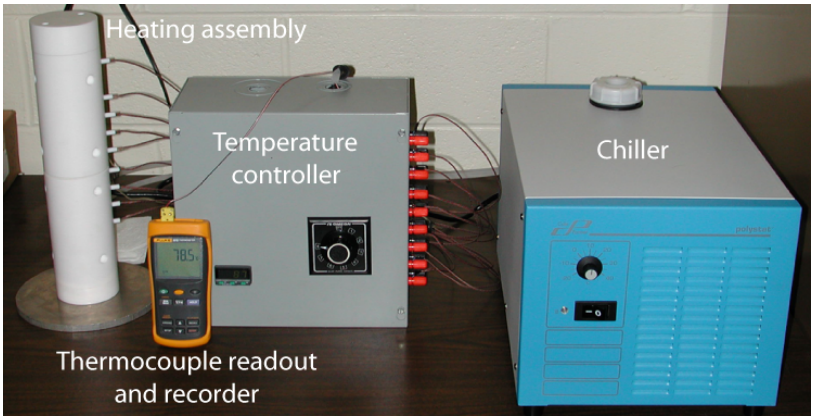

Figure 5.1: Axial heat flow setup for measuring room temperature thermal conductivity.

$$Q = -\lambda A \left(\frac{\Delta T}{\Delta Z} \right) \tag{5.1}$$

$$\lambda_{sample} = \frac{(Q_{hot} + Q_{cold}) L_{sample}}{2 A_{sample} (T_{hot} - T_{cold})} \tag{5.2}$$

The results obtained for room temperature thermal conductivity measurements are listed in Table 5.1. It should be noted that the values of thermal conductivity listed in Table 5.1 are rather low, especially from the perspective of a nuclear fuel. Although

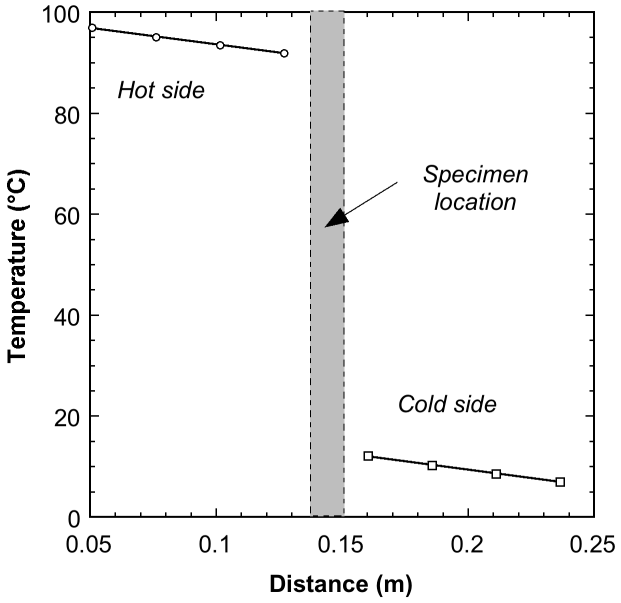

Figure 5.2: Typical thermocouple data at steady state heat conduction stage.

the thermal conductivities shown by the carbide materials are higher than oxide materials, it is still not as high as required for a nuclear fuel. Normally, this would be a cause for concern as low values of thermal conductivity can lead to greater center-line temperatures and reduced thermal shock performance. In this case, however, the low values of thermal conductivity is almost entirely due to the presence of the amorphous silicon carbide matrix, a-SiC. In fact a heat-treatment for nano-crystallization leads to a *significant* increase in the thermal conductivity, as illustrated in Table 5.2.

In the current study, room temperature measurements were carried out using an in-house axial flow meter. However, since it is essential to perform such measurements at higher temperatures to analyze in-service performance these fuels, it would be worth measuring thermal conductivity using a laser based technique with high temperature capabilities. Variation of thermal conductivity due to the changes in the porosity levels must also be studied since the porosity in such fabrication affects the density as well as the convection based conductivity.

Material	**Thermal Conductivity** (W/m-K)
SiC-PP-9010-H	7.05
(a-SiC)–U_3O_8–A*	1.55
(a-SiC)–U_3O_8–B*	1.08
NbC-PP-9010-H	4.14
NbC-PP-9010-M	4.09
ZrC-PP-9010-H	4.00
ZrC-PP-9010-M	6.52
NbC-SiC-PP-454510-H	6.67
ZrC-SiC-PP-454510-H	5.29
ZrC-NbC-PP-454510-H	5.28
UC-PP-H*	1.78

Table 5.1: Room temperature thermal conductivity of the carbide based materials processed to 1150 °C, determined using the axial heat flow setup. Please note that the SiC-PP materials were the control samples fabricated using commercial acquired β-SiC, and uranium carbide was converted to UO_2 during its pyrolysis as seen in Fig. 4.4(a). *represents materials pyrolyzed to 900 °C.

Material	**Processing Temperature**	**Thermal Conductivity** (W/m-K)
SiC-PP-9010-H	1150 °C	7.05
SiC-PP-9010-H	1600 °C	192.72

Table 5.2: Heat treatment at 1600 °C for four hours leads to an ∼2600% increase in the thermal conductivity due to amorphous-to-nanocrystalline conversion.

5.2 Factors Affecting Thermal Conductivity

The thermal conductivity of a single component system is very well understood theoretically, but in real life situations, every composition is heterogeneous and composed of more than one component. Variation of thermal conductivity due to the presence of the secondary component has also been widely studied in the past [41, 96, 97]. The conductivity of the composite, assuming that the phases lie in series or in parallel direction to the direction of heat flow, is given as:

$$\lambda_{\parallel} = \lambda_1\phi_1 + \lambda_2\phi_2 \tag{5.3}$$

$$\lambda_{\perp} = \{\phi_1/\lambda_1 + \phi_2/\lambda_2\}^{-1}. \tag{5.4}$$

where $\lambda_{\parallel}$ is the thermal conductivity of the composite for parallel arrangement of the slabs (components); similar to electrical resistors in parallel, and $\lambda_{\perp}$ assumes the slabs arranged in a series, similar to electrical resistors in series. These conductivities form the extreme boundaries, much overestimated typically, of the possible effective conductivity of the composite.

The proposed models may be very specific to a given material system. Carson *et al.* [97] pointed out that the term 'porous' may be the cause of confusion and has not been well defined. They tried to differentiate 'internal porosity' from 'external porosity'. Their analysis was limited to steady state conduction heat transfer and materials that could be considered isotropic, macroscopically. Using Fig. 5.3, Carson *et al.* [97] depicted a heat flow in a theoretical material. The material contains circles (the dispersed media) in a continuos phase.

It is apparent from Fig. 5.3 that the optimal heat path depends on the thermal conductivity of the phases, where the heat flow avoids the dispersed phase when $\lambda_{cont.} > \lambda_{disp.}$, while it utilizes the dispersed phase as much as possible otherwise. With this example, they clarified that even if the volume fractions are equivalent, the

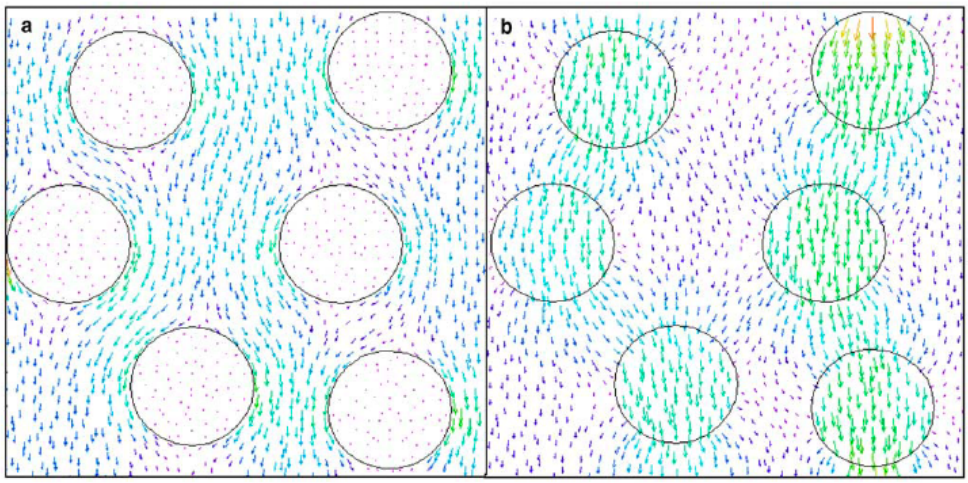

Figure 5.3: Carson *et al.* depicted the heat flux vectors for dispersed spheres in a continuos medium (a) $\lambda_{cont.} > \lambda_{disp.}$ and (b) $\lambda_{cont.} < \lambda_{disp.}$ [97].

effective thermal conductivity can be different. Hence, they defined particulate-type materials in which air comprises a continuos phase as 'external porsosity' material and materials such as foams, sponges, and honeycomb structures as 'internal porosity' material.

Another well-known model for effective thermal conductivity measurement is the Maxwell-Euken model [97, 98] as given in Eqn. 5.5 and 5.6.

$$\lambda_e = \lambda_1 \frac{2\lambda_1 + \lambda_2 - 2(\lambda_1 - \lambda_2)\phi_2}{2\lambda_1 + \lambda_2 + (\lambda_1 - \lambda_2)\phi_2} \tag{5.5}$$

$$\lambda_e = \lambda_2 \frac{2\lambda_2 + \lambda_1 - 2(\lambda_2 - \lambda_1)(1 - \phi_2)}{2\lambda_2 + \lambda_1 + (\lambda_2 - \lambda_1)(1 - \phi_2)} \tag{5.6}$$

In general the Maxwell's model is biased towards the continuos phase. There can be materials where the distinction between continuos and dispersed phase is ambiguous. Either component can be considered continuos or dispersed. Effective medium theory (EMT) has been reported to work well in these scenarios [97], and is

given in Eqn. 5.7.

$$\lambda_e = \frac{1}{4}\left((3\phi_2 - 1)\lambda_2 + [3(1-\phi_2) - 1]\lambda_1 + \sqrt{[(3\phi_2 - 1)\lambda_2 + (3\{1-\phi_2\} - 1)\lambda_1]^2 + 8\lambda_1\lambda_2}\right) \tag{5.7}$$

The EMT model assumes that for a completely random distribution, the local disturbance caused by the inclusions could be averaged such that over a sufficiently large volume, the temperature distribution within the material could be approximated by a material having a uniform temperature distribution with effective thermal conductivity λ_e. Figure 5.4 shows the conductivities predicted by the above mentioned models with varying porosity. The thermal conductivities used to calculate the plot was $\lambda_1 = 10$, and $\lambda_2 = 1$.

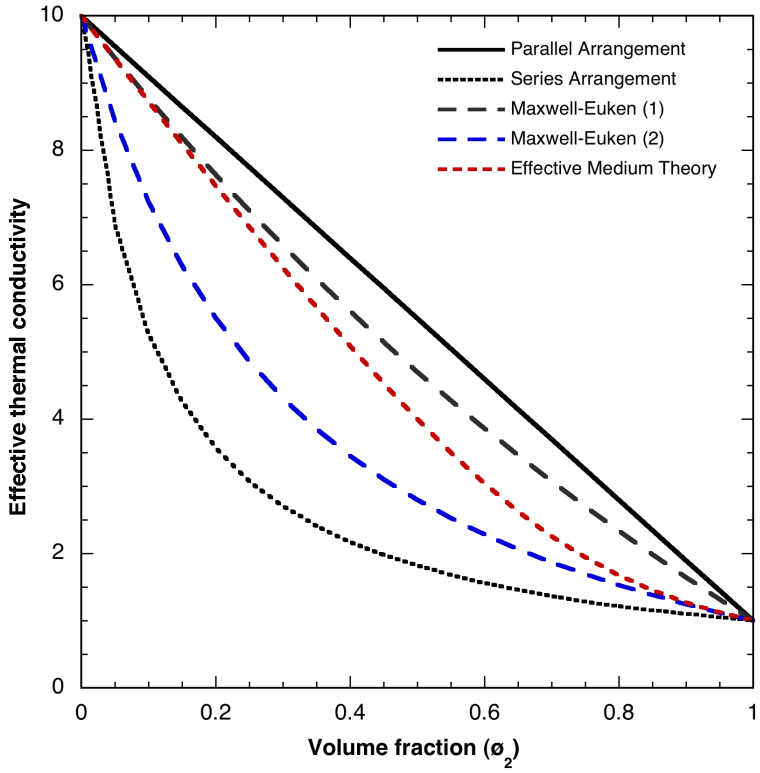

Figure 5.4: The effective thermal conductivity prediction using different models for $\lambda_1/\lambda_2 = 10$.

In Fig. 5.4, Maxwell-Eucken-1 predicts the conductivity for materials where $\lambda_{cont.} > \lambda_{disp.}$ and Maxwell-Eucken-2 predicts for $\lambda_{cont.} < \lambda_{disp.}$. Furthermore, Carson *et al.*

explain that the region between EMT and Maxwell-Eucken-1 would predict conductivities for 'internal porosity' and between EMT and Maxwell-Eucken-2 would predict for 'external porosity' regions. In our material fabrication process, high thermal conductivity phase, crystalline silicon carbide is embedded within either amorphous silicon carbide or other fuel materials. This would classify as an external porosity material.

An effort has been ongoing to fabricate silicon carbide based test specimens at different pyrolysis temperatures (900, 1150, and 1400 °C). Furthermore, by fabricating samples at 1650 °C, silicon carbide specimens ranging from completely amorphous to crystalline nature can be obtained. Table 5.3 is data from an unpublished investigation performed by Arif Rahman at Mechanics of Advanced Materials Laboratory (MAML). A comparison of silicon carbide fabricated using our technique was made with Hexoloy® SA silicon carbide (Saint-Gobain Ceramics, 23 Acheson Drive, NY) sintered specimens.

Property	**Hexoloy® SiC**	**AHPCS derived SiC**		
		900°C	1150°C	1400°C
Biaxial Strength (MPa)	263±76	55±2	80±8	85±5
Density (gm/cc)	3.15	2.43	2.5	2.73
Open Porosity (%)	0.58	2.98	4.08	10.12
Closed Porosity (%)	1.93	4.15	1.84	1.05
Thermal Conductivity (W/m-K)	65.60	2.44	3.86	12.03

Table 5.3: Comparison of different properties of AHPCS derived SiC using PIP technique and Hexoloy® SA SiC, Saint-Gobain Ceramics Structural Ceramics, NY. The experiments were carried out by Arif Rahman at MAML.

The variation in the thermal conductivity after higher pyrolysis temperature is due to the increased crystallinity of the silicon carbide. Our latest effort includes identifying the volume fraction of the crystalline phase using atomic force microscopy (AFM). This is extremely critical and can be used to predict the minimum amount of silicon carbide required to fabricate a fuel composite of desired thermal conductivity.

CHAPTER 6

MECHANICAL CHARACTERIZATION

The strength of ceramic materials depend on the stressed area and the statistical distribution of strength-controlling three dimensional flaws [99]. The test must be designed such that the maximum area is tested to minimize sampling error. Therefore, biaxial flexure test methods are preferred over uniaxial testing (in tension or in bending) for characterization of ceramics [100, 101]. The benefits include the examination of a large surface area that is free from edge finishing defects, ease of test piece preparation, and the applicability of this method to thin sheets. A larger stressed area increases the probability of characterizing the flaw population successfully. In uniaxial tests, failure is governed by the condition of edges parallel to the major axis. This may result in improper judgement of the material strength and behavior. This makes the biaxial stress distribution, where the stress is maximum over a plane, more discriminate of material defects than a uniaxial distribution. In the biaxial flexure test method the maximum tensile stress occurs within the central loading area, far from edges, and spurious edge failures are eliminated [102].

Historically, there were several problems associated with the biaxial methods, which led to the existence of many variants. Table 6.1 lists various biaxial tests that has been studied earlier [103]. Each method has its own benefits and drawbacks. Methods that include the contact with balls, suffer through a stress concentration at the contact locations. In case of loading the disc using a ball, several approximations have been suggested for the calculation of the contact radius at the loading point [99, 103], but the difficulty is still encountered. Similarly, commenting on ball-

(a) Axis-symmetric stress distribution
Ring on ring
Ball on ring
Punch on ring
Ball with flat on ring
Full or part pressurization of ring supported disc
(b) Non axis-symmetric stress distribution
Punch on three balls
Ball on three balls
Ring of balls on ring of balls
Ball with flat on three balls

Table 6.1: Typical biaxial flexure test methods [103].

on-three-ball method, Borger *et al.* add that due to the threefold symmetry in this test, the stress depend on a large number of geometrical and material parameters. This complicates the analytical solution considerably. However, these methods provide the feasibility of testing warped specimens as well, which is not possible with ring supported discs. On the other hand, a ring distributes stresses more evenly compared to a ring of balls and it is an easier test to perform for high temperature characterizations [104]. Additionally, the analytical solution is well established. A standard for typical biaxial tests, ASTM F394-02 [105], has been recently deactivated. However, ring on ring is now the most acceptable form which is now associated with a new standard, ASTM C1499-05 [106].

6.1 Ring-on-ring (RoR) Method

Ring-on-ring (RoR) biaxial tests were carried out in the current investigation. The ring-on-ring (RoR) configuration is one of the biaxial tests that exposes the maximum area under a constant maximum stress. The RoR is an axisymmetric test, where the disc is supported by a ring and loaded from the opposite side by another smaller concentric ring, as shown in Fig. 6.1. This configuration subjects a greater portion of the specimen to an equibiaxial stress state and distributes the applied contact

load over a larger area compared to any other biaxial test methods. The concentric support ring in RoR configuration reduces the likelihood of fixture-induced specimen failure leading to invalid test data.

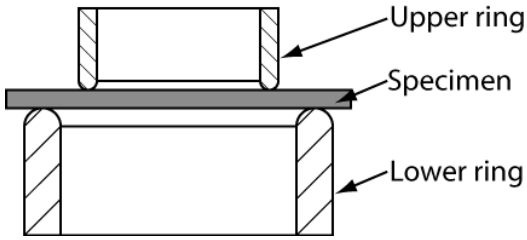

Figure 6.1: Ring-on-ring (RoR), flexure schematic.

Stress magnification is reported under the loading ring in the cases where the deflection of the center of the disc exceeds half the disc thickness. There is an approximate 20% increase in the stress under the loading ring [99, 101]. In general, there is no strict shape requirement for the test sample as long as the outer perimeter is known. Additionally, the shape of the overhang area does not influence the stress distribution considerably within the support ring. However, theories of elastic bending of rigid plates are valid *as long as* the thickness of the disc is less than 0.2 times the diameter of the support ring and the center deflection is less than half of its thickness [99].

6.1.1 Analytical solution

For a ring-on-ring test, the radial (σ_r) and the tangential (σ_t) stresses within the smaller ring are equal and is given by Eqn. 6.1 [99],

$$\sigma_{\mathrm{RoR}} = \frac{3P}{4\pi t^2}\left[\frac{(1-\nu)(a^2-b^2)}{a^2}\frac{a^2}{R^2} + 2(1+\nu)\ln\frac{a}{b}\right] \tag{6.1}$$

where P is the applied load, ν is the Poisson ratio of the specimen and was assumed to be 0.20 for SiC, a is the radius of the support ring, b is the radius of the load ring, and R and t are the radius and thickness of the disc specimen, respectively. A

correction factor, a^2/R^2, is commonly used to accommodate the stiffening effect due to the overhang. The radial (σ_r) and the tangential (σ_t) stresses outside the inner ring, $b \leq r \leq a$, are given by the expressions given below [99]:

$$\sigma_r = \frac{3P}{4\pi t^2}\left[2(1+\nu)\ln\frac{a}{r} + \frac{(1-\nu)b^2(a^2-r^2)}{a^2r^2}\frac{a^2}{R^2}\right] \tag{6.2}$$

$$\sigma_t = \frac{3P}{4\pi t^2}\left[2(1+\nu)\ln\frac{a}{r} - \frac{(1-\nu)b^2(a^2-r^2)}{a^2r^2}\frac{a^2}{R^2} + 2(1-\nu)\frac{a^2}{R^2}\right]. \tag{6.3}$$

It can also be noted that the stresses are independent of the Young's modulus of either the test material or the rings, but rather depend on the Poisson's ratio of the disc. The ring-on-ring method can also be used to measure the Young's modulus of the material using Eqn. 6.4.

$$E = \frac{3P(1-\nu^2)b^2}{2\pi y_c t^3}\left[\frac{a^2}{b^2}\left\{1 + \frac{(1-\nu)(a^2-b^2)}{2(1+\nu)R^2}\right\} - \left\{1 + \ln\frac{a}{b}\right\}\right], \tag{6.4}$$

where y_c is the deflection at the center of the disc. However, in many cases, the deflection at center may not be easily measured. Whereas, the deflection of the loading ring could be measured easily. Therefore, the above equation was modified to incorporate the load ring deflection. The general solution for the deflection of the disc at location r is given by Eqn. 6.5 [107].

$$y_r = y_c + \frac{M_c r^2}{2D(1+\nu)}, \quad 0 \leq r \leq b \tag{6.5}$$

where $M_c = waL_9, w = P/2\pi b, D = \frac{Et^3}{12(1-\nu^2)}$ and $L_9 = \frac{b}{a}\left\{\frac{1+\nu}{2}\ln\frac{a}{b} + \frac{1-\nu}{4}\left[1 - \frac{b^2}{a^2}\right]\right\}$. This can be used to derive the deflection beneath the loading ring as:

$$y_b = y_c - \frac{3P(1-\nu^2)b^2}{2\pi Et^3}\left[\frac{(1-\nu)(a^2-b^2)}{2(1+\nu)a^2} + \ln\frac{a}{b}\right] \tag{6.6}$$

$$y_b = \frac{3P(1-\nu^2)b^2}{2\pi Et^3}\left[\frac{(a^2-b^2)}{b^2}\left\{1 + \frac{(1-\nu)}{2(1+\nu)}\left[\frac{a^2}{R^2} - \frac{b^2}{a^2}\right]\right\} - 2\ln\frac{a}{b}\right]. \tag{6.7}$$

Note that this equation includes the overhang factor which has been previously accounted for, while calculating the deflection at the center. Equation 6.7 can also be modified to calculate the Young's modulus easily if the deflection at the loading ring is the known parameter. The Young's modulus obtained using the biaxial tests may not compare well with the one measured using the uniaxial tests, because of the fundamentally different failure mechanisms at play in these two methods.

Giovan and Sines [108] compared uniaxial and biaxial tests and found that the flexural strengths were about 16% lower in biaxial tests on alumina samples. They also performed high temperature strength measurements at 982 °C. The high temperature measurements are important for structural materials that are expected to be exposed to higher temperatures during the service period. They found that the failure mode was different at higher temperatures and they predicted that the critical flaws at room temperature may not be critical at high temperature and even if they are critical their performance may vary with temperature.

In a similar vein, several other efforts have been made to compare the modulus obtained using the uniaxial and biaxial methods [102,109,110]. Chao and Shetty [109] compared the statistical distribution models and tried to compare the modulus obtained through the experimental tests (three point bend, four point bend, compression and biaxial flexure). Ban *et al.* [102], calculated the modulus with several methods and compared them with the modulus obtained using pulse-echo method.

6.1.2 Ensuring validity of the test

In the case of large central deflections, the stresses under the load ring is much higher than that at the central region. Kao and coworkers [111] studied the effect of large scale deflection, where the deflection at the center could be 3–4.5 times the thickness of the plate. They concluded that in case of large bending, membrane and stretching stresses predominate over bending stresses. Moreover, in case of large deflections the

linear plate theory does not apply for strength calculations.

Care is needed to select the diameters of the loading and support rings, relative to the specimen thickness, in order to promote a valid failure event. Also, clean loading conditions and plane-parallel disk shaped specimens are required for the RoR configuration. Lack of these conditions may result in a 3-point contact between ring and specimen.

If the contact stresses are large, the measured stresses deviate from the theoretical model and the failure is biased at the contact location. Therefore a ring crosssection radius of $t/4$ to $3t/4$, reduces the elevation in the tensile stresses to less than 2% [112]. The concentric rings in the current setup were made up of stainless steel and had bull-nose edges with a radius of 0.3125 mm towards the loading side. This configuration employed a support ring diameter of 19.05 mm and the loading ring diameter of 6.35 mm. The specimens were loaded in the RoR fixture using a table-top test frame

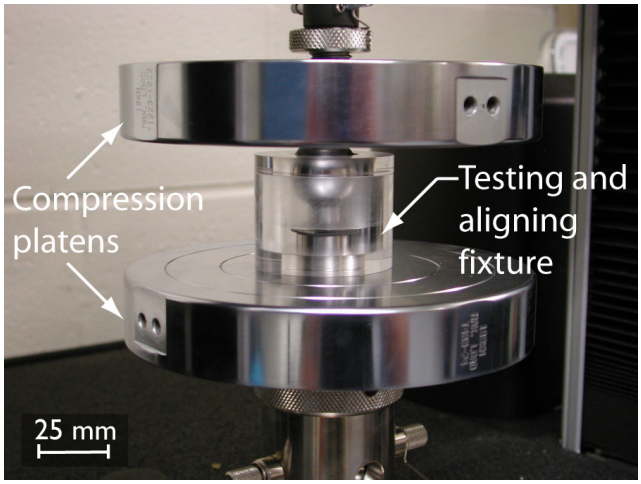

Figure 6.2: Photograph of RoR Fixture.

(Instron® 5567, Instron Corporation, Norwood, Massachusetts, USA) as shown in Fig. 6.2. Adhesive tape was applied as per ASTM C1499-05 [106] on the compressive side of the sample which reduced stress concentration and helped in retaining the disc fragments together after the failure. Displacement controlled loading at a rate of 0.5 mm/min. was used and the load versus load-point displacement was recorded

till the point of failure. Then the flexural strength was calculated from the peak load sustained by the specimen. A minimum of five samples were tested for each material. The flexure strength was then determined as per Eqn. 6.1 [99], using the peak load at failure.

The stress calculated using Eqn. 6.1 is the maximum stress achieved by the sample with $\sigma_{\mathrm{RoR}} = \sigma_r = \sigma_t$. For precise breaking strength determination, the fracture must initiate from the uniformly stressed region (the region within the central ring in RoR). This also defines the validity of the test where the failure must initiate from the central loaded region. The validity of ring-on-ring results was examined by testing commercially obtained alumina discs (AD–90, CoorsTek, Golden, Colorado, USA). Figure 6.3 shows valid/invalid failure patterns for a ring-on-ring test. Figure 6.4

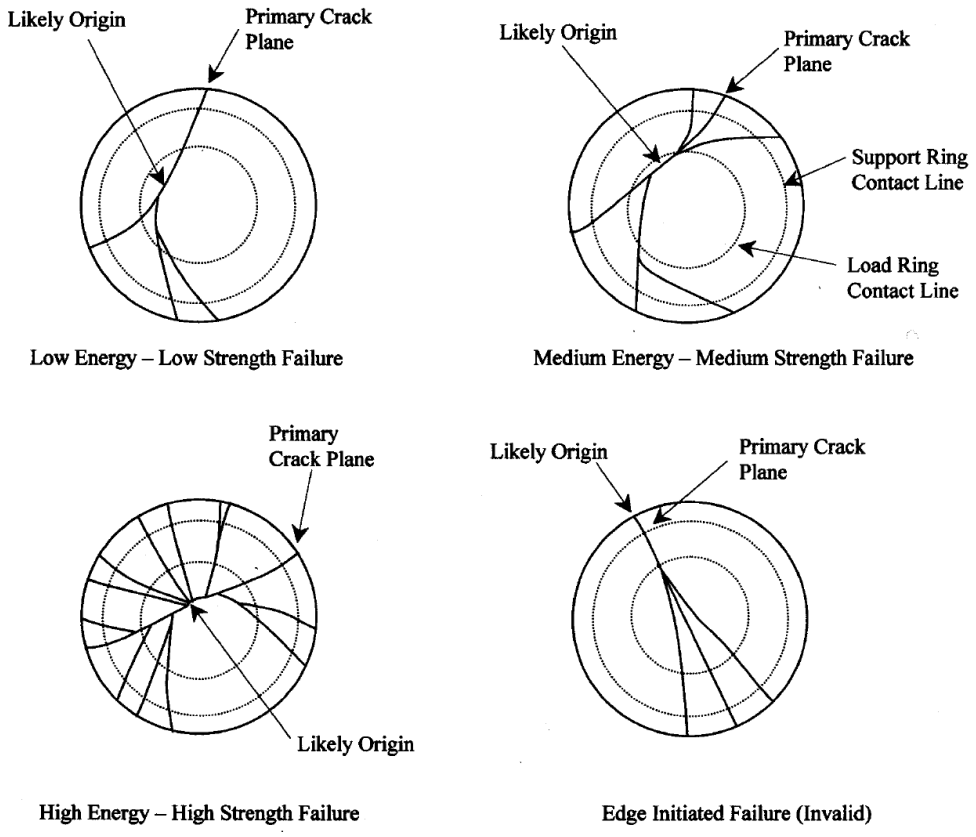

Figure 6.3: Identifying valid failure patterns as per ASTM C1499-05 [106].

illustrates valid tests in which the failure initiates from the central region of the

discs [110].

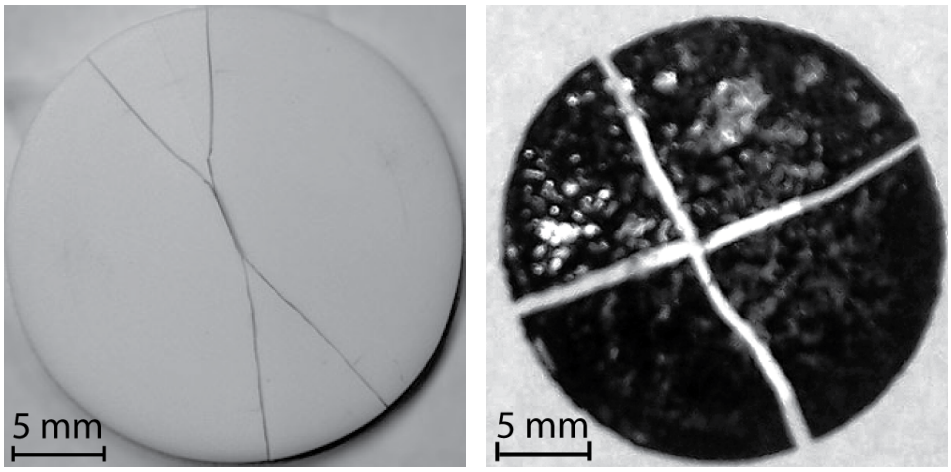

(a) Alumina disc (b) (a-SiC)–U_3O_8–A disc

Figure 6.4: Typical RoR failures.

Uniaxial flexure test and RoR tests were compared by Wereszczak *et al.* [110], on 99.5% pure alumina samples purchased from CoorsTek. They reported that the RoR values were ∼20% less than their uniaxial flexural strength. However, the biaxial strength obtained for alumina (AD–90, 90% purity) in our test was ∼35% lower than the uniaxial strength reported by CoorsTek. However, a valid failure pattern was obtained, as suggested by Wereszczak *et al.* [110], for both alumina and uranium-ceramic samples, as shown in Fig. 6.4. The validity of these tests were also identified by looking at the fracture, which originated from inside the loading ring instead of initiating beneath the ring. The flexural strength results are shown in Table 6.2. Note that the samples named SiC-PP were fabricated using commercially obtained silicon carbide as the initial powder. Figure 6.5 shows the typical loading curve obtained for the RoR biaxial tests done on the prepared discs.

6.1.3 Effect of porosity

Effect of porosity on mechanical strength has been widely studied [113–115]. Porosity affects the material's modulus, fracture toughness and biaxial strengths. Radovic *et*

Material	Biaxial Strength (MPa)	Pyrolysis Temp. (°C)
SiC-900	42±2	900
SiC-PP-9010-H	128±14	1150
SiC-PP-9010-M	118±7	1150
(a-SiC)–U_3O_8–A	54±3	900
(a-SiC)–U_3O_8–B	49±5	900
UO_2-PP-9010-H	55±2	1150
NbC-PP-9010-H	178±16	1150
NbC-PP-9010-M	151±9	1150
NbC-SiC-PP-454510-H	154±17	1150
ZrC-PP-9010-H	117±17	1150
ZrC-PP-9010-M	136±10	1150
ZrC-SiC-PP-454510-H	109±11	1150
ZrC-NbC-PP-454510-H	124±12	1150
UC-PP-H	72±9	900
UH_3-PP-H	72±6	1150
UC-Nb-PP-H	103±6	1150
Alumina	222±17	–

Table 6.2: Biaxial strength of the fabricated ceramic composite and alumina using the RoR test.

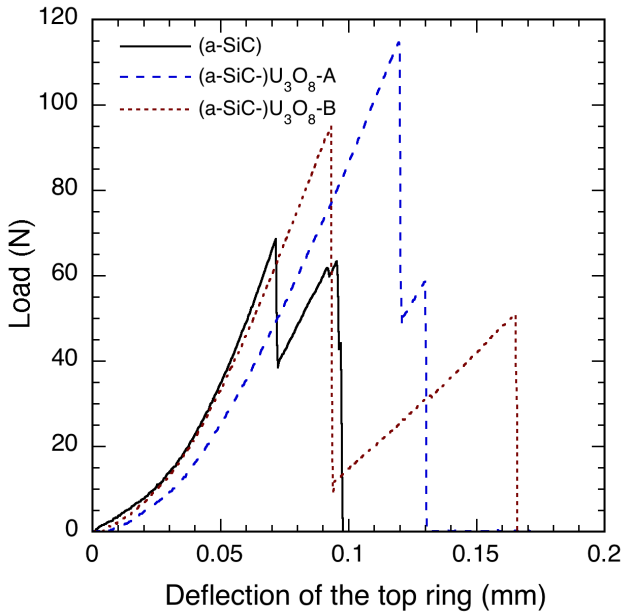

Figure 6.5: Typical load-deflection curve of ceramic composites test under RoR.

al. performed biaxial among the other tests to characterize the effect of porosity. The most widely used property-porosity equation 6.8 uses the typical minimal solid area (MSA) model.

$$\sigma = \sigma_0 exp(-BP') \tag{6.8}$$

where B is a constant, σ_0 is the strength at zero porosity, and P' is the porosity in the material. Equation 6.8 can be used to describe material behavior of a wide variety of materials. This relationship assumes that the strength of the material is uniform in the remaining areas. However, this may not be true for the ceramic materials. Several researchers believe that the strength can be only predicted using statistical failure probabilities [113].

The fracture toughness, $K_{\mathrm{IC}} = \sqrt{2E\gamma}$, and strength, $\sigma_f = K_{\mathrm{IC}}/Y\sqrt{c}$, where γ is the fracture surface energy, Y is the geometrical factor, and c is the critical defect size respectively. Because of the interdependence, it is expected that the property-porosity trend must be similar in all three cases (material's modulus, fracture toughness and biaxial strengths), but Radovic and Lara-curzo predicted that in some conditions, the distribution of critical flaws vary with porosity. If the strength controlling flaws are larger than the pore sizes, the properties follow the above formulation. They predicted that in the case of crack bridging and the interaction of the cracks with the pores, the porosity dependance for the elasticity modulus and the fracture surface energy changes.

Recently, Pabst *et al.* [116] proposed another relationship as,

$$\sigma = \sigma_0(1 - P')(1 - P'/0.684), \tag{6.9}$$

which was found suitable for pore forming materials. The microstructures are different for the partially sintered materials as opposed to those using pore formers. This model was found attractive as the PIP process generates pores during pyrolysis. We can use

this model to calculate the zero porosity biaxial stress for amorphous silicon carbide (σ_0). The porosity, P', for a-SiC can be calculated using the bulk density, ρ_b, and the particle density, ρ_t, provided earlier in Table 4.3. The porosity was calculated as

$$P' = 1 - \frac{\rho_b}{\rho_t}, \tag{6.10}$$

which gives P' as 0.1723 (for $\rho_b = 2.21$ and $\rho_t = 2.67$ g/cm^3). Using the biaxial flexure strength, $\sigma = 42 \pm 2$ MPa (Table 6.2), the zero porosity biaxial strength, σ_0 was obtained to be 68 ± 3 MPa. Similarly, the zero porosity strength for amorphous silicon carbide, prepared by Arif Rahman (reported in Table 5.3) using our technique, was obtained as 66±2 MPa. However, since the biaxial data can not be compared with other reported uniaxial strengths, the applicability of these models for our fabrication technique is yet to be authenticated.

6.1.4 Other applications of RoR

Testing square plates

The ring-on-ring method is not restricted to circular plates. In fact, it is not affected considerably by the shape of the plate. There have been several studies to model the effect of the overhang and calculating the mean radius of the plate [112, 117]. Typically, the R was taken as the average of the edge lengths. However, the square to round plate approximation results in overestimation of the stresses by about 4% [104]. Salem *et al.* [112] provided a better estimate for the disk diameter, D, for the square plates as:

$$D = \frac{l}{0.90961 + 0.12652\frac{t}{a} + 0.00168 \ln \frac{l-a}{t}}, \tag{6.11}$$

where l is the average edge length of the square plate. This estimation reduces the maximum stresses to within 1% of that calculated using the finite element analysis carried out by them.

Testing multi-layered composites

Recently, biaxial modes are being considered for the multilayer testing for composites. Hsueh *et al.* [118] summarized and developed an analytical model for biaxial flexure for multilayerd ceramics. Finite element analysis was also carried out for two and three layered ceramics to validate the closed form solution.

Using biaxial testing methodology would be extremely effective in measuring properties of multilayered composites. This method would be effective even if each layer has different mechanical properties. Owing to this, it can be an effective method to measure the strain to failure measurements in thermal barrier coatings. This technique would be effective because the flaw sizes in very thin layers can be restricted to that of the layer itself and therefore the failure can be controlled [119].

CHAPTER 7

FINITE ELEMENT ANALYSIS OF ROR

7.1 Introduction

Ring-on-ring method is an attractive biaxial test method for ceramic materials because it examines a large surface area for flaws. It is well-suited for high temperature testing as well, due to its structural simplicity. Guidelines for designing a test fixture, for *valid* test results, have been proposed by a few authors [104, 112, 120, 121] using numerical models.

The lack of ductility in ceramics, leads to low strain tolerance, low fracture toughness, and large variations in the failure strength. The failure is governed by the statistical distribution of the strength controlling flaws. Therefore, in year 1993, Powers *et al.* [120] evaluated the reliability of a ceramic component using the finite element analysis (FEA). This was one of the first FEA based study for the ROR test method. They used ceramic analysis and reliability evaluation of structures LIFE prediction program (CARES/LIFE) for the analysis. Herein, the results from ring-on-ring test of silicon carbide were integrated with CARES/LIFE that predicated the survivability of the monolithic component. Thus they were able to predict Weibull parameters (statistical analysis parameters, assuming gaussian distribution of the flaws) for the materials correctly.

In another finite element (FE) based study, Hulm *et al.* [121] modeled ROR for only one configuration ($b = 3t$, $a = 7.5t$, $R = 9t$, and $t = 2$ mm). In their analysis, a uniform circumferential load was applied to form the load ring and a circumferential restriction on Z-displacement for the nodes making support ring. The schematic of

their model is shown in Fig. 7.1. This was a preliminary study which focused on comparing the uniform stresses within the inner ring with the stresses appearing at the specimen edges. They concluded that the edge stresses drop down by about 70% compared to the maximum, which occurs at the center. This reduced stress at the edges would be insufficient for a failure initiation.

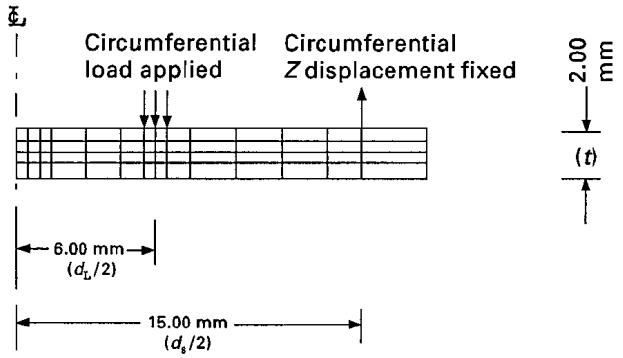

Figure 7.1: Finite element model used by Hulm *et al.* [121]

Later, in year 2002, Powers *et al.* [104] used FE modeling to compare square and circular geometries under ROR loading. Their work established the initial guidelines for the ring-on-ting test method. The finite element model used by Powers *et al.* is shown in Fig. 7.2. They setup the guidelines by comparing the numerical results with linear-plate-bend theoretical solution.

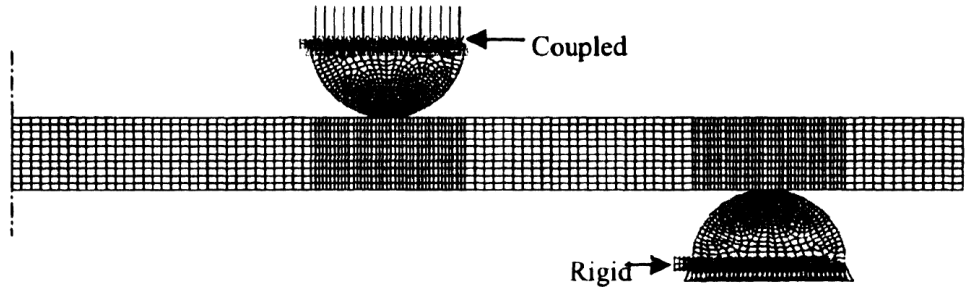

Figure 7.2: Axisymmetric mesh of the plate and ring assembly employed by Powers *et al.* [104]

The disc in their model was assumed to have elastic modulus of 300 GPa and Poisson's ratio of 0.2. The rings had elastic modulus of 200 GPa and Poisson's

ratio of 0.3. Friction condition was also used in their model. A summary of their recommendation is described below:

Maximum center deflection – Deviation from linear plate theory was observed when the deflection at the center, y_c, exceeded 1/4 of t, the disc thickness.

Disc thickness (a/t)– To minimize the failures due to edge effects, the stresses around the overhang must be kept as low as possible. The tangential edge stresses, responsible for overhang stresses, were observed to be lower for the thinner samples (high a/t). On the other hand, the ratio of maximum versus center stress increases with thickness of the disc.

Alignment – Finally, they predicted that a 1% error in concentricity of the ring results in 2% error in the stresses within the support ring. This increases the risk of rupture near the load ring by about 30% for a material with Weibull modulus of 20.

The ring-on-ring based FEM models in literature have assumed uniform disc thickness. The effect of uneven disc thickness has not been modeled yet. Typically, another biaxial method, ball-on-three-ball (Bo3B), is preferred for the tests where non-parallel discs are expected. Ball-on-three-ball can accommodate slight misalignments in the specimen planes. However, there are several limitations including stress concentration at the load and support balls, a small part under maximum stress, and perhaps most importantly the problems associated with contact radius calculation. Borger *et al.* [103,122] investigated the Bo3B tests in great detail using finite element modeling. They modeled several thickness profiles, including non-parallel, convex, and warped discs.

We created a numerical model for ROR in an effort to fill the research gap. The two aspects that were studied in our study are:

1. Variable contact profile (fixed t, b, and a)

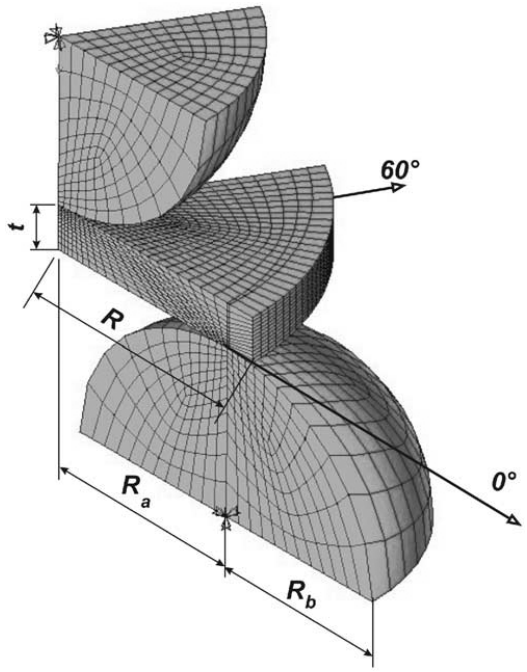

Figure 7.3: The FE model of ball-on-three-ball (Bo3B) setup [122]. It utilizes the six fold symmetry. However, to model a disc with non-parallel top and bottom surfaces, the whole disc requires meshing and symmetry cannot be used.

2. Variable location of the load ring (variable b/a, fixed t)

The long term objective of this effort is to analyze the effect of uneven surfaces while testing discs under ROR.

7.2 Procedure

Abaqus was used for ROR modeling in the current study. Initially, because of its axisymmetric nature and uniform disc thickness assumption, a 2D model was sufficient. Therefore, the disc was modeled as a 2D-deformable, axisymmetric plate with diameter of $21.2t$ where, t is the thickness of the plate. The support rings were modeled as 2D axisymmetric, analytical rigid parts. The support ring diameter was taken as $15.8t$ and load ring diameter as $5.3t$.

The disc consisted of 4 node bilinear axisymmetric quadrilateral elements with reduced integration and hourglass control (CAX4R). Only one point in the center

of the element is used because of the chosen reduced integration. This helps in reducing the stiffness of the response. The contact between the rings and the disc was ensured by providing kinematic contact conditions. Master-slave designation was also associated for smooth contact calculations. The load and the support rings formed the master, and the disc was defined as slave. Furthermore, the number of seed points were doubled around the contact locations as advised by Abaqus. Figure 7.4 shows the generated FE model. It can be seen in Fig. 7.4(a) that the rings do not touch the disc initially. Both rings are brought in contact with the disc later, in a separate step, as shown in Fig. 7.4(b). An increased mesh concentration is used for the contact locations. Figure 7.4(c) displays the mesh intensity beneath the load ring contact area.

To load the disc, a constant displacement boundary condition is being used by displacing the top ring by a specified amount. The current study employs an elastic model. The Young's modulus of 210 GPa and Poisson's ratio of 0.3 is being used for the disc. During the variable profile analysis, the contact surfaces are considered frictionless.

7.2.1 Variable contact profile (VCP)

The shape profile of the load and the support ring was identified as the first variable to study in this study. The profile for each ring was varied between, a circle with radius of $0.275t$, a circle with radius of $0.55t$, and a flat punch with width of $0.55t$ having a fillet radius of $0.05t$ which will be henceforth referred as profiles 'C', 'B' and 'P' respectively. Similarly, the load ring is referred as 'inner ring' and the support ring as 'outer ring'. This generated a total of nine initial conditions. This configuration contained 2464 elements for VCP analysis.

The analysis of the flat punch profile required an additional pressure step in the analysis. A small pressure was applied towards the punch after the rings come in

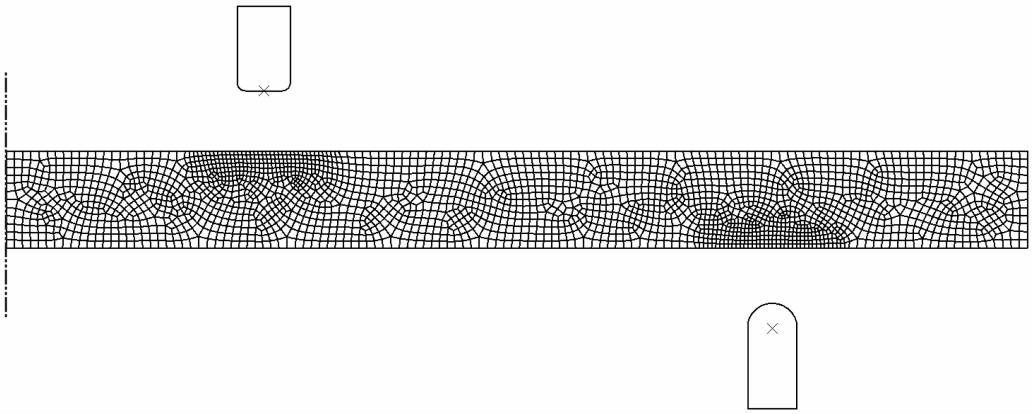

(a) The FE model of RoR used in this study

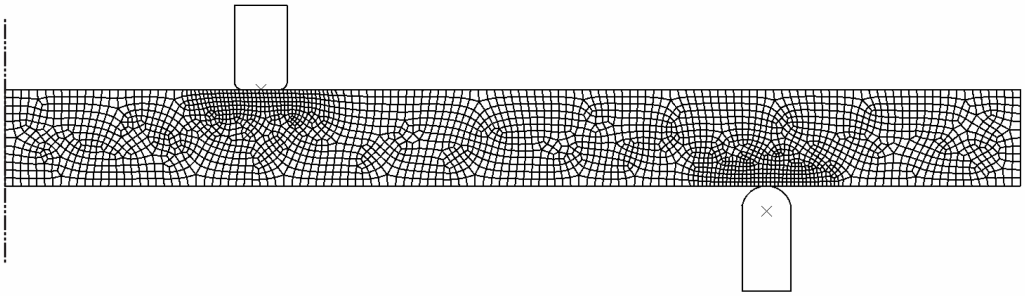

(b) After bringing the rings in contact with the disc

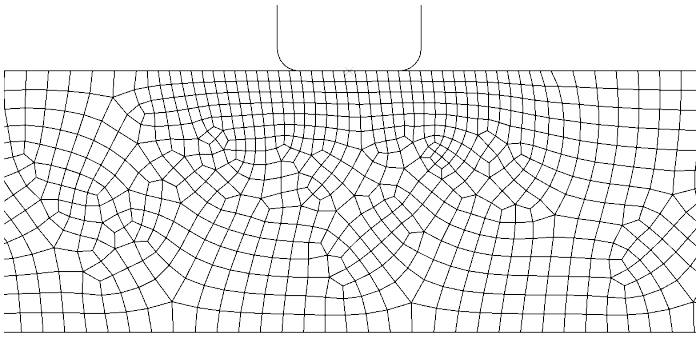

(c) Close up view of the contact area. The meshing was increased to accommodate higher expected strains.

Figure 7.4: The 2D deformable, axisymmetric model for RoR used in the current study.

contact with the disc. Later it is removed gradually while allowing the load ring to compress the disc in the final step. This avoids vibrations that may occur otherwise and helps in convergence of the solution.

For every combination of the rings, the stress variations were studied for five displacements of the load ring: $0.0084t$, $0.0168t$, $0.0252t$, $0.0336t$, and $0.042t$. Figure 7.5 shows the stress contours obtained after the disc is loaded. The configuration used in this examples is IPOC (Inner ring; Punch profile, Outer ring; Circle profile). The stress contours for the radial stress, Fig. 7.5(a), and for the tangential stress, Fig. 7.5(b), are mostly alike within the top ring, however the tangential stress is much more distributed in the region between the two rings. This behavior can be predicted by the linear plate bending theory as well.

Increased stresses are observed at 'A' and 'B' (depicted in Fig. 7.5(a)). At 'A', the stresses are compressive which is of lesser concern than those at 'B' which is tensile. In the current analysis, the overshoot in the tensile stresses at B were less than 2% compared to the stresses in the central region. However, for large deflections even 50% increase in stress on the tensile side beneath the loading ring has been previously reported.

Figure 7.6 shows the summary plot for normalized radial stress with the normalized radial location in the disc. The stress is normalized with the maximum stress observed in the disc (underneath the load ring, compressive in nature), whereas the normal radial location is r/R. The normalized displacement is the ratio of the load ring displacement with the disc thickness. Only two extreme displacement plots have been shown as they displayed similar behavior.

It should be noted that the normalized stress, within the inner load ring, close to unity is much desirable. Therefore, for the inner ring, small circle profiles (see Fig. 7.6(b)) are rejected for future calculations. The peaks around the support ring do not affect the overall stress patterns and are considered non-critical.

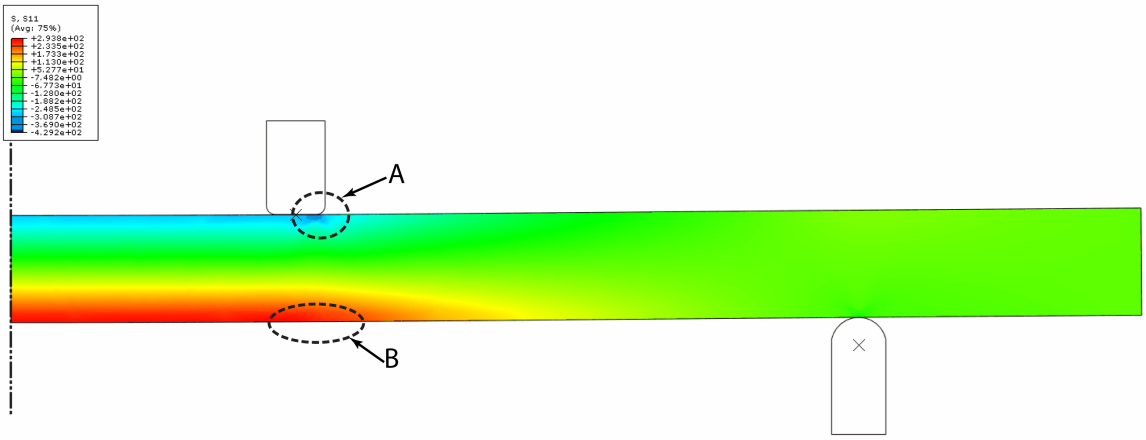

(a) The radial stress contours

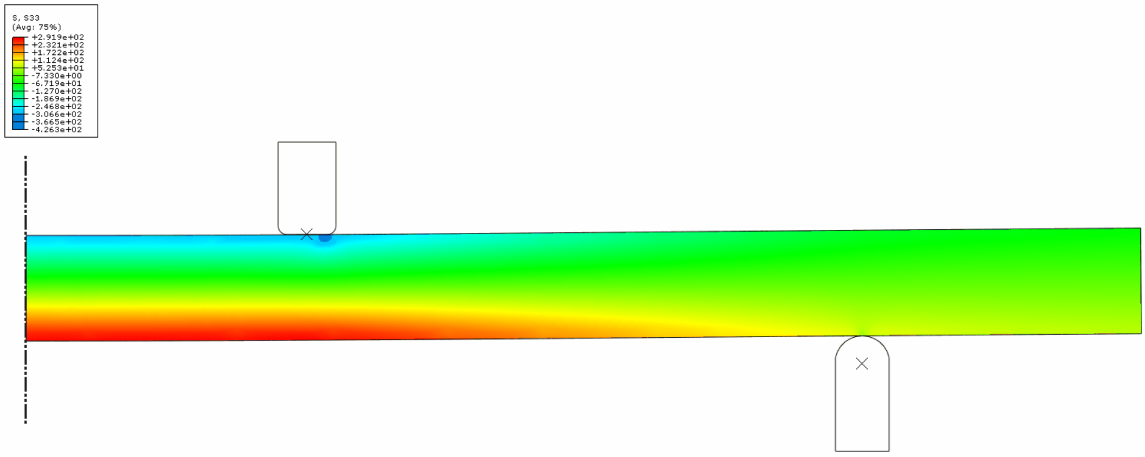

(b) The tangential stress contours

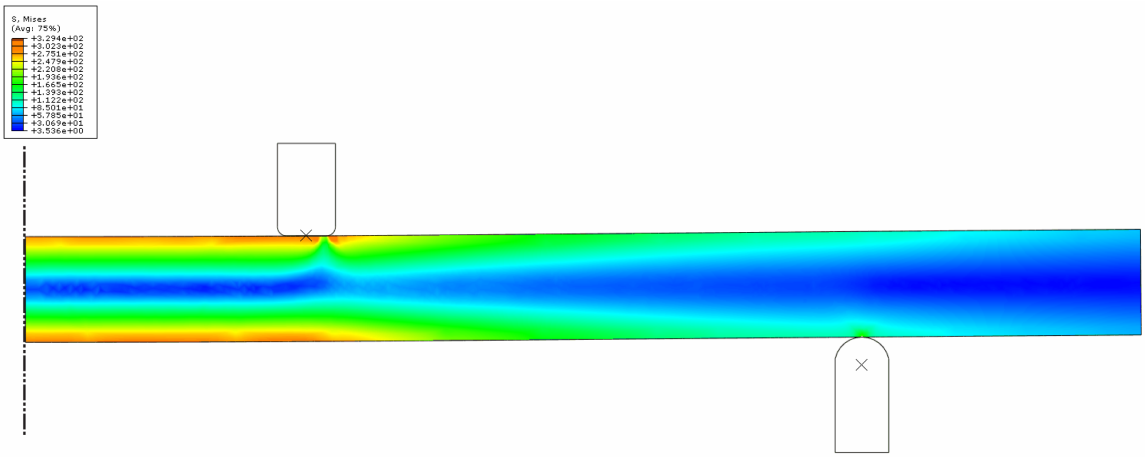

(c) Von-mises stress contour

Figure 7.5: Stress contour plots for a disc under RoR.

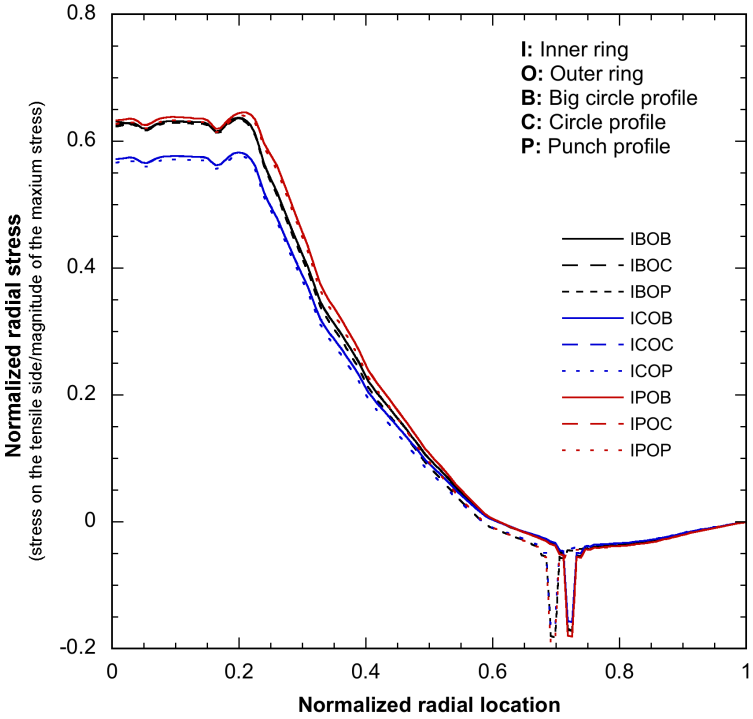

(a) Stress profile for normalized displacement of 0.0084.

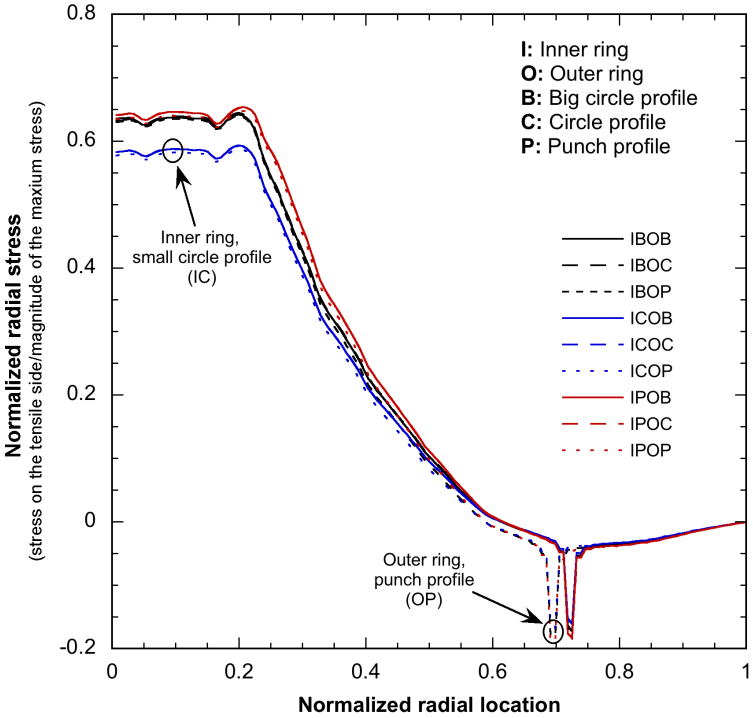

(b) Stress profile for normalized displacement of 0.042.

Figure 7.6: Normalized radial stress profile for two displacements are plotted. The normalized stress ratio closer to unity is favorable during a test.

7.2.2 Variable load ring location

The location of the load ring was varied in an effort to identify its effect on the normalized stress. Six locations were decided for the placement of the load ring. The inner radius of the load ring were $0.0083t$, $1.2t$, $2.3917t$, $3.8667t$, $5.0583t$, and $6.25t$. Due to the modified contact location, mesh was also modified as per requirement. The number of elements used for each condition due to this change were, 2263, 2515, 2484, 2483, 2440, and 2468 respectively. We chose IPOC profile for this study. A constant displacement was provided in each condition.

Figure 7.7 shows the plot of normalized radial stress. It can be clearly seen that

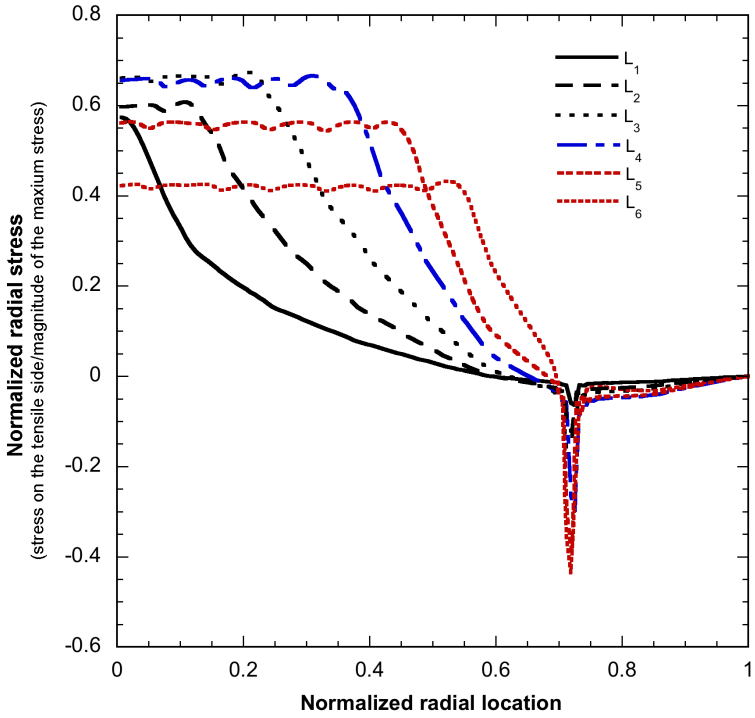

Figure 7.7: Normalized radial stress profile for variable location of the load ring.

the normalized stress within the load ring region increases for the first three cases, reaches a plateau and decreases thereafter. The most desirable location for load ring placement would be at L_4 because it has high normalized stress as well as it examines a larger area compared to L_3 location. This demonstrates that the guideline for the load ring locations can also be predicted using a numerical technique.

CHAPTER 8

CONCLUSIONS & FUTURE WORK

8.1 Conclusions

A novel fabrication technique for processing silicon carbide based ceramic matrix composite using the polymer-derived process was established. The fabrication incorporated a wide variety of powders including commercially obtained crystalline silicon carbide, niobium carbide, zirconium carbide, uranium carbide and uranium oxides (U_3O_8 and UO_2). The fabricated composites can be categorized as oxide-, carbide-, and mixed-metal carbide/silicide materials. The objective was to fabricate solid composite pellets at low process temperatures with silicon carbide in the matrix that could act as the high conductivity phase.

Solid-state reactions were observed in several mixed-metal fabrications. Pyrolysis of UH_3 mixed with niobium or zirconium and AHPCS showed the formation of UC and NbC or ZrC respectively. These results are extremely promising and thus demand further attention. Similarly, niobium and zirconium mixed with AHPCS showed formation of known silicides and interesting unidentified peaks.

The starting material, U_3O_8, during its pyrolysis with AHPCS, was converted to UO_2, as indicated by a color change and confirmed using X-ray diffraction. This conversion is advantageous as U_3O_8 is readily available and UO_2 shows better stability at higher temperatures. In addition, a novel method to fabricate UC based pellets was developed. This involved preparation of UH_3 that acts as a source of uranium metal which finally converts to UC during pyrolysis with AHPCS.

A fairly uniform distribution of uranium particles in the specimens was observed

by scanning electron microscopy. The porosity values were very low and highlight the efficiency of the pressure-assisted vacuum purge method. Even better densification could be obtained using pressure assisted curing of the initially compacted cylinder, as reported by Shah *et al.* [67] for pressure cast SiCN samples.

Given the fact that porosity may be a desirable feature, the achievable strength will be lower than those for near theoretically-dense sintered ceramics. Surprisingly, there is a lack of published data on mechanical strength requirement for fuel pellets aimed towards GFR applications. However, in an annual report prepared by Idaho National Engineering and Environmental Laboratory [19], an arbitrary principal stress limit of 150 MPa was used to compare different fuels. Brittle fracture stress of approximately 1400 MPa, was reported for UO_2 based sintered fuel pellets [84]. However, this may not represent the actual physical requirement for next generation fuel pellets. To understand creep behavior, compressive stress magnitude of 41.4 MPa is typically used in literature for temperatures below 1350 °C [124]. Furthermore, the strength requirement should be studied as a function of irradiation damage, temperature and exposure time. Nonetheless, here we report the biaxial failure strength, determined at room temperature, as a means of comparing the effects of inclusions in the PIP densified SiC matrix. Moreover, Weibull distribution was not studied in the current analysis because the large number of tests required for such analysis. This was not feasible in the current analysis due to a small number of samples fabricated.

Depending on the initial composition and the pyrolysis temperature used, the fabricated composites had varying porosity, different microstructures, and sometimes unknown final compositions. The strength determination was carried out using a biaxial testing technique, which suits the in-service requirements (multi-axial load conditions) of our research material. Several flexure techniques were analyzed before selecting on to the ring-on-ring technique. This technique had an agreeable analytical solution with least assumptions.

The biaxial strength as well as thermal conductivity obtained for carbide-based fabrication were higher than the oxide-based pellets. This is partially due to the fact that the base material used in these composites had higher thermal conductivities. Furthermore, niobium carbide and zirconium carbide inclusions helped in mechanical performance. This indicates that the fillers can provide strengthening mechanisms to the *a*-SiC matrix. The composite fabricated using uranium carbide as the starting material showed a conversion of UC—UO_2 and therefore showed lower mechanical strength and thermal conductivity. This fabrication was not successful in the first attempt because of the large volume change involved ($\approx 30\%$) in this conversion.

This composite fabrication technique holds promise for nuclear fuel preparation. However, since the pyrolysis temperature used in this study was limited to 1500 °C, crystallization of SiC was not achieved. It is generally agreed that *a*-SiC, undergoes swelling under neutron irradiation, which may not be insignificant even at lower temperatures, making it unsuitable for nuclear applications. In a parallel study by Zunjarrao *et al.* [77], it was observed that pyrolysis to 1150–1650 °C produces *β*-crystalline silicon carbide from AHPCS, which would be more suitable for nuclear applications [55, 56, 123]. Allylhydridopolycarbosilane, the precursor used in this study, is known for its ultra high purity and ability to form near-stoichiometric SiC, which are favorable attributes for nuclear applications of SiC. In that manner, the composite prepared in this investigation could be subjected to further thermal treatment to reduce the effects of neutron irradiation.

A numerical model was developed to analyze ring-on-ring tests. The long term objective of this model is to characterize the effect of non-parallel planes during the disc fabrication. Additionally, the statistical inclusion of porosity is also planned for. Nonetheless, it has been used over here to characterize the possible ring profiles that can be used for the ROR test and similarly the preferred location of the load ring can also be predicted. Currently, frictionless contact was studied. This restriction will

also be removed in later studies.

8.2 Future Work

The current work is a part of an ongoing project; while a big leap has been taken towards the fabrication of polymer derived ceramic composites for nuclear applications, there are several areas that requires further probing. A brief description is given below:

Reaction kinetics: Understanding the reaction kinetics must still be pursued intensively. Due to the scarcity of ternary/quarternary phase diagrams for a combinations of U/Nb/Zr/C/Si/H/O, there is a rather slow progress in this field.

Thermal conductivity models: It would be worth to identify the thermal conductivity model that can predict the amount of silicon carbide required to prepare a composite with desired thermal conductivity. This would depend on the knowledge of the degree of crystallinity and its volume fraction, as a function of pyrolysis temperature and hold time.

Numerical modeling: The Abaqus model must be used to model non-parallel discs, so that any error in sample preparation can be studied using the numerical models.

Strength variation with porosity: In the current processing, the samples go through a series of infiltration and pyrolysis cycles, therefore a study could be conducted to analyze the strength variation as the porosity changes (can be varied by the number of infiltrations). The pyrolysis temperature must be kept constant for this study. This study would assume that the properties of the matrix does not change after multiple heat cycles.

Other polymer chemistries: With the increased attention towards SiC fabrication technique, studies related to emerging polymers for producing SiC has also increased [126, 127]. Very recently, Liu *et. al.* [126] reported a novel synthesis of a new SiC precursor, A-PMS (Polymethylsilane). In their study they compared the performance of SiC derived using AHPCS and that of A-PMS. They used PIP for their study and concluded that the fabricated precursor can be used to accelerate the densification process. A-PMS based densification took 4 reinfiltrations compared to 12 involved for AHPCS. However, the Si/C ratio obtained from A-PMS was found to be 1.12 whereas PCS or PMS are known for resulting in stoichiometric SiC. Pyrolysis of allylhydridopolycarbosilane results in little extra carbon [61]. Currently, this is hypothesized as a favorable feature to promote solid state reactions with filler compounds. However, A-PMS may be considered for later use, since the excess carbon could react with initial filler particles and may finally result in inert SiC matrix with enhanced properties.

Ethynylhydridopolycarbosilane (EHPCS) is another polymer, which is developed by Fang *et al.* [127]. They claimed to produce stoichiometric SiC at about 1600 °C which shows characteristics of β-SiC. Further, they achieved C:Si ratio of 1.05 at 900 °C and 1.55 between temperatures of 1200 to 1600 °C.

BIBLIOGRAPHY

[1] Jones, R. H., and Henager Jr., C. H., 2005. "Subcritical crack growth processes in SiC/SiC ceramic matrix composites". *Journal of the European Ceramic Society,* **25**(10 SPEC ISS), pp. 1717 – 1722.

[2] Hinoki, T., and Kohyama, A., 2005. "Current status of SiC/SiC composites for nuclear applications". *Annales de Chimie: Science des Materiaux,* **30**(6), pp. 659–671.

[3] Alkan, Z., Kugeler, K., Kaulbarsch, R., and Manter, C., 2001. "Silicon Carbide Encapsulated Fuel Pellets for Light Water Reactors". *Progress in Nuclear Energy,* **38**(3-4), pp. 411 – 414.

[4] Lee, Y., Lee, S., Kim, H., Joung, C., and Degueldre, C., 2003. "Study on the mechanical properties and thermal conductivity of silicon carbide-, zirconia- and magnesia aluminate-based simulated inert matrix nuclear fuel materials after cyclic thermal shock". *Journal of Nuclear Materials,* **319**, pp. 15 – 23.

[5] Arunachalam, V. S., and Fleischer, E. L., 2008. "Preface". In *Harnessing Materials for Energy.* MRS Bulletin, p. 261.

[6] Arunachalam, V. S., and Fleischer, E. L., 2008. "**The Global Energy Landscape and Materials Innovation**". In *Harnessing Materials For Energy.* MRS Bulletin, pp. 264–276.

[7] International Atomic Energy Agency, 2006. "Annual Report for 2006".

[8] Baldev, R., Vijayalakshmi, M., Rao, V. P. R., and Rao, S. K. B., 2008. "Challenges in Materials Research for Sustainable Nuclear Energy". *Harnessing Materials for Energy - MRS Bulletin,* **33**(4), pp. 327–340.

[9] Sheppard, L. M., 2008. "Is Nuclear Power the Answer to U.S. Energy Needs?". In *American Ceramic Society Bulletin*. pp. 20–24.

[10] Walters, L., Porter, D., and Crawford, D., 2002. "Nuclear fuel considerations for the 21¡sup¿st¡/sup¿ century". *Progress in Nuclear Energy,* **40**(3-4 SPEC), pp. 513 – 521.

[11] DOE, 2002. *A Technology Roadmap for Generation IV Nuclear Energy Systems*. U.S. DOE Nuclear Energy Research Advisory Committee.

[12] Gueneau, C., Chatain, S., Gosse, S., Rado, C., Rapaud, O., Lechelle, J., Dumas, J. C., and Chatillon, C., 2005. "A thermodynamic approach for advanced fuels of gas-cooled reactors". *Journal of Nuclear Materials,* **344**(1-3), pp. 191 – 197.

[13] Corwin, W., Snead, L. L., Zinkle, S., Nanstad, R., Rowcliffe, A., Mansur, L., Swinderman, R., Ren, W., Wilson, D., McGreevy, T., Rittenhouse, P., Klett, J., Allen, T., Gan, J., and Weaver, K., 2004. "The Gas Fast Reactor (GFR) Survey of materials experience and R&D needs to assess viability". *Generation IV: Nuclear Energy Systems,* **ORNL/TM-2004/99**.

[14] Clougher, V. E., Pober, R. L., and Kaufman, L., 1968. "Synthesis of oxidation resistant metal diboride composites". *Transactions of the Metallurgical Society of AIME,* **242**(6), pp. 1077–&.

[15] Perry, A. J., 1987. "The refractories HfC and HfN - A survey. 1. Basic properties". *Powder Metallurgical International,* **19**(1), pp. 29–35.

[16] Opeka, M. M., Talmy, I. G., Wuchina, E. J., Zaykoski, J. A., and Causey, S., 1999. "Mechanical, thermal, and oxidation properties of refractory hafnium and zirconium compounds". *Journal of the European Ceramic Society,* **19**(13-14), pp. 2405–2414.

[17] Bull, J. D., Rasky, D. J., and Karika, J. C., 1992. "Stability characterization of diboride composites under high velocity atmospheric flight conditions". *International SAMPE Electronics Conference,* **24**, pp. 1092 – 1106.

[18] Riedel, R., Mera, G., Hauser, R., and Klonczynski, A., 2006. "Silicon-based polymer-derived ceramics: Synthesis properties and applications - A review". *Journal of the Ceramic Society of Japan,* **114**(1330), pp. 425–444.

[19] Weaver, K. D., Totemeier, T. C., Clark, D. E., Feldman, E. E., Hoffman, E. A., Vilim, R. B., Wei, T. Y. C., Gan, J., Meyer, M. K., Gale, W. F., Driscoll, M. J., Golay, M., Apostolakis, G., and Czerwinski, K., 2004. "Gas-Cooled Fast Reactor (GFR) FY04 Annual Report". *Generation IV: Nuclear Energy Systems,* **INEEL/EXT-04-02361**.

[20] Ion, S. E., Watson, R. H., and Loch, E. P., 1989. "Fabrication of nuclear fuel". *Nuclear Energy,* **28**(1), pp. 21 – 28.

[21] Stoops, R., and Hamme, J., 1964. "Phase relations in the system uranium carbon oxygen". *Journal of the American Ceramic Society,* **47**(2), pp. 59–62.

[22] Cordfunke, E. H. P., 1969. "The Chemistry of Uranium".

[23] Manning, P. S., 1986. "Nuclear fuel manufacture by BNFL". *Nuclear Engineer: Journal of the Institution of Nuclear Engineers*(5), pp. 148 – 151.

[24] Vaidya, V. N., 2008. "Status of sol-gel process for nuclear fuels". *Journal of Sol-Gel Science and Technology,* **46**(3), pp. 369–381.

[25] Rozhgar, O., 2004. "Steady state and transient analysis of heat conduction in nuclear fuel elements". PhD thesis, KTH, Stockholm, Sweden.

[26] Holden, R. B., 1966. "Ceramic Fuel Elements". *Gordon and Breach Science Publishers, New York.*

[27] Kittel, H., Adamson, M. G., Bauer, A. A., Kerrish, J. F., Nayak, U. P., Peterson, D. T., and Weber, E. T., 1977. "Properties of Fuels for Alternate Breeder Fuel Cycle". *ANL-AFP-38, Argonne National Laboratory.*

[28] Ma, B. M., 1983. "Nuclear Reactor Materials and Applications". *Van Nostrand Reinhold Company, New York.*

[29] Oggianu, S. M., No, H. C., and Kazimi, M. S., 2003. "Analysis of burnup and economic potential of alternative fuel materials in thermal reactors". *Nuclear Technology,* **143**(3), SEP, pp. 256–269.

[30] McCoy, K., and Mays, C., 2008. "Enhanced thermal conductivity oxide nuclear fuels by co-sintering with BeO: II. Fuel performance and neutronics". *Journal of Nuclear Materials,* **375**(2), pp. 157–167.

[31] Mccoy, J. K., 2008. "Process for manufacturing enhanced thermal conductivity oxide nuclear fuel and the neclear fuel".

[32] Sarma, K. H., Fourcade, J., Lee, S., and Solomon, A., 2006. "New processing methods to produce silicon carbide and beryllium oxide inert matrix and enhanced thermal conductivity oxide fuels". *Journal of Nuclear Materials,* **352**(1-3), pp. 324–333.

[33] Kuchibhotla, H., 2005. "Enhanced thermal conductivity oxide fuels: compatibility and novel fabrication techniques using BeO". PhD thesis, Purdue University.

[34] Lippmann, W., Knorr, J., Noring, R., and Umbreit, M., 2001. "Investigation of the use of ceramic materials in innovative light water reactor - fuel rod concepts". *Nuclear Engineering and Design,* **205**(1-2), pp. 13–22.

[35] Verrall, R. A., Vlajic, M. D., and Krstic, V. D., 1999. "Silicon carbide as an inert-matrix for a thermal reactor fuel". *Journal of Nuclear Materials,* **274**(1-2), pp. 54–60.

[36] Hough, A., and Marples, J. A. C., 1965. "Pseudo binary phase diagrams of PuO_2 with alumina beryllia and magnesia and pseudo ternary PuO_2-ThO_2-BeO". *Journal of Nuclear Materials,* **15**(4), p. 298.

[37] Solomon, A. A., Revankar, S., and K, M. J., 2005. "Final Report: Enhanced Thermal Conductivity Oxide Fuels". *DOE Project 02-180.*

[38] Ishimoto, S., Hirai, M., Ito, K., and Korei, Y., 1996. "Thermal conductivity of UO_2-BeO pellet". *Journal of Nuclear Science and Technology,* **33**(2), pp. 134–140.

[39] Matthews, R. B., and Herbst, R. J., 1983. "Uranium-Plutonium carbide fuel for fast breeder reactors". *Nuclear Technology,* **63**(1).

[40] Carter, T. C., Knight, T. W., and Anghaie, S., 2003. "Feasibility of mixed carbide fuels for use in transmutation systems". pp. 124 – 127.

[41] Krishnaiah, M., Seenivasan, G., Srirama Murti, P., and Mathews, C., 2003. "Thermal conductivity of selected cermet materials". *Journal of Alloys and Compounds,* **353**(1-2), pp. 315 – 321.

[42] Matthews, R. B., 1992. "Ceramic fuel development for space reactors". *American Seramic Society Bulletin,* **71**(1), JAN, pp. 96–101.

[43] Knight, T., and Anghaie, S., 1999. "(U, Zr, Nb)C pseudo-ternary carbide fuel for high temperature space nuclear reactors". pp. 201 – 213.

[44] Tosdale, P. J., 1967. "IS-T-219". PhD thesis, Iowa State University.

[45] Naghedolfeizi, M., Chung, J.-S., Morris, R., Ice, G., Yun, W., Cai, Z., and Lai, B., 2003. "X-ray fluorescence microtomography study of trace elements in a SiC nuclear fuel shell". *Journal of Nuclear Materials,* **312**(2-3), pp. 146 – 155.

[46] Andrievskii, R. A., Klimenko, V. V., Mitrofanov, V. I., and Poltoratskii, N. I., 1977. "Effect of structural vacancies in interstitial phases on their sintering shrinkage". *Soviet Powder Metallurgy and Metal Ceramics (English translation of Poroshkovaya Metallurgiya),* **16**(6), pp. 423 – 426.

[47] Knight, T. W., and Anghaie, S., 2002. "Processing and fabrication of mixed uranium/refractory metal carbide fuels with liquid-phase sintering". *Journal of Nuclear Materials,* **306**(1), pp. 54–60.

[48] Czechowicz, D. G., G, H. F., and E, S. K., 1991. "High-temperature mixed carbide fuels for space propulsion reactors". pp. 1059–1063.

[49] Butt, P. D., Storms, E., and Wallace, T., 1993. "Knowledge Status Report on Mixed Uranium/Refractory Metal Carbides Useful for Nuclear Thermal Propulsion".

[50] Perez, F., and Ghoniem, N. M., 1993. "Chemical compatibility of SiC composite structures with fusion-reactor helium coolant at high-temperatures". *Fusion Engineering and Design,* **22**(4), pp. 415–426.

[51] Raffray, A. R., El-Guebaly, L., Sze, D. K., Billone, M., Sviatoslavsky, I., Mogahed, E., Najmabadi, F., Tillack, M. S., and Wang, X., 1999. "SiC/SiC com-

posite for an advanced fusion power plant blanket". *Proceedings - Symposium on Fusion Engineering*, pp. 73 – 76.

[52] Snead, L. L., Osborne, M., and More, K. L., 1995. "Effects of radiation on SiC-based Nicalon fibers". *Journal of materials research,* **10**(3), pp. 736–747.

[53] Senor, D. J., Youngblood, G. E., Brimhall, J. L., Trimble, D. J., Newsome, G., and Woods, J., 1996. "Dimensional stability and strength of neutron-irradiated SiC-based fibers". *Fusion Technology,* **30**(3), pp. 956–968.

[54] Hollenberg, G. W., Henager, C. H., Youngblood, G. E., Trimble, D. J., Simonson, S. A., Newsome, G. A., and Lewis, E., 1995. "The effect of irradiation on the stability and properties of monolithic silicon-carbide and SiC_f/SiC composites up to 25 dpa". *Journal of Nuclear Materials,* **219**, pp. 70–86.

[55] Snead, L. L., Katoh, Y., Kohyama, A., Bailey, J., Vaughn, N., and Lowden, R., 2000. "Evaluation of neutron irradiated near-stoichiometric silicon carbide fiber composites". *Journal of Nuclear Materials,* **283**, pp. 551–555.

[56] Newsome, G., Snead, L., Hinoki, T., Katoh, Y., and Peters, D., 2007. "Evaluation of neutron irradiated silicon carbide and silicon carbide composites". *Journal of Nuclear Materials,* **371**(1-3), pp. 76–89.

[57] Katoh, Y., Snead, L. L., Henager, C. H., Hasegawa, A., Kohyama, A., Riccardi, B., and Hegeman, H., 2007. "Current status and critical issues for development of SiC composites for fusion applications". *Journal of Nuclear Materials,* **367**, pp. 659–671.

[58] Kim, B., Choi, Y., Lee, J., Lee, Y., Sohn, D., and Kim, G., 2000. "Multi-layer coating of silicon carbide and pyrolytic carbon on UO¡sub¿2¡/sub¿ pellets by a combustion reaction". *Journal of Nuclear Materials,* **281**(2-3), pp. 163 – 170.

[59] Schick, H. L., 1966. "Thermodynamics of Certain Refractory Comounds". *Academic Press,* **1**, pp. 1–402.

[60] Munro, R., 1997. "Material properties of a sintered alpha-SiC". *Journal of Physical and Chemical Reference Data,* **26**(5), pp. 1195–1203.

[61] Moraes, Kevin, V., and Interrante, Leonard, V., 2003. "Processing, fracture toughness, and vickers hardness of allylhydridopolycarbosilane-derived silicon carbide". *Journal of the American Ceramic Society,* **86**(2), pp. 342–346.

[62] Clark, T. J., Arons, R. M., Stamatoff, J. B., and Rabe, J., 1985. "Thermal degradation of Nicalon SiC fibers". *Ceramic Engineering and Science Proceedings,* **6**, pp. 576–588.

[63] Interrante, L. V., Whitmarsh, C., Sherwood, W., Wu, H.-J., Lewis, R., and Maciel, G., 1994. "High yield polycarbosilane precursors to stoichiometric SiC. Synthesis, pyrolysis and application". *Proceedings of the 1994 MRS Spring Meeting, Apr 4-8 1994, San Francisco, CA, USA,* **346**, pp. 593–603.

[64] Interrante, L., Jacobs, J., Sherwood, W., and Whitmarsh, C., 1997. "Fabrication and properties of fiber- and particulate-reinforced SiC matrix composites obtained with (A)HPCS as the matrix source". *Key Engineering Materials,* **127-131**(Pt 1), pp. 271–278.

[65] Greil, P., 2000. "Polymer derived engineering ceramics". *Advanced Engineering Materials,* **2**(6), pp. 339–348.

[66] Colombo, P., 2008. "Engineering porosity in polymer-derived ceramics". *Journal of the European Ceramic Society,* **28**(7), pp. 1389 – 1395.

[67] Shah, S., and Raj, R., 2002. "Mechanical properties of a fully dense polymer derived ceramic made by a novel pressure casting process". *Acta Materialia,* **50**(16), pp. 4093–4103.

[68] Bharadwaj, L., Fan, Y., Zhang, L., Jiang, D., and An, L., 2004. "Oxidation Behavior of a Fully Dense Polymer-Derived Amorphous Silicon Carbonitride Ceramic". *Journal of the American Ceramic Society,* **87**(3), pp. 483 – 486.

[69] Lewinsohn, C. A., Jones, R. H., Colombo, P., and Riccardi, B., 2002. "Silicon carbide-based materials for joining silicon carbide composites for fusion energy applications". *Journal of Nuclear Materials,* **307-311**(2 SUPPL), pp. 1232–1236.

[70] Kotani, M., Inoue, T., Kohyama, A., Katoh, Y., and Okamura, K., 2003. "Effect of SiC particle dispersion on microstructure and mechanical properties of polymer-derived SiC/SiC composite". *Materials Science and Engineering A,* **357**(1-2), pp. 376 – 385.

[71] Ozcivici, E., and Singh, R. P., 2005. "Fabrication and characterization of ceramic foams based on silicon carbide matrix and hollow alumino-silicate spheres". *Journal of the American Ceramic Society,* **88**(12), pp. 3338–3345.

[72] Singh, A. K., Zunjarrao, S. C., and Singh, R. P., 2006. "Silicon Carbide and Uranium Oxide based Composite Fuel Preparation using Polymer Infiltration and Pyrolysis". *Proceedings of ICONE-14.*

[73] Singh, A. K., and Singh, R. P., 2007. "Fabrication of NbC, ZrC and UC based Silicon Carbide Matrix Composites for Nuclear Applications Using Polymer Infiltration and Pyrolysis". *Material Science & Technology 2007 Conference and Exhibition.*

[74] Guron, M. M., Kim, M. J., and Sneddon, L. G., 2008. "A simple polymeric precursor strategy for the syntheses of complex zirconium and hafnium-based ultra high-temperature silicon-carbide composite ceramics". *Journal of the American Ceramic Society,* **91**(5), pp. 1412 – 1415.

[75] Riedel, R., Mera, G., Hauser, R., and Klonczynski, A., 2006. "Silicon-based polymer-derived ceramics: Synthesis properties and applications-A review". *Nippon Seramikkusu Kyokai Gakujutsu Ronbunshi/Journal of the Ceramic Society of Japan,* **114**(1330), pp. 425 – 444.

[76] Starfire Inc. "Starfire SMP–10 datasheet".

[77] Zunjarrao, S. C., Singh, A. K., and Singh, R. P., 2006. "Structure-Property Relationships in Polymer Derived Amorphous/Nano-crystalline Silicon Carbide for Nuclear Applications". *Proceedings of ICONE-14.*

[78] Pellaud, B., 1971. *The physics design of the gas cooled fast breeder reactor demonstration plant*, Vol. GA-10509. Gulf General Atomic Co., San Diego, CA.

[79] Solomon, Alvin, A., Fourcade, J., Lee, S.-G., Kuchibhotla, S., Revankar, S., Latta, R., Holman, Peter, L., and McCoy, J. K., 2004. "The polymer impregnation and pyrolysis method for producing enhanced conductivity LWR fuels". *Proceedings of the 2004 International Meeting on LWR Fuel Performance, Orlando, Florida, September 19-22, 2004, American Nuclear Society, La Grange Park, IL 60526, United States, pp. 146155. Paper 1028.*, pp. 146–155.

[80] Zunjarrao, S. C., Singh, A. K., and Singh, R. P., 2007. "Modulus and Hardness of Nanocrystalline Silicon Carbide as Functions of Grain Size". *31st International Cocoa Beach Conference and Exposition.*

[81] Kovacheva, P., Todorovsky, D., Radev, D., Mavrudiev, V., Petrov, R., Kovacheva, D., and Petrov, K., 2004. "Mechanochemical effects in U_3O_8". *Journal of Radioanalytical and Nuclear Chemistry,* **262**(3), pp. 573–578.

[82] Pijolat, M., Brun, C., Valdivieso, F., and Soustelle, M., 1997. "Reduction of uranium oxide U_3O_8 to UO_2 by hydrogen". *Solid State Ionics,* **101**, pp. 931–935.

[83] Yang, J. H., Rhee, Y. W., Kang, K. W., Kim, K. S., Song, K. W., and Lee, S. J., 2007. "Formation of columnar and equiaxed grains by the reduction of U_3O_8 pellets to $UO_{(2+x)}$". *Journal of Nuclear Materials,* **360**(2), pp. 208–213.

[84] Orlander, D., 1976. "Pore migration and fuel restructuring kinetics". In *Fundamental Aspects of Nuclear Reactor Fuel Elements*. US Dept of Energy.

[85] Akiyoshi, M., Takagi, I., Yano, T., Akasaka, N., and Tachi, Y., 2006. "Thermal conductivity of ceramics during irradiation". *Fusion Engineering and Design,* **81 A**(1-4), pp. 321 – 325.

[86] James, Filla, B., 1997. "Steady-state high-temperature apparatus for measuring thermal conductivity of ceramics". *Review of Scientific Instruments,* **68**(7), pp. 2822 – 2829.

[87] Huang, B., Ni, Z., Millward, A., McGaughey, A., Uher, C., Kaviany, M., and Yaghi, O., 2007. "Thermal conductivity of a metal-organic framework (MOF-5): Part II. Measurement". *International Journal of Heat and Mass Transfer,* **50**(3-4), pp. 405–411.

[88] Choi, S., and Kim, D., 2007. "Measurement of thermal properties of microfluidic samples using laser point heating thermometry". *Thermochimica Acta,* **455**(1-2), pp. 11–15.

[89] ASTM, C 1113-99(2004). "Standard Test Method for Thermal Conductivity of Refractories by Hot Wire (Platinum Resistance Thermometer Technique)". In *ASTM International*.

[90] Choi, T., Poulikakos, D., Tharian, J., and Sennhauser, U., 2006. "Measurement of the thermal conductivity of individual carbon nanotubes by the four-point three-omega method". *Nano Letters,* **6**(8), pp. 1589–1593.

[91] Mun, J., Kim, S., Kato, R., Hatta, I., Lee, S., and Kang, K., 2007. "Measurement of the thermal conductivity of TiO2 thin films by using the thermoreflectance method". *Thermochimica Acta,* **455**(1-2), pp. 55–59.

[92] Blumm, J., Lindemann, A., and Min, S., 2007. "Thermal characterization of liquids and pastes using the flash technique". *Thermochimica Acta,* **455**(1-2), pp. 26–29.

[93] Kobatake, H., Fukuyama, H., Minato, I., Tsukada, T., and Awaji, S., 2007. "Noncontact measurement of thermal conductivity of liquid silicon in a static magnetic field". *Applied Physics Letters,* **90**(9), p. 094102.

[94] Lee, W., Han, I., Yu, J., Kim, S., and Byun, K., 2007. "Thermal characterization of thermally conductive underfill for a flip-chip package using novel temperature sensing technique". *Thermochimica Acta,* **455**(1-2), pp. 148–155.

[95] ASTM, E1225-04. "Standard Test Method for Thermal Conductivity of Solids by Means of the Guarded-Comparative-Longitudinal Heat Flow Technique". In *ASTM International*.

[96] Cernuschi, F., Ahmaniemi, S., Vuoristo, P., and Mantyla, T., 2004. "Modelling of thermal conductivity of porous materials: Application to thick thermal barrier coatings". *Journal of the European Ceramic Society,* **24**(9), pp. 2657 – 2667.

[97] Carson, J. K., Lovatt, S. J., Tanner, D. J., and Cleland, A. C., 2005. "Thermal conductivity bounds for isotropic, porous materials". *International Journal of Heat and Mass Transfer,* **48**(11), pp. 2150 – 2158.

[98] Hashin, Z., and Shtrikman, S., 1962. "A variational approach to the theory of the effective magnetic permeability of multiphase materials". *Journal of Applied Physics,* **33**, pp. 3125 – 3131.

[99] Shetty, D. K., Rosenfield, A. R., McGuire, P., Bansal, G. K., and Duckworth, W. H., 1980. "Biaxial flexure tests for ceramics". *American Ceramic Society Bulletin,* **59**(12), pp. 1193 – 1197.

[100] Ovri, J. E. O., 2000. "A parametric study of the biaxial strength test for brittle materials". *Materials Chemistry and Physics,* **66**(1), pp. 1 – 5.

[101] de With, G., and Wagemans, H. H. M., 1989. "Ball-on-ring test revisited". *Journal of the American Ceramic Society,* **72**(8), pp. 1538 – 1541.

[102] Ban, S., Hasegawa, J., and Anusavice, K. J., 1992. "Effect of loading conditions on bi-axial flexure strength of dental cements". *Dental Materials,* **8**(2), pp. 100–104.

[103] Borger, A., Supancic, P., and Danzer, R., 2002. "The ball on three balls test for strength testing of brittle discs: stress distribution in the disc". *Journal of the European Ceramic Society,* **22**(9-10), pp. 1425–1436.

[104] Powers, L. M., Salem, J. A., and Weaver, A. S., 2002. "Stresses in ceramic plates subjected to loading between concentric rings". No. 1409, pp. 30 – 45.

[105] ASTM, F394-78. "Standard Test Method for Biaxial Flexure Strength (Modulus of Rupture) of Ceramic Substrates". In *ASTM International.*

[106] ASTM, C1499-05. "Standard Test Method for Monotonic Equibiaxial Flexural Strength of Advanced Ceramics at Ambient Temperature". In *ASTM International*.

[107] Young, W. C., and Budynas, R. G., 2002. *Roark's formulas for stress and strain.* McGraw-Hill.

[108] Giovan, M. N., and Sines, G., 1981. "Strength of a ceramic at high temperatures under biaxial and uniaxial tension.". *Journal of the American Ceramic Society,* **64**(2), pp. 68 – 73.

[109] Chao, L.-Y., and Shetty, D. K., 1991. "Reliability analysis of structural ceramics subjected to biaxial flexure". *Journal of the American Ceramic Society,* **74**(2), pp. 333 – 344.

[110] Wereszczak, A. A., Swab, J. J., and Kraft, R. H., 2003. "Effects of Machining on the Uniaxial and Equibiaxial Flexure Strength of CAP3 AD-995 Al_2O_3". *ARL Technical Report*.

[111] Kao, R., Perrone, N., and Capps, W., 1971. "Large- deflection solution of the coaxial- ring- circular- glass- plate flexure problem". pp. 566 – 71.

[112] Salem, J. A., and Powers, L., 2003. "Guidelines for the testing of plates". Vol. 24, pp. 357 – 364.

[113] Schneider, T., Greil, P., and Schober, G., 1999. "Strength modeling of brittle materials with two- and three-dimensional pore structures". *Computational Materials Science,* **16**(1-4), pp. 98 – 103.

[114] Radovic, M., and Lara-Curzio, E., 2004. "Mechanical properties of tape cast nickel-based anode materials for solid oxide fuel cells before and after reduction in hydrogen". *Acta Materialia,* **52**(20), pp. 5747 – 5756.

[115] Atkinson, A., Bastid, P., and Liu, Q., 2007. "Mechanical properties of magnesia-spinel composites". *Journal of the American Ceramic Society,* **90**(8), pp. 2489 – 2496.

[116] Pabst, W., Gregorova, E., and Ticha, G., 2006. "Elasticity of porous ceramics - A critical study of modulus-porosity relations". *Journal of the European Ceramic Society,* **26**(7), pp. 1085 – 1097.

[117] Krohn, M. H., Hellmann, J. R., Shelleman, D. L., Green, D. J., Sakoske, G. E., and Salem, J. A., 2002. "Test methodology for strength testing of soda-lime-silica float glass before and after enameling". *Journal of Testing and Evaluation,* **30**(6), pp. 470–477.

[118] Hsueh, C. H., and Luttrell, C. R., 2007. "Recent advances in modeling stress distributions in multilayers subjected to biaxial flexure tests". *Composites Science and Technology,* **67**(2), pp. 278 – 285.

[119] Phillipps, A., Clegg, W., and Clyne, T., 1994. "Failure of layered ceramics in bending and tension". *Composites,* **25**(7), pp. 524 – 533.

[120] Powers, L. M., Salem, J. A., and Choi, S. R., 1993. "Failure prediction using the ring-on-ring test and the CARES/LIFE integrated design program". Vol. 55, pp. 55 – 63.

[121] Hulm, B. J., Parker, J. D., and Evans, W. J., 1998. "Biaxial strength of advanced materials". *Journal of Materials Science,* **33**(13), pp. 3255–3266.

[122] Borger, A., Supancic, P., and Danzer, R., 2004. "The ball on three balls test for strength testing of brittle discs: Part II: analysis of possible errors in the strength determination". *Journal of the European Ceramic Society,* **24**(10-11), pp. 2917–2928.

[123] Jones, R. H., Giancarli, L., Hasegawa, A., Katoh, Y., Kohyama, A., Riccardi, B., Snead, L. L., and Weber, W. J., 2002. "Promise and challenges of SiC_f/SiC composites for fusion energy applications". *Journal of Nuclear Materials,* **307**, pp. 1057–1072.

[124] Meyer, M. K., 2003. "Properties of (U, Pu)C and (U, Pu)N for use as gas-cooled fast reactor fuels". *ANL-West.*

[125] Rahman, A., Zunjarrao, S. C., and Singh, R. P., 2008. "Comparison of Bulk and Nanoscale Properties of Polymer Precursor Derived Silicon Carbide with Sintered Silicon Carbide". *Material Science & Technology 2008 Conference and Exhibition.*

[126] Liu, L., Li, X., Xing, X., Zhou, C., and Hu, H., 2008. "A modified polymethylsilane as the precursor for ceramic matrix composites". *Journal of Organometallic Chemistry,* **693**(6), pp. 917 – 922.

[127] Fang, Y., Huang, M., Yu, Z., Xia, H., Chen, L., Zhang, Y., and Zhang, L., 2008. "Synthesis, characterization, and pyrolytic conversion of a novel liquid polycarbosilane". *Journal of the American Ceramic Society,* **91**(10), pp. 3298 – 3302.

VITA

Abhishek K. Singh

Candidate for the Degree of

Doctor of Philosophy

Dissertation: Novel Fabrication of SiC based Ceramics For Nuclear Applications

Major Field: Mechanical Engineering

Biographical:

Personal Data: Born in Allahabad, UP, India on January 01, 1979.

Education:

Received the B.Tech. degree from Indian Institute of Technology, Kanpur, UP, India, 2001, in Mechanical Engineering
Received the M.S. degree from State University of New York, Stony Brook, NY, USA, 2006, in Mechanical Engineering
Completed the requirements for the degree of Doctor of Philosophy with a major in Mechanical Engineering from Oklahoma State University in January, 2009.

Experience:

Has over **7** years experience in *Fiber–Composites* and over **3** years in *Polymer* and *Ceramic Nano–Composites*. Invention disclosure for **2** patents are under process and has exertise in Solid Mechanics, Materials Science, and Experimental Mechanics.

Name: Abhishek K. Singh Date of Degree: May, 2009

Institution: Oklahoma State University Location: Stillwater, Oklahoma

Title of Study: Novel Fabrication of SiC based Ceramics For Nuclear Applications

Pages in Study: 102 Candidate for the Degree of Doctor of Philosophy

Major Field: Mechanical Engineering

Advances in nuclear reactor technology and the use of gas-cooled fast reactors require the development of new materials that can operate at the higher temperatures expected in these systems. These materials include refractory alloys based on Nb, Zr, Ta, Mo, W, and Re; ceramics and composites such as SiC–SiC$_f$; carbon–carbon composites; and advanced coatings. Besides the ability to handle higher expected temperatures, effective heat transfer between reactor components is necessary for improved efficiency. Improving thermal conductivity of the fuel can lower the center-line temperature and, thereby, enhance power production capabilities and reduce the risk of premature fuel pellet failure.

Crystalline silicon carbide has superior characteristics as a structural material from the viewpoint of its thermal and mechanical properties, thermal shock resistance, chemical stability, and low radioactivation. Therefore, there have been many efforts to develop SiC based composites in various forms for use in advanced energy systems. In recent years, with the development of high yield preceramic precursors, the polymer infiltration and pyrolysis (PIP) method has aroused interest for the fabrication of ceramic based materials, for various applications ranging from disc brakes to nuclear reactor fuels. The pyrolysis of preceramic polymers allow new types of ceramic materials to be processed at relatively low temperatures. The raw materials are element-organic polymers whose composition and architecture can be tailored and varied.

The primary focus of this study is to use a pyrolysis based process to fabricate a host of novel silicon carbide–metal carbide or oxide composites, and to synthesize new materials based on mixed-metal silicocarbides that cannot be processed using conventional techniques. Allylhydridopolycarbosilane (AHPCS), which is an organometal polymer, was used as the precursor for silicon carbide. Inert gas pyrolysis of AHPCS produces near-stoichiometric amorphous silicon carbide (a-SiC) at 900–1150 °C. Results indicated that this processing technique can be effectively used to fabricate various silicon carbide composites with UC or UO_2 as the nuclear component.

ADVISOR'S APPROVAL: _____